UNIVERSITÀ DI PARMA

UNIVERSITÀ DEGLI STUDI DI PARMA

DOTTORATO DI RICERCA IN

FISICA

CICLO XXXVII

Local-FCS: a platform for image correlation spectroscopy

Coordinatore:

Chiar.ma Prof.ssa Raffaella Burioni

Tutore:

Chiar.mo Prof. Paolo Bianchini

Chiar.mo Prof. Alberto Diaspro

Dottorando: Simone Civita

Anni Accademici 2020/2021 – 2023/2024

Contents

a Federica

alle persone che mi hanno nel cuore

a mia Zia Anna e a mia nonna Emma

1 Introduction

There are some too who ascribe this heavenly sphere and all the worlds to spontaneity. They say that the vortex arose spontaneously, i.e. the motion that separated and arranged in its present order all that exists. This statement might well cause surprise.

Aristotle, Physics II 350 B.C. [1]

Five century B.C. in Greece arose the concept of atoms.
Democritus affirmed that the soul was a fire consisting of innumerable particles, which he termed atoms, perpetually in motion due to incessant collisions [2]. This idea has crossed the centuries through a few fragments and subsequent reinterpretations. After Epicurus, Lucretius, in *De Rerum Natura,* illustrated the continuous motion of atoms, using the analogy of dust particles moving unpredictably within sunlit beams. These early insights laid the base for the atomistic theory of matter, suggesting that all substances are composed of tiny, indivisible particles in perpetual motion.

Approximately 2,500 years later, we refer to this phenomenon as Brownian motion, named after the Scottish botanist Robert Brown. In 1827, Brown observed and meticulously described the erratic movement of pollen grains from various plants suspended in aqueous solutions under a microscope. He noted that the particles exhibited a jittery and unpredictable motion, which could not be explained by external currents or vibrations. Brown's observations were pivotal because they provided empirical evidence of the kinetic activity at the microscopic scale, bridging a gap between macroscopic observations and molecular dynamics.

Today, we understand that this erratic movement is fundamental to the functioning of life itself. Molecular machines within cells exploit this energy at the nanoscale to perform all essential tasks required for cellular function. Processes such as enzyme catalysis, DNA replication, and protein synthesis rely on the random collisions and movements facilitated by thermal energy. The stochastic nature of Brownian motion enables molecules to explore their environment rapidly, increasing the likelihood of necessary interactions occurring within the crowded cellular environment. At this spatial dimension—on the order of nanometres—chemical, mechanical, and electrostatic energies become comparable to thermal energy (Figure 1). This convergence presents unique opportunities for complex physical objects and processes utilized by living organisms. At this scale, the interplay between chance and necessity

becomes a driving force for biological functions. Thermal fluctuations can induce conformational changes in macromolecules, trigger signalling pathways, and influence the rates of biochemical reactions, all of which are essential for maintaining life.

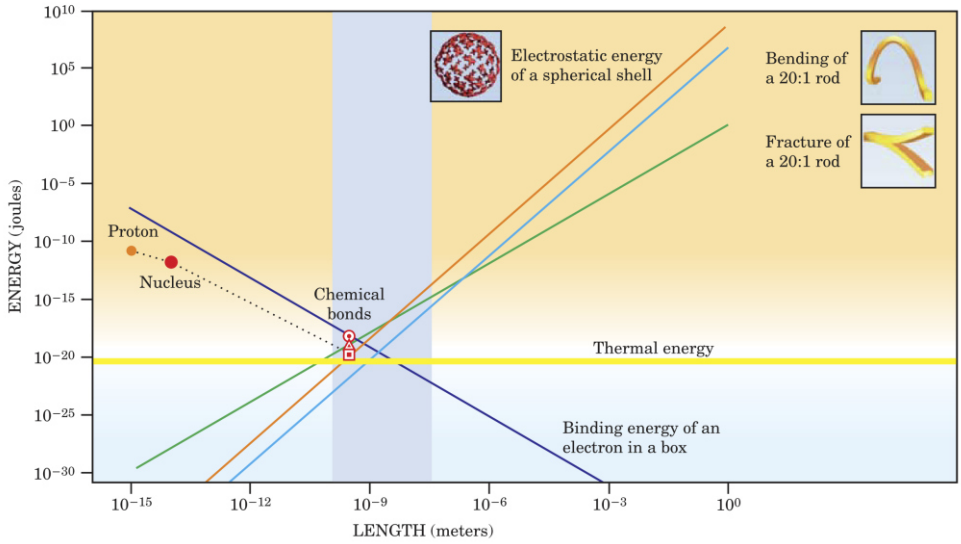

Figure 1 The convergence of different energy scales is depicted in this graph, illustrating how thermal, chemical, mechanical, and electrostatic energies associated with an object vary with its size. All these energy types converge as the object's size approaches the scale at which molecular machines operate (indicated by the shaded area). The thermal energy, represented by the horizontal line, remains constant regardless of size, corresponding to the thermal energy scale kT. The binding energy (in dark blue) is estimated by considering an electron confined in a box, with comparisons to measured binding energies for hydrogen bonds (square), phosphate groups in ATP (triangle), and covalent bonds (circle). Additionally, the graph shows characteristic energies for nuclear and subatomic particles. For bending energy (blue), an elastic rod with an aspect ratio of 20:1 bent into a semicircle was used. The fracture energy (green) was estimated by calculating the energy in the chemical bonds along the longitudinal cross-section of the rod. Lastly, a spherical protein's electrostatic energy (orange) was determined, assuming single-charged amino acids of specific sizes distributed on its surface. Reproduced from [3] with the permission of the American Institute of Physics.

In every living cell, millions of nanometric objects float, propelled by thermal agitation, and thus move via Brownian motion. These include proteins, nucleic acids, lipids, and various complexes critical for cellular operations. Some of these objects can become trapped in spatial regions due to interactions with cellular structures like the cytoskeleton or membrane compartments. Others are propelled by active transport mechanisms involving motor proteins such as kinesin, which move along microtubules, consuming chemical energy in the form of ATP.

Various sophisticated techniques have been developed to study these diffusive motions. Among them, Fluorescence Correlation Spectroscopy (FCS) is treated in detail in this thesis. FCS is a powerful tool that analyses fluctuations in fluorescence intensity within a tiny volume to extract information about the number and dynamics of fluorescent particles. It allows measuring diffusion coefficients, concentrations, and kinetic rates of molecular interactions in real time and with high sensitivity down to a single molecule regime.

In recent decades, technological advancements have enabled the probing of multiple positions (*quasi*) simultaneously, gaining the possibility to resolve diffusive heterogeneities within complex systems. Techniques such as spatially resolved FCS, fluorescence recovery after photobleaching (FRAP), and single-particle tracking (SPT) have expanded the ability to observe and quantify molecular movements with unprecedented precision. These methods recognize and measure that diffusion is not always uniform within cells. The environment of cells is highly heterogeneous due to obstacles, binding events, and active transport processes.

In this work, we will present the state of the art of FCS, particularly considering the image-resolved FCS (i.e. Image Correlation Spectroscopy, ICS, with some of its declinations). We will focus on the pros and cons of these methods to probe and quantify these diffusive heterogeneities. Then, we will introduce and propose a new concept called *local*-FCS that aims to increase the accuracy and precision of spatial-resolved FCS measurements. Coupling *local*-FCS to different imaging modalities, we aim to simplify the FCS analysis by spatially unmixing the system's complexity, reducing the possibility of artifacts and leading to a more straightforward interpretation of the autocorrelation functions. This approach will be illustrated and used in several biological contexts, clarifying fluorescent probes' diffusional behaviour.

1.1 The diffusion

The dynamics of diffusion and molecular transport processes are of significant importance in biology. In fact, in principle, we can associate each characteristic of a biomolecule's motion with a unique cellular function distinct from others. The diffusive modes of molecular motion at the intracellular level can be classified into two broad categories [4]:

1. **Brownian** diffusive motion, in which molecules or molecular complexes move purely due to thermal agitation, and diffusion is exclusively related to thermodynamic factors and the size of the molecules themselves.

2. **Anomalous** diffusive motions**:**

   - **Subdiffusive** or **confined** motion, in which the movement of molecules or molecular complexes is limited or confined by partially permeable or impassable barriers.

   - **Superdiffusive** motion, in which the movement of molecules or molecular complexes is "guided" in a non-stochastic manner by the action of other molecules, typically involves energy consumption.

In addition to these diffusion modes, it is also essential to consider the possibility of binding interactions between the molecule of interest and another molecule. Modelling these interactions is generally complex, but two relatively simple systems can be identified:

a. The binding interaction occurs with an association/dissociation time that is much faster than the diffusive motion.

b. The binding interaction occurs with an association/dissociation time that is much slower than the diffusive motion.

It is clear that case (a) leads to a "mediated" diffusion between different states (bound and unbound, in rapid equilibrium). On the other hand, case (b) results in two distinguishable types of dynamics: diffusion and binding. A particular instance of case (b) occurs when the formed complex is immobile, as it is part of an intracellular structure, such as a protein-DNA bond. In this case, (b) corresponds to a special instance of confined motion where the barrier to movement is also "absorbing".

In real scenarios, diffusion analysis is typically quite complex and closely tied to the specific process at play. However, it is possible to empirically describe confined and superdiffusive motions by using Brownian diffusion as a reference [5].

1.1.1 Brownian motion

In the late nineteenth century, Boltzmann introduced an atomistic perspective to the natural sciences, aiming to explain thermodynamic phenomena through the statistical behaviour of individual particles rather than continuous fields or concentrations. Despite facing substantial opposition and criticism from prominent colleagues, Boltzmann laid the foundation for what is now known as "statistical physics". His search for microscopic explanations of thermodynamic laws also stimulated interest in diffusion. In particular, there was interest in developing a theory that could explain the Brownian motion phenomenon: the erratic movement of pollen grains in water observed by Robert Brown in 1828 [6]. One of the most significant advancements came in 1905 when Einstein provided the first consistent microscopic interpretation of Fick's laws [7]. In his seminal paper, Einstein derived the diffusion constant from a molecular perspective, marking a major step forward in understanding diffusion at the microscopic scale. The key insight of Einstein's work was the observation that small particles when near thermodynamic equilibrium, undergo a movement due to the finite temperature of their surroundings.

According to Einstein's theory, the solution to the diffusion equation is a normalized Gaussian distribution, where the variance increases linearly over time and provides the mean squared displacement (MSD) $w^2(t)$:

$$w^2(t) = 2NDt \tag{1}$$

Where t is the elapsed time, N is the dimensionality of diffusion, D is the diffusion coefficient.

Einstein's formulation is based on three key assumptions: (i) particles move independently of each other, (ii) their displacements are statistically uncorrelated, and (iii) their random movements are caused by thermal collisions with water molecules, with no preferential direction, and the distributions of step lengths and waiting times have finite means and variances [8].

Later, Smoluchowski [9][10] associated Einstein's model with the theory of random walks [11]. This connection highlighted the equivalence between the diffusion of a group of particles and the random walk of a single particle, demonstrating that the process is ergodic. This propriety means that following the motion of a single particle over a long period provides the same information as monitoring an entire ensemble of particles.

In a real biological context, this ergodic theorem is only weakly satisfied. For this reason, other diffusional modalities have been introduced to describe what happens inside the cell [12].

1.1.2 Anomalous Diffusion

In cells, it could happen that a molecule that initially exhibited Brownian motion could become confined within a specific region or may bind to another molecule, following its movement, breaking the ergodic hypothesis. These different types of motion typically arise from interactions between the particle and its surrounding environment. Studying these motions can provide valuable insights into the properties of the environment, the kinetics of molecular binding interactions, the presence of structures that influence particle diffusion, or the role of molecular motors [13]. To interpret these various behaviours and extract information about the surrounding media, significant theoretical work has been dedicated to describing diffusion in complex systems [12]. To describe these anomalous diffusional modalities (sub or superdiffusive) that scale the mean square displacement (MSD) differently due to the heterogeneous environment, this generalization of eq. (1) has been proposed [13]:

$$w^2(t) = 2ND_\alpha t^\alpha \tag{2}$$

Where $\propto$ is the diffusional anomalous parameter, $\propto = 1$ for Brownian motion, $0 < \propto < 1$ if we have a subdiffusive motion, and $\propto > 1$ is superdiffusive. Of note, the parameter D_α where $\propto \neq 1$ loses the physical meaning of the diffusional coefficient and holds an empirical ratio between the spatial and temporal features of motion.

In general, anomalous diffusion arises when at least one of the assumptions of Einstein's theory is violated, leading to deviations from the central limit theorem. For instance, anomalous diffusion may be caused by broad distributions of jump times (the time that a molecule has to wait between steps) or lengths or by strong correlations in the diffusive motion (for example in a directional motion).

1.1.3 How to measure diffusion? SPT, FRAP and FCS

If we could track a single molecule in real-time - as it happens in a single particle tracking (SPT) experiment - we could plot the MSD versus time and determine the diffusion modality involved (Figure 2).

SPT has been used since 1987, when Brabander et al. demonstrated that 40nm gold nanoparticles could be visualized on the surface of living cells by optical microscopy [14].

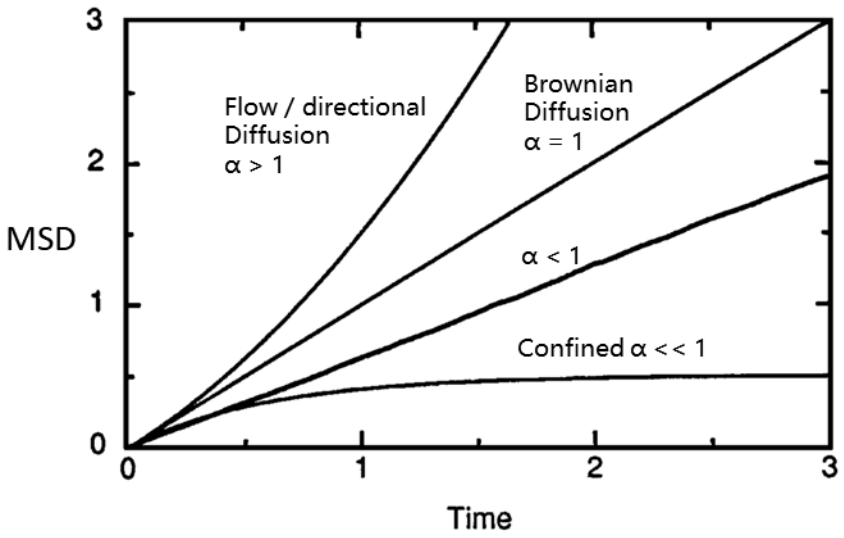

Figure 2 The mean-square displacement MSD as a function of time for different diffusional modalities. From the top: directional diffusion and/or flow $\propto > 1$, pure Brownian diffusion $\propto = 1$, diffusion in the presence of obstacles $\propto < 1$, and confined motion. Adapted from [15] with permission of Annual Review of Biomedical Engineering

Initially termed "*particle nanovid microscopy*," this technique relied on the use of colloidal gold particles attached to the biomolecule of interest. Ideally, each gold particle is conjugated with a single biomolecule. Due to their high Rayleigh scattering intensity, the spatial coordinates of the central positions of individual particles could be determined with nanometer precision through recordings taken at successive times using video-enhanced differential interference contrast (DIC) microscopy. This straightforward methodology allowed for the first-time tracking of kinesin-driven movements with nanometer-scale precision [16], thus paving the way for studying the tracking of individual molecules in the cell membrane.

The size of the scattering particle used for tracking imposes significant limitations on the biological processes that can be observed and may lead to substantial artefacts. Reducing the size of the particle is challenging because Rayleigh scattering decreases with the sixth power of the particle's diameter. Over the past 30 years, the ability to detect single fluorescent molecules at room temperature has opened the way to using single-particle tracking (SPT) via fluorescence. However, the duration of the trajectories and the precision of spatial positioning with fluorescent reporters are typically limited to only a few seconds and 20–50 nm respectively. In the last few years, the proposal of tracking fluorescent molecules with minimal photon fluxes (MINFLUX)

(Balzarotti, F., et al. 2017 [17] Eilers Y., et al. 2018 [18]) allowed tracking (in 3D) fluorescent molecules with few nanometer uncertainties with very few hundreds of photons.

One of the remaining drawbacks of this technique is the difficulty of preparing a living sample with a single molecule level expression in a single cell. This extremely low labelling density translates to a very long measurement (with respect to the typical movement of the cell) to achieve a good spatial statistic (Priest et al. 2019 [19]).

Prior to the development of techniques for single-particle tracking, other methods for studying dynamics had been proposed and successfully employed. Among these, fluorescence recovery after photobleaching (FRAP) made a significant contribution to cellular biology particularly thanks to its simplicity (Axelrod et al. 1976 [20]). This method involves inducing a significant localized change in fluorescence signal within the sample and evaluating the system's relaxation over time. More specifically, this technique leverages the photobleaching of the fluorescent marker, bound to the biomolecule of interest, by using an intense short and spatially localized excitation radiation. The subsequent fluorescence recovery in the photobleached region, driven by the molecular diffusion of non-bleached species, provides local dynamic information on molecular motion. The recovery is a clear, simple sign of the diffusion of the molecules. If the recovery is not complete, there is an immobile fraction of molecules. From the curve of the recovery, it is possible to extract the diffusional characteristics of the molecule [21]. This quantitative information requires complex mathematical models to interpret fluorescence recovery data and extract the molecular diffusion characteristics, resulting in one of the main limitations of this technique [22].

FRAP studies the system's relaxation back to a steady state (or equilibrium). The Fluctuation-Dissipation theorem (Kubo, R. 1966 [23]) assures that the information obtained via relaxation techniques can also be derived by observing the system's spontaneous fluctuations around its steady-state (or equilibrium) (Elson and W. W. Webb 1975 [24]).

The technique that analyses these spontaneous fluctuations around the steady state is known as Fluorescence Correlation Spectroscopy (FCS) and is the main topic of this thesis. This technique greatly benefits from the high sensitivity of fluorescence, which allows the detection of very small variations in the optical signal.

The key idea of this method for studying diffusion is to probe a volume and to record the fluctuation of temporal fluorescence intensity. If few molecules are

present in the volume, it is possible to recover the molecules' permanence time from the intensity temporal trace. This characteristic time is linked to the diffusion coefficient by the probing volume size. If the molecules in the solution are diluted, randomly dispersed, and do not interact between them, the number of molecules present in a volume follows the Poissonian distribution. Under this hypothesis, the concentration fluctuations δc become significant, relative to the mean $\langle c \rangle$, only if a few tens molecules are present in the volume.

$$\frac{\delta c}{\langle c \rangle} = \frac{1}{\sqrt{N}} \tag{3}$$

For systems with sub-micromolar biomolecular concentrations (typical of cellular environments), the use of a confocal microscope for its femtoliter confocal volume is a key point for obtaining sensitive FCS measurements. In a typical confocal system, with a confocal volume of 0.2 fl and a concentration of 100 nM, there are approximately 12 molecules in the volume, corresponding to a 30% fluctuation relative to the mean. Because of such a high sensitivity, it was one of the first single-molecule techniques proposed. Also, it explains why it is used for detecting very low fluorescent molecule concentrations.

Fluorescence correlation spectroscopy offers several advantages over single particle tracking and fluorescence recovery after photobleaching methods, especially in terms of ease of implementation, analysis versatility, and applicability to a wide range of sample densities [25]. A key benefit of FCS over SPT is that while SPT provides a highly accurate description of individual molecules' behaviour, it requires extremely low expression levels. Successful SPT tracking relies on having only a few emitting molecules within a small field of view (around 5x5 μm), resulting in long acquisition times to sample sufficient space, obtain a statistically significant number of traces, and generate reliable Mean Square Displacement (MSD) curves [26]. This requirement makes SPT more labour-intensive, although it offers the distinct advantage of detailed, molecule-specific dynamics, which are often more straightforward to interpret compared to the collective behaviour that FCS measures [15].

On the other hand, FRAP requires a significant external perturbation, using high-intensity laser radiation to bleach the fluorophores, which some studies suggest can potentially damage cells or induce artefacts like receptor cross-linking [27] (even if there is no strong consensus [28]). In contrast, FCS uses much lower laser power and studies systems at equilibrium, making it less invasive. While FRAP is valuable for large spatial scale dynamics [20], a classical FCS approach offers to probe a single small volume (with a typical size comparable with the optical resolution of the

microscope), becoming a sensitive method for studying fast dynamics and molecular interactions, with the added advantage of working in both equilibrium and steady-state conditions.

As reported in the next chapter, FCS was initially developed as a technique to monitor fluorescence fluctuations just in a single point of the sample. This approach focuses on studying fluorescence fluctuations in the time domain alone, using a specific descriptive function called the temporal autocorrelation function of the fluctuations $G(\tau)$. However, it soon became clear to explore also the opportunity given by probing the sample spatially $G(\rho)$ to obtain information about the concentration and the shape of the intensity distribution. In a few years, different methods have been proposed with the help of technological advancement. The possibility to collect, at high temporal resolution, fluctuations as images enable the study of the complete spatio-temporal autocorrelation function $G(\rho, \tau)$, where ρ represents the position vector in the Image Correlation Spectroscopy ICS.

2 Fluorescence Correlation Spectroscopy

In fact, many first elements of things, in many ways,
from infinite time until now, stimulated by collisions
and drawn by their own weight, are accustomed to move and wander
and to join together in every way and explore every possible interaction
by aggregating among themselves,
that it is no wonder if they also fell into such arrangements
and arrived at such movements as those
through which the sum of things, renewing itself, now is realized.

Lucretius - De Rerum Natura - V vv. 187-194[1]

In this chapter, we will discuss the state of the art of various techniques related to FCS. Specifically, we will focus on techniques that use image correlation spectroscopy to highlight their potential and limitations with the aim of proposing new methods that overcome such limitations (Chapter 3).

There have been several developments over the years that are relevant to the thesis's focus and have enabled unprecedented insights into biophysical diffusion processes.

The idea to extract diffusional information from the fluorescence fluctuation arose in the late sixties from Magde, Elson, Webb. In the first FCS paper, Magde et al., 1972 [29] highlighted the limitations of dynamic light scattering (DLS) [30] in resolving chemical kinetics. This is primarily because fluctuations in the dielectric constant, which DLS relies on, are often too small to detect accurately. DLS analyses changes in the refractive index caused by solute concentration fluctuations in a solution. However, beyond the challenge of resolving chemical kinetics, DLS has other significant limitations. It requires very low solute concentrations (in the micromolar range), its sensitivity is mainly influenced by the size and shape of the scatterer, it cannot distinguish between contributions from different biomolecules, and it lacks the ability to label specific proteins of interest. Magde, Elson, and Webb addressed these issues by extending DLS theory to fluorescence fluctuations, taking advantage

[1] *Translated by the author*
Namque ita multa modis multis primordia rerum | ex infinito iam tempore percita plagis |ponderibusque suis consuerunt concita ferri | omnimodisque coire atque omnia pertemptare, | quae cumque inter se possint congressa creare, | ut non sit mirum, si in talis disposituras | deciderunt quoque et in talis venere meatus, | qualibus haec rerum geritur nunc summa novando.

of the theoretically infinite contrast provided by fluorescence. This innovation allowed them to measure concentration fluctuations in a chemically reactive system at equilibrium, and in particular, they successfully measured the chemical rate constants of ethidium bromide's reversible binding to DNA and the diffusion coefficients of the Rhodamine 6G and EtBr.

A few years later, Ehrenberg & Rigler (1974) [31] developed the theory and built a setup capable of resolving the rotational Brownian motion by analyzing fluorescence intensity fluctuation after exciting the fluorophores with linearly polarized light. In the same year, Koppel [32] developed the first theoretical signal-to-noise derivation for the FCS autocorrelation function.

The first mix between spatial and temporal fluctuations measurement was performed by Weissman et al. (1976) [33], [34] to measure the molecular weight of DNA. In this work, the samples were rotated under an illumination beam. Analysing the autocorrelation, computed at a lag-time equal to the period of the rotation, they recovered the concentration of the DNA, uncoupling the other noise source.

In 1986, Petersen [35][34] suggested to scan over the sample rather than moving it. This adaptation of FCS for semi-static images (where diffusion or flow is slow compared to the scan time) involves measuring intensity fluctuations based on position instead of time, allowing the extraction of information about the number and size of aggregates. This method was first known as "scanning-FCS" since the spatial autocorrelation, from which the number and the size of the aggregations are recovered, is computed on a line obtained from a scanning microscope.

In 1993, Petersen [36] et al. generalized the spatial autocorrelation from 1D to image 2D images, calling it Image Correlation Spectroscopy (ICS). The article's last lines highlight the possibility of rapidly acquiring a sequence of images.

In 1994, Koppel [33] et al. generalized the concept of Weissman et al. (1976) by using a confocal line scan microscope to analyse the autocorrelation decay due to diffusion.

In 1995 Srivastava and Petersen [37] proposed using Temporal Image Correlation Spectroscopy (tICS) to recover the diffusion from the decay of the amplitude of the spatio-temporal correlation. Moreover, the same article introduces the use of 2-channel Image Cross-Correlation Spectroscopy.

In 1999, Brinkmeier et al. [38] proposed cross-correlation of fluctuation at different known positions to determine flow properties of velocity vectors in microstructured channels. This method is referred to as "2-beam cross-correlation".

In 2005, Hebert et al. [39] took advantage of analysing the full spatio-temporal autocorrelation functions in the so-called stICS analysis (spatio-temporal image correlation spectroscopy). With this approach, it became straightforward to map the velocity of the flow or the movement of proteins.

Kolin et al. (2006 [35]) presented the k-space analysis called kICS. Making the temporal autocorrelation in the Fourier space, instead of in the real space, it decouples the dynamics and the photophysical contribution to the autocorrelation decay. This is very effective for understanding if the measurement has binding kinetics.

Digman et al. in 2005 [40], [41] developed Raster Image Correlation Spectroscopy (RICS). This technique takes advantage of the *hidden* temporal information encoded in an image acquired with raster scanning. In a classical confocal microscope, the sample is probed at different points, collecting the intensity for a few ms. Such a time is called dwell time. When the microscope has ended to acquire a row of an image, typically, it moves back the mirror and starts to acquire the second row, and so on. Using the information of the dwell time and the line time, just performing a spatial autocorrelation, it is possible to recover a fast diffusion coefficient like free EGFP in the cytoplasm. An interesting development of this technique in 2018 by Scipioni et al. [42] has permitted the recovery of diffusional heterogeneities from a local evaluation of RICS (local-RICS).

In 2009, Digman and Gratton generalized the concept of 2-beam cross-correlation on a confocal microscope in the so-called Pair correlation [43]. This technique allows for detecting diffusion barriers and diffusion heterogeneity by observing a delay in the correlation maximum when barriers are present.

Di Rienzo et al., in 2013 developed another way of interpreting changes in the shape of the spatiotemporal autocorrelation in the image-derived mean squared displacement iMSD [4], [44], [45].

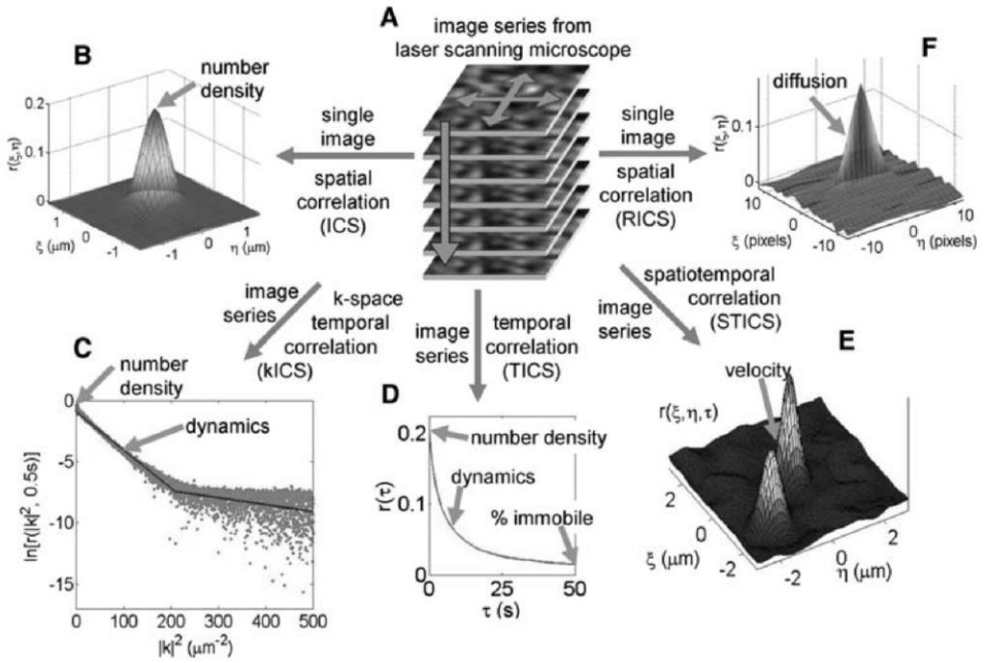

Figure 3 An overview of the image correlation techniques (ICS) developed. (A) All analyses are based on images or image series obtained using a confocal or two-photon laser scanning microscope or total internal reflection fluorescence (TIRF) microscopy. The typical sample is a cell membrane with a macromolecule of interest, selectively tagged with a fluorophore through antibody labelling or fluorescent protein transfection. (B) Image Correlation Spectroscopy (ICS) is performed on a static image to determine the number density and aggregation state of fluorescently labelled particles. (C) k-Space ICS (kICS) focuses on measuring particle dynamics, such as diffusion and flow, while being insensitive to fluorophore "blinking" and photobleaching. (D) Temporal ICS (tICS) examines an image series over time to extract information on dynamics, particle density, and the immobile fraction of fluorophores during the observation period. (E) Spatiotemporal ICS (stICS) combines spatial and temporal correlations from an image series to identify the flow direction and speed in the sample. (F) Raster ICS (RICS) applies spatial autocorrelation analysis to the rapid and slow components of a laser raster scan to study fast transport dynamics, such as cytosolic movement, using images acquired with a laser scanning microscope. Reprinted with permission from Springer Nature [46]. Copyright © 2007. Springer Nature Limited.

2.1 FCS Theory

The use of fluorescence intensity as a source of contrast in Fluorescence Correlation Spectroscopy (FCS) represents a significant improvement over Dynamic Light Scattering (DLS). Fluorescence provides a more versatile and sensitive approach, particularly for studying biological processes at the molecular level. In brief, some of the main advantages of fluorescence in FCS are:

1. Fluorescent probes can be used to label biomolecules. This approach is particularly advantageous in living systems, where fluorescent proteins can be genetically encoded, allowing real-time quantification of biomolecule's diffusions in their natural environment without disrupting biological processes.

2. Proportionality between fluorescence intensity and concentration. This linearity is crucial for all quantitative fluorescence methods and is verified for a typical biological system (where the absorbance is very low < 0.05).

3. Spectral separation of excitation and emission wavelengths: fluorescence, because of Stokes's shift, decouples excitation and emission wavelengths, ensuring that the emitted light can be detected without interference from the excitation source. This separation results in a theoretically infinite contrast, enhancing the sensitivity of measurements.

4. Time dependence of the fluorescence signal: The excited state of fluorescent molecules typically has an emission lifetime greater than 100 ps. This feature enables the fluorescence signal to be modulated based on environmental changes, such as pH or ion concentration variations, making it highly responsive to changes in the local chemical environment.

The fluorescence intensity collected during an experiment is also influenced by the optical and physical characteristics of the acquisition system. In the experiments described in this thesis, both confocal and wide-field microscopes were used. The wide field microscope is coupled with inclined illumination and Total Internal Reflection Fluorescence (TIRF) to increase the illumination sectioning.

The core of FCS analysis lies in fitting experimental correlation functions to theoretical models that describe the underlying diffusive processes being studied. These models account for several dynamics, such as diffusion in 2D and 3D, flow and active transport, multi-component systems, anomalous diffusion, and photo-physical phenomena. Theoretical autocorrelation functions (ACFs) for different diffusive systems will be derived in the next paragraph based on the experimental optical setup.

These correlation functions are further extended to spatial and spatiotemporal domains when using confocal scanning or camera-based optical schemes.

2.1.1 Fluorescence fluctuations in a diffusive system

To develop a mathematical formulation of FCS for diffusion, we begin by describing a fluorescent molecular species diffusing isotropically within a defined volume. Then, we will compute the correlation function under a general propagator function.

The concentration of the diffusive molecules $c(\boldsymbol{r}, t)$ in the defined volume will depend on space and time, denoted respectively by **r** and t. As highlighted before, FCS analyses the system at equilibrium. The concentration for each point in the space can be decomposed as a fluctuation around the temporal average.

$$\mathrm{c}(\mathbf{r}, \mathrm{t}) = \delta\mathrm{c}(\mathbf{r}, \mathrm{t}) + \langle \mathrm{c}(\mathbf{r}, \mathrm{t}) \rangle_{\mathrm{t}} \tag{4}$$

As a result of isotropic diffusion, the concentration fluctuations adhere to Fick's second law.

$$\frac{\partial}{\partial \mathrm{t}} \delta\mathrm{c}(\mathbf{r}, \mathrm{t}) = \mathrm{D}\nabla^2 \delta\mathrm{c}(\mathbf{r}, \mathrm{t}) \tag{5}$$

With the addition of a set of boundary conditions:

$$\Gamma_{\boldsymbol{r},t}(\delta c) = 0 \text{ for } \boldsymbol{r} \in S \tag{6}$$

Where S represents the geometric boundary of the system, and Γ is an operator that describes the boundary conditions (for instance, in the case of complete absorption at the boundary, the condition will be $c(\boldsymbol{r}, t)|_{\mathbf{r} \in \mathrm{S}} = 0$; in the case of reflection at the boundary, it can be imposed that the derivative with respect to the outward normal to the volume S is zero: that is, $\partial_N \, \delta c(\boldsymbol{r}, t)|_{\mathbf{r} \in \mathrm{S}} = 0$).

The solution to the Fick's diffusion equation can be expressed as [47]:

$$\delta\mathrm{c}(\mathbf{r}, \tau) = \int \delta\mathrm{c}(\mathbb{r}, 0)\, \mathcal{G}(\mathbf{r}, \tau | \mathbb{r}, 0) \mathrm{d}\mathbb{r} \tag{7}$$

Where $\mathcal{G}(\boldsymbol{r}, \tau|\mathbb{r}, 0)$ is Green's function of the diffusion equation, i.e., a solution to the partial differential equation that satisfies the initial condition

$$\mathcal{G} = \delta(\mathbf{r} - \mathbb{r}) \text{ for } \mathrm{t} = 0 \tag{8}$$

Due to the time invariance of Fick's equation, its solution can be written for any time interval as follows:

$$\delta c(\boldsymbol{r}, \tau) = \int \delta \mathrm{c}(\mathbb{r}, \mathrm{t})\, \mathcal{G}(\mathbf{r}, \mathrm{t} + \tau|\mathbb{r}, \mathrm{t}) \mathrm{d}\mathbb{r} \tag{9}$$

With

$$\mathcal{G}(\mathbf{r}, \mathrm{t} + \tau|\mathbb{r}, \mathrm{t}) = \mathcal{G}(\mathbf{r}, \tau|\mathbb{r}, 0) \tag{10}$$

Thus, Green's function for diffusion represents the probability density distribution of the concentration fluctuation displacement of the molecule from position $\mathbb{r}$ at time t=t to a position $\boldsymbol{r}'$ after t=t+τ time. τ it will be called *lag time*, and it is the actual temporal variable.

If we compute the autocorrelation of the concentration fluctuations, this could assume this formulation:

$$\begin{aligned} &\langle \delta \mathrm{c}(\mathbf{r}', \mathrm{t} + \tau) \delta \mathrm{c}(\mathbf{r}, \mathrm{t}) \rangle \\ &\qquad = \int \langle \delta \mathrm{c}(\mathbb{r}, \mathrm{t}) \delta \mathrm{c}(\mathbf{r}, \mathrm{t}) \rangle \mathcal{G}(\mathbf{r}', \mathrm{t} + \tau|\mathbb{r}, \mathrm{t}) \mathrm{d}\mathbb{r} \end{aligned} \tag{11}$$

Where averaging operation is considered with respect to time. Assuming the ergodic hypothesis, meaning:

$$\begin{aligned} &\langle \delta \mathrm{c}(\mathbf{r}', \mathrm{t} + \tau) \delta \mathrm{c}(\mathbf{r}, \mathrm{t}) \rangle \\ &\qquad = \lim_{\mathrm{T} \to \infty} \frac{1}{\mathrm{T}} \int_0^{\mathrm{T}} \delta \mathrm{c}(\mathbf{r}', \mathrm{t} + \tau) \delta \mathrm{c}(\mathbf{r}, \mathrm{t}) \mathrm{dt} \end{aligned} \tag{12}$$

At equilibrium, the fluctuations of the molecules are spatially uncorrelated due to the absence of flow processes. Therefore, we have:

$$\langle \delta c(\mathbb{r}, t)\delta c(\mathbf{r}, t)\rangle = \langle \delta c^2\rangle \delta(\mathbb{r} - \mathbf{r}) \tag{13}$$

As stated before, if the molecules do not interact between them, and the concentration is relatively low (hypothesis verified for mostly all intracellular biomolecules), their concentration follows Poisson statistics, and we have:

$$\langle \delta c^2\rangle = \langle c\rangle \tag{14}$$

where $\langle c\rangle$ represents the equilibrium concentration of the molecules, assumed to be uniform throughout the volume V considered, and obtained (through the ergodic theorem) as the limit of the time-averaged instantaneous concentration for infinite time.

Considering this, the equation for the correlation of concentration fluctuations can be rewritten as:

$$\begin{aligned} &\langle \delta c(\mathbf{r}', t+\tau)\delta c(\mathbf{r}, t)\rangle \\ &\qquad = \int \langle \delta c^2\rangle \delta(\mathbb{r} - \mathbf{r}) \mathcal{G}(\mathbf{r}', t+\tau|\mathbb{r}, t)\mathrm{d}\mathbb{r} \\ &\qquad = \int \langle c\rangle \delta(\mathbb{r} - \mathbf{r}) \mathcal{G}(\mathbf{r}', t+\tau|\mathbb{r}, t)\mathrm{d}\mathbb{r} \\ &\qquad = \langle c\rangle\, \mathcal{G}(\boldsymbol{r}', \tau|\boldsymbol{r}, 0) \end{aligned} \tag{15}$$

This function, derived in a general manner with respect to the form of Green's function, plays a key role in the theory behind fluorescence fluctuation experiments, as will be demonstrated in the following section.

One of Green's most useful analytical functions is related to the case of free diffusion. This, within an infinite volume of dimensionality k (k=1,2,3), could be written as:

$$\mathcal{G}(\mathbf{r}', \tau|\mathbf{r}, 0) = \frac{1}{(4\pi D\tau)^{k/2}} \exp\left(-\frac{(\mathbf{r}' - \mathbf{r})^2}{4D\tau}\right) \tag{16}$$

It is worth noting that, in this particular case, Green's function depends only on the difference between the spatial arguments, namely the mean squared displacement.

2.1.2 Single-point FCS

The simplest way to collect intensity fluctuations is to sample the fluorescent molecules that diffuse in a volume $V(\mathbf{r})$, in a fixed position.

The source of illumination excites only the molecules that reside in the illumination volume. $I_0(\mathbf{r})$ is the intensity distribution of the excitation light. The collected fluorescent signal will be proportional to the concentration of fluorescence molecules, to their molecular brightness b, to $I_0(\mathbf{r})$, and to the collection efficiency of the optical system $DET(\boldsymbol{r})$.

$$F(t) = \int I_0(\mathbf{r})DET(\mathbf{r})V(\mathbf{r})b\langle c(\mathbf{r},t\rangle \, d\mathbf{r} \tag{17}$$

In this definition of molecular brightness, b represents the probability of detecting a fluorescence photon emitted by a single molecule, combined with contributions from the excitation efficiency of the chromophore, the quantum yield of fluorescence, and the efficiency of the photon detection system.

At the equilibrium, the fluorescence signal can be expressed as an average value around a fluctuation:

$$F(t) = \delta F(t) + \langle F(t)\rangle \tag{18}$$

With $\langle \delta F(t)\rangle = 0$

It should be noted that, in this context, the averaging is purely temporal. The ergodic theorem ensures that, at equilibrium, the time-averaged signal from the observed region corresponds to the average fluorescence across all points in the sample.

The fluctuation density can be seen in relationship with the local concentration fluctuation

$$\delta c(\mathbf{r},t) = c(\mathbf{r},t) - \langle c(\mathbf{r},t)\rangle_t:$$

$$\delta F(t) = \int I_0(\mathbf{r}) DET(\mathbf{r}) V(\mathbf{r}) \delta(c(\mathbf{r}, t) b)\, d\mathbf{r} \tag{19}$$

Usually, the molecular brightness b is considered constant over time. This does not occur, for example, in the presence of *photobleaching*, which converts fluorophores into a non-fluorescent irreversible state. Assuming b remains constant, meaning there is no brightness reduction due to photobleaching or other phenomena, the equation simplifies to:

$$\delta F(t) = b \int I_0(\mathbf{r}) DET(\mathbf{r}) V(\mathbf{r}) \delta c(\mathbf{r}, t)\, d\mathbf{r} \tag{20}$$

We now define the normalized autocorrelation function.

$$G(\tau) = \frac{\langle F(t) F(t+\tau) \rangle}{\langle F(t) \rangle^2} - 1 \tag{21}$$

Using the eq. (18) it can be rewritten to

$$G(\tau) = \frac{\langle (\delta F(t) + \langle F(t) \rangle)(\delta F(t+\tau) + \langle F(t+\tau) \rangle) \rangle}{\langle F(t) \rangle^2} - 1 \tag{22}$$

$$= \frac{\langle \delta F(t) \delta F(t+\tau) + \delta F(t) \langle F(t+\tau) \rangle + \langle F(t) \rangle \delta F(t+\tau) + \langle F(t) \rangle \langle F(t+\tau) \rangle \rangle}{\langle F(t) \rangle^2} - 1$$

The temporal average over the fluctuation is 0, so all $\langle \delta F(t) \rangle = 0$. This signifies that, when performing the temporal average, the second and the third terms became 0:

$$\langle \delta F(t) \langle F(t+\tau) \rangle \rangle = \langle \delta F(t) \rangle \langle F(t+\tau) \rangle = 0 \tag{23}$$

$$\langle\langle \mathrm{F(t)}\rangle \delta \mathrm{F(t+\tau)}\rangle = \langle \mathrm{F(t)}\rangle\langle \delta \mathrm{F(t+\tau)}\rangle = 0 \tag{24}$$

Since it's a stationary process $\langle \mathrm{F(t+\tau)}\rangle = \langle \mathrm{F(t)}\rangle$:

$$\begin{aligned} G(\tau) &= \frac{\langle \delta \mathrm{F(t)}\delta \mathrm{F(t+\tau)} + \langle \mathrm{F(t)}\rangle^2\rangle}{\langle F(t)\rangle^2} - 1 \\ &= \frac{\langle \delta \mathrm{F(t)}\delta \mathrm{F(t+\tau)}\rangle + \langle \mathrm{F(t)}\rangle^2}{\langle F(t)\rangle^2} - 1 \\ &= \frac{\langle \delta \mathrm{F(t)}\delta \mathrm{F(t+\tau)}\rangle + \langle \mathrm{F(t)}\rangle^2}{\langle \mathrm{F(t)}\rangle^2} - 1 \\ &= \frac{\langle \delta F(t)\delta F(t+\tau)\rangle}{\langle F(t)\rangle^2} \end{aligned} \tag{25}$$

In this way we have demonstrated that

$$\mathrm{G(\tau)} = \frac{\langle \mathrm{F(t)F(t+\tau)}\rangle}{\langle \mathrm{F(t)}\rangle^{\,2}} - 1 = \frac{\langle \delta \mathrm{F(t)}\delta \mathrm{F(t+\tau)}\rangle}{\langle \mathrm{F(t)}\rangle^2} \tag{26}$$

The next step is to substitute F(t) with eq. (17).

$$\mathrm{G(\tau)} = \tag{27}$$

$$\frac{b^2 \int\int \mathrm{I_0(\mathbf{r})I_0(\mathbf{r}')\ DET(\mathbf{r})DET(\mathbf{r}')V(\mathbf{r})V(\mathbf{r}')\langle c(\mathbf{r},t)c(\mathbf{r}',t+\tau)\rangle\, d\mathbf{r}d\mathbf{r}'}}{b^2\langle \int \mathrm{I_0(\mathbf{r})\ DET(\mathbf{r})V(\mathbf{r})c(\mathbf{r},t)\, d\mathbf{r}}\rangle_{\mathrm{t}}^{\,2}} - 1$$

The only variable that has the temporal dimension at the denominator is the concentration. So it can be removed from the integral. Moreover, another very general simplification is when the sample occupies a volume V(**r**) larger than the observed volume. This results in considering V(r)=1 in the integral.

These considerations led the autocorrelation to be the simple as:

$$G(\tau) = \frac{\int\int I_0(\mathbf{r}) I_0(\mathbf{r}')\ DET(\mathbf{r}) DET(\mathbf{r}') \langle c(\mathbf{r},t) c(\mathbf{r}', t+\tau)\rangle\, d\mathbf{r} d\mathbf{r}'}{\langle c\rangle_t^{\,2} (\int I_0(\mathbf{r})\ DET(\mathbf{r}) d\mathbf{r})^{\mathbf{2}}} - 1 \qquad (28)$$

The product of $I_0(\mathbf{r})$ for $DET(\boldsymbol{r})$ is the well know Point Spread Function $\Omega(\boldsymbol{r})$, and it's convenient to use in the formula. Switching to the fluctuation, the eq. can be written as:

$$G(\tau) = \frac{\iint \Omega(\mathbf{r}') \langle \delta c(\mathbf{r},t) \delta c(\mathbf{r}', t+\tau)\rangle \Omega(\mathbf{r}) d\mathbf{r} d\mathbf{r}'}{\langle c(\mathbf{r},t)\rangle_t^{\,2} (\int \Omega(\mathbf{r})\, d\mathbf{r})^2} \qquad (29)$$

Moreover, thanks to the general demonstration obtained in the last paragraph in eq(15), we can use the propagator to simplify:

$$G(\tau) = \frac{\iint \Omega(\mathbf{r}') \mathcal{G}(\mathbf{r}', \tau | \mathbf{r}, 0) \Omega(\mathbf{r}) d\mathbf{r} d\mathbf{r}'}{\langle c\rangle (\int \Omega(\mathbf{r})\, d\mathbf{r})^2} \qquad (30)$$

This is a very general formulation of the temporal autocorrelation. Some properties of the correlation function can be analysed with complete generality without choosing the specific form of Green's function. For example, Eq. leads to the conclusion that:

$$G(0) \equiv \langle N\rangle^{-1} \qquad (31)$$

Where

$$\langle N\rangle = \langle c\rangle \frac{(\int \Omega(\mathbf{r})\, d\mathbf{r})^2}{\int \Omega^2(\mathbf{r}) d\mathbf{r}} \qquad (32)$$

Represents the effective average number of molecules simultaneously present in the observed volume.

This general formulation can be simplified for particular optical configurations like using a confocal or wide field TIRF microscope and imposing a propagator.

The Point Spread Function $\Omega(\boldsymbol{r})$ for a confocal microscope could be approximated with a 3D Gaussian.

$$\Omega(\mathrm{x},\mathrm{y},\mathrm{z}) = I\,\exp\left(-2\frac{\mathrm{x}^2+\mathrm{y}^2}{\omega_{\mathrm{xy}}^2}\right)\cdot\exp\left(-2\frac{\mathrm{z}^2}{\omega_{\mathrm{z}}^2}\right) \tag{33}$$

Where ω_{xy} and ω_z are commonly called waist and represent the $1/e^2$ radii of the 3D Gaussian observation volume for the radial and axial directions. I is a parameter that considers the power and a normalization factor.

Using the Brownian propagator in 3D (eq. (16))

$$\begin{aligned}\langle\delta c(r',t+\tau)\delta c(r,t)\rangle &= \langle c\rangle\,\frac{1}{(4\pi D\tau)^{3/2}}exp\left(-\frac{(r'-r)^2}{4D\tau}\right)\\ &= \langle c\rangle\,\frac{1}{8(\pi D\tau)^{3/2}}exp\left(-\frac{(x'-x)^2+(y'-y)^2+(\mathrm{z}'-z)^2}{4D\tau}\right)\end{aligned} \tag{34}$$

In the G(t):

$$G(\tau) = \tag{35}$$

$$\frac{\int\int\int\int\int\int e^{\frac{-2(x^2+x\prime^2)}{\omega_x^2}}e^{\frac{-2(y^2+y\prime^2)}{\omega_y^2}}e^{\frac{-2(z^2+z\prime^2)}{\omega_z^2}}\frac{e^{\left(-\frac{(x'-x)^2+(y'-y)^2+(z\prime-z)^2}{4D\tau}\right)}}{8(\pi D\tau)^{3/2}}dxdx'dydy'dzdz'}{\langle c\rangle\left(\int\int\int e^{-\frac{2x^2}{\omega_{\mathrm{x}}^2}}e^{-\frac{2y^2}{\omega_{\mathrm{y}}^2}}e^{-\frac{2z^2}{\omega_{\mathrm{z}}^2}}dx\;dy\,dz\right)^2}$$

The solution of the integral can be written as:

$$G(\tau) = \frac{1}{\langle c\rangle\pi^{3/2}\omega_x\omega_y\omega_z}\left(1+\frac{4D\tau}{\omega_x^2}\right)^{-1/2}\left(1+\frac{4D\tau}{\omega_y^2}\right)^{-1/2}\left(1+\frac{4D\tau}{\omega_z^2}\right)^{-1/2} \tag{36}$$

Since the PSF is symmetric in the xy plane $\omega_x = \omega_y = \omega_{xy}$, the equation can be written as:

$$G(\tau) = \frac{1}{\langle c \rangle \pi^{3/2} \omega_{xy}^2 \omega_z} \left(1 + \frac{4D\tau}{\omega_{xy}^2}\right)^{-1} \left(1 + \frac{4D\tau}{\omega_z^2}\right)^{-1/2} \tag{37}$$

Usually, this is expressed using the characteristic time $\tau_D = \omega_{xy}^2/4D$ that represents the transit time in the probed volume; and using the structure factor $\eta = \frac{\omega_z}{\omega_{xy}}$ that describe the ratio of the shape of the focal volume.

$$G(\tau) = \frac{1}{\langle c \rangle \pi^{3/2} \omega_{xy}^2 \omega_z} \left(1 + \frac{\tau}{\tau_D}\right)^{-1} \left(1 + \frac{\tau}{\eta^2 \tau_D}\right)^{-1/2} \tag{38}$$

The use of the τ_D is convenient because under these hypotheses (gaussian PSF and Brownian motion) is the time at which the ACF became halved. The factor η for a typical confocal setup is in the range of 3 to 8.

Of note, for $\tau = 0$ eq. (30) leads to a quantification of

$$V_{eff} = \frac{(\int \Omega(\boldsymbol{r})\, d\boldsymbol{r})^2}{\int \Omega^2(\mathbf{r}) d\boldsymbol{r}} = \pi^{3/2} \omega_{xy}^2 \omega_z \tag{39}$$

The final formulation for the temporal autocorrelation of fluorescence molecules that diffuse in a Brownian manner, measured using a confocal microscope and applied for curve fitting, became:

$$G(\tau) = \frac{1}{\langle N \rangle} \left(1 + \frac{\tau}{\tau_D}\right)^{-1} \left(1 + \frac{\tau}{\eta^2 \tau_D}\right)^{-1/2} + G_\infty \tag{40}$$

The use of a bias term of G_∞ are demonstrated theoretically recently by Kohler et al. 2023 [48]. If the measurement is infinitely long, the autocorrelation converges to 0 and the G_∞ became neglectable. Practically, the measurement is limited, and the estimation of the mean intensity could be corrupted by non-linear phenomena like photobleaching. The typical value of G_∞ is below 5% of the autocorrelation, but nevertheless, it is needed to fit the experimental points accurately. When the autocorrelation is computed in a very short time window (T<$10\tau_D$) they demonstrated that $G_\infty(\tau)$ become lag-time dependent, and proposed methods to fit the data that works for one diffusive population or multiple (in this last case, only if the brightness of each population is known).

Two properties of G(τ) are particularly relevant: 1) G(0)=1/N, meaning that the autocorrelation function at zero time decreases in amplitude as the number of diffusing molecules increases; 2) G(τ) decreases as τ increases, indicating that the correlation between fluorescence intensities measured at two different times tends to diminish as the time interval between those two points increases, due to the diffusive motion of the molecules as it traverses the confocal PSF.

The theoretical ACF corresponds to the expression for the mean squared displacement in three dimensions of a particle undergoing Brownian motion. For non-Brownian motion, the Green's function should be modified. In particular, since the propagator depends only on the difference in spatial coordinates, that is, on the mean squared displacement, we can use as mean squared displacement $w^2(t) = 2NDt^{\propto}$ as introduced before in the paragraph 1.1.2.

The autocorrelation then became:

$$\mathrm{G}(\tau) = \frac{1}{\langle \mathrm{N} \rangle} \cdot \left(1 + \left(\frac{\tau}{\tau_\mathrm{D}}\right)^{\alpha}\right)^{-1} \cdot \left(1 + \frac{\sigma_{xy}^2}{\sigma_z^2}\left(\frac{\tau}{\tau_\mathrm{D}}\right)^{\alpha}\right)^{-1/2} \tag{41}$$

where

$$\tau_\mathrm{D}{}^{\alpha} = \frac{\sigma_{xy}^2}{4\mathrm{D}} \tag{42}$$

If multiple diffusive populations are present, the computation of the ACF is direct for not interacting molecules. It will necessarily introduce two different concentrations of molecules, with 2 brightness *b*:

$$c_1(\boldsymbol{r}, t) = f c(\boldsymbol{r}, t);\ c_2(\boldsymbol{r}, t) = (1 - f) c(\boldsymbol{r}, t) \tag{43}$$

It can be demonstrated that the ACF became:

$$\begin{aligned} \mathrm{G}(\tau) = \frac{1}{\mathrm{N}\left(b_1 \mathrm{f} + b_2(1-\mathrm{f})\right)^2} \Bigg[& b_1^2 \mathrm{f} \left(1 + \frac{\tau}{\tau_{\mathrm{D}1}}\right)^{-1} \left(1 + \frac{\tau}{\eta\tau_{\mathrm{D}1}}\right)^{-1/2} \\ & + b_2^2 (1-\mathrm{f}) \left(1 + \frac{\tau}{\tau_{\mathrm{D}2}}\right)^{-1} \left(1 + \frac{\tau}{\eta\tau_{\mathrm{D}2}}\right)^{-1/2} \Bigg] + \mathrm{G}_\infty \end{aligned} \tag{44}$$

It is important to notice that the contribution to the amplitude of the ACF of the different populations is proportional to the square number of their brightness. This dependence is critical for a quantitative measurement of the fraction of the two populations:

$$G(0) = \frac{b_1^2 f + b_2^2 (1-f)}{N\left(b_1 f + b_2 (1-f)\right)^2} + G_\infty \tag{45}$$

If we have multiple N_c population, supposing we are interested only in the contribution of that component to the ACF α_i, eq. (44) can be written as:

$$G(\tau) = \frac{1}{N} \sum_{i=1}^{N_c} \alpha_i \left(1 + \frac{\tau}{\tau_{Di}}\right)^{-1} \left(1 + \frac{\tau}{\eta \tau_{Di}}\right)^{-1/2} \tag{46}$$

2.1.3 Spot variation FCS

Spot variation FCS [49] is a technique that allows the analysis of molecular diffusion by varying the size of the observation area (or "spot size"). By doing so, it is possible to infer how the diffusion properties of molecules change based on the spatial scale, providing information into the underlying mechanisms of molecular motion, such as free diffusion, hindered diffusion, or hopping between domains.

The core principle of spot variation FCS is that molecular dynamics can differ depending on the scale at which they are observed (Figure 4). The apparent diffusion coefficient remains constant across different spot sizes for free Brownian motion. However, for hindered or confined diffusion, the diffusion coefficient changes as the spot size decreases. For instance, if molecules are trapped in domains or transiently interact with structures like the cytoskeleton, the diffusion coefficient typically decreases as the observation spot becomes smaller. This variation in the diffusion coefficients with spot size can reveal different types of molecular interactions, such as trapping in domains, compartmentalization, or temporary binding events.

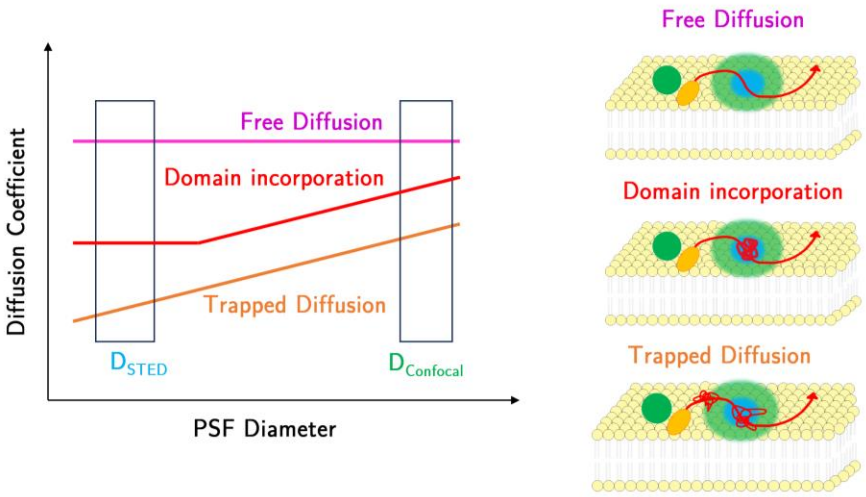

Figure 4 Spot variation FCS scheme. On the left side, if the diffusion is free, the diffusion coefficient computed is independent of the size of the PSF. If the diffusion is confined or trapped, the apparent diffusion coefficient decreases with the size of the PSF. If the diffusion is limited in a region, we have different modalities. If the size of the PSF is smaller than the size of the domain, we start to measure free diffusion. If the PSF is larger, we still find a trapped diffusion.

This technique could be implemented easily by changing the pinhole's size in the confocal microscope. Another way to change the volume size is by shrinking it using

a depletion beam, as is done in STimulated Emission Depletion (STED) [50], [51]. This super-resolution technique, depleting the fluorescence from the PFS's outer region, can reduce the focal volume to a few tens of nanometers. Using STED, if the time of arrival of photons is also collected, it could be possible to use the Separation of Photons by LIfetime Tuning (SPLIT) approach to obtain different temporal traces with different resolutions *a posteriori* [52]. Another way to change the spot volume is by using an Image Scanning Microscope (ISM) [53][54][55]. The spot variation could also be used with imFCS (next paragraph), merging the fluctuation that arises from near pixels [56], [57], [58].

2.1.4 Parallelization of FCS

Single-point FCS provides dynamic information about a single region in space, with dimensions equivalent to the PSF. The equilibrium assumption, along with the ergodic theorem, ensures that the observed dynamics represent a much larger region V, with $V \gg \Omega(\mathbf{r})$. However, this approach presents significant limitations when studying complex environments, such as subcellular regions, where the dynamics of a molecule may critically depend on its spatial location.

The technological advances, with the development of sensitive and fast detectors (like fast and sensitive cameras, resonant scanners, and sensitive single-photon detectors in a confocal microscope), enable probing a few μm^2 in less than 1ms, collecting the intensity in multiple points. With these sensitive and fast detectors, dynamics slower than 5-10 $\mu m^2/s$ can be easily detected, enabling probing multiple points and making multiplexing of FCS experiments possible. One of the first idealizations of computing $G(\tau)$ is from Petersen et al. in 1993 [36], but the first fast measurement using a 2x2 detector was by Blom and Rigler 2002 [59]. Ruan et al. in 2004 [60] proposed, with a confocal, to scan a single line multiple times as a particular image where performing temporal autocorrelation at a single pixel level. Sisan et al. 2006 used a spinning disk [61][62], Kannan et al. 2007 a camera TIRF[63], Wohland et al. 2010 [64] used a single plane illumination microscope. Usually, the analysis at the single pixel level of the ACFs is referred to as "image-FCS" (imFCS).

If a confocal is used to collect images (even when it is a line), the autocorrelation function computed for each pixel $G_{x,y}(\tau)$ has the same aspect as eq. (38). In this thesis, I will call "line-FCS" a repeated acquisition over a line and "circular-FCS" over an orbit.

The ACF functions will change when the microscope technique has a different PSF $\Omega\ r$. As an example, following the demonstration by Wohland et al. 2020

[52], the case of 2D diffusion with a square pixel camera detector is reported in Figure 5.

The detection function as a 2D Gaussian PSF integrated between the size of the pixel (a) has this aspect:

$$\mathrm{DET(x,y)} = \mathrm{DET(x)DET(y)} \tag{47}$$

$$\mathrm{DET(x)} = 1/a \int_0^a PSF(x - x_0)dx \tag{48}$$

Using a 2D Brownian propagator, a constant illumination I_0=1, the DET(x,y), the eq. (28) simplified to:

$$\mathrm{G_{x,y}(\tau)} = \frac{\iint_0^a \iint_0^a \iint_{-\infty}^{\infty} \iint_{-\infty}^{\infty} \mathrm{e}^{\frac{-2(x^2+x_0{}^2)}{\omega_{xy}^2}} \mathrm{e}^{\frac{-2(y^2+y_0{}^2)}{\omega_{xy}^2}} \mathrm{e}^{\frac{-2(x^2+x_0{}'^2)}{\omega_{xy}^2}} \mathrm{e}^{\frac{-2(y^2+y_0{}'^2)}{\omega_{xy}^2}} \frac{\mathrm{e}^{\left(-\frac{(x'-x)^2+(y'-y)^2}{4D\tau}\right)}}{4D\tau} \mathrm{dxdx'dydy'dx_0dx_0'dy_0dy_0'}}{\langle c\rangle \left(\iint_{-\infty}^{\infty} \mathrm{e}^{\frac{-2(x^2)}{\omega_{xy}^2}} \mathrm{e}^{\frac{-2(y^2)}{\omega_{xy}^2}} \mathrm{e}^{\frac{-2(x^2+x_0{}'^2)}{\omega_{xy}^2}} \mathrm{e}^{\frac{-2(y^2+y_0{}'^2)}{\omega_{xy}^2}} \frac{\mathrm{e}^{\left(-\frac{(x'-x)^2+(y'-y)^2}{4D\tau}\right)}}{4D\tau} \mathrm{dxdy} \right)^2}$$

Where the integrals are over the whole space from -inf to +inf to obtain the contribution of all fluorescent molecules excited. Then, we integrate over the pixel area (0 to a) to obtain the detected fluorescence.

Then, the autocorrelation can be solved to [58]

$$G_{x,y}(\tau) = \frac{1}{\langle c\rangle a^2} \left[\frac{\sqrt{4D\tau + \omega_{xy}^2}}{a\sqrt{\pi}} \left(\mathrm{e}^{-\frac{a^2}{4D\tau+\omega_{xy}^2}} - 1 \right) + \mathrm{erf}\left(\frac{a}{\sqrt{4D\tau + \omega_{xy}^2}} \right) \right]^2 \tag{49}$$

Ries J et al. 2008 [65] is a good reference for round pixels and more details.

I suggest simplifying this formulation by using an effective waist ($\omega_{xy\,eff}$) that takes into account the size of the pixel. Usually, the size of the pixel elements on the camera is fixed by the optical setup. The size of the PSF could be measured by analysing blinking objects (like DNA paint or specific dye or impurities in the glass). By this, it can be recovered the ω_{xy}. To fit the FCS curve it could be used eq. (49) or using a $\omega_{xy\,eff}$ with the classical eq. (40). The $\omega_{xy\,eff}$ could be extracted by a calibration with a note diffusion system (typically by using a membrane model). Another way to compute it is by simulations: a synthetic autocorrelation obtained with eq. (49) in the diffusional range expected could be fitted with the classical eq. (40). Imposing the same, simulated, diffusion coefficient the $\omega_{xy\,eff}$ could be computed (Figure 6).

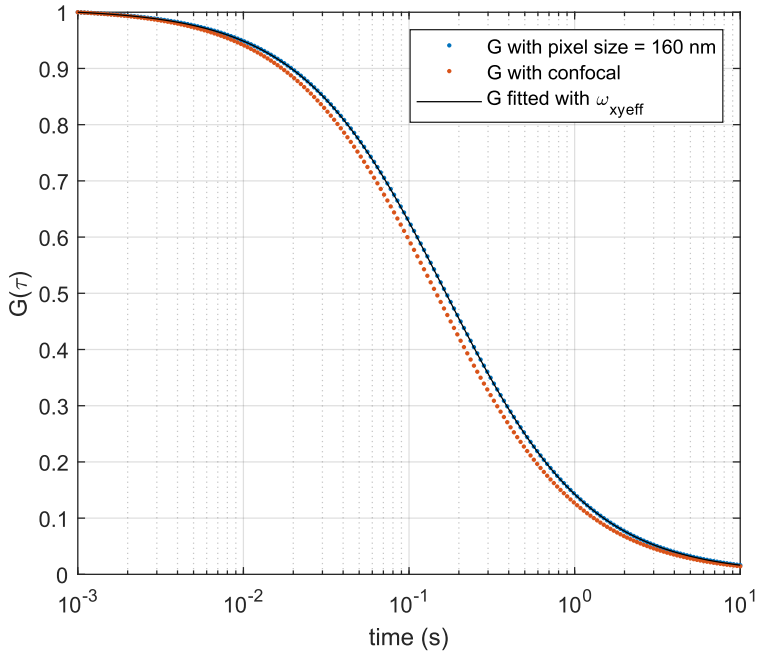

Figure 5 Normalized autocorrelation for D = 1 $\mu m^2/s$: in red the ACF obtained with a confocal with ω_{xy}=240 nm; in blue the ACF of the same identical particles obtained with a camera with a pixel size of a=160nm. As it appears clear, the latter curve is shifted to a longer lag time. The blue data points can be perfectly fit with eq. (40) using the effective waist $\omega_{xy\,eff}$ = 257 nm (black curve).

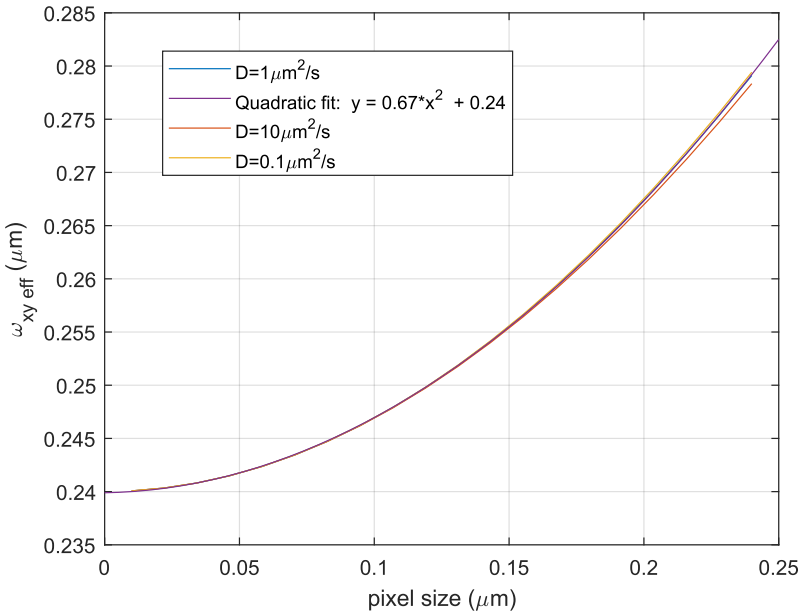

Figure 6 Calculation of the effective waist $\omega_{xy\,eff}$ vs the pixel size obtained for $\omega_{xy} = 0.24\,\mu m$. This data, fitted with a quadratic polynomial, is used to interpolate the $\omega_{xy\,eff}$ used to fit the data in Figure 5.

2.1.5 FCS segmentation

In live cells, the fluorescence intensity trace is often non-stationary due to cell movement or the internal dynamics of cellular components. To address this, the trace is typically segmented into shorter, quasi-stationary sections that are analysed individually [66]. This segmented approach not only helps maintain the stationarity condition required by FCS theory but also allows for the experimental determination of standard deviations in autocorrelation estimators and the calculation of goodness-of-fit statistics (Wohland et al. 2001) [67].

While segmenting the data can approximate stationarity, it comes at the cost of reducing the length of data available for calculating the autocorrelation function, which can introduce bias. It is known that correlation function estimators are biased when calculated from short data segments respecting the diffusion characteristic time (Ries and Schwille 2008) [65]. This bias impacts parameter estimation in FCS experiments, with the ACFs (segmented ACF) curve often shifting or changing shape if the data acquisition time is too short relative to the characteristic correlation time of the experiment. Kohler et al. 2022 [48] model this, proposing a formula for fitting the autocorrelation taken in a short intensity trace.

Following the paper, if T is the total acquisition time, the autocorrelation can be written as:

$$G_T(\tau;\, T) \;=\; G_{T=\infty}(\tau) \;+\; \Gamma_C(\tau;\, T) \;+\; \Gamma_S(\tau;\, T) \tag{50}$$

Where

$$\Gamma_S(\tau;T) = -\frac{T_S(T-2\tau)}{\langle \mathrm{F} \rangle (T-\tau)^2} H(T-2\tau) \tag{51}$$

Takes in account for the influence of shot noise, T_S is the sampling time, H(t) the Heaviside function, $\langle F \rangle$ the average fluorescence counts

$$\Gamma_C(\tau;T) = -G_0 \frac{B_2(T) + B_2(|T-2\tau|) - 2B_2(\tau)}{2(T-\tau)^2} \tag{52}$$

With B_2 represents a function called "second-order Binning function". In particular, if the diffusion is Brownian and the PSF is a 3D Gaussian, it is demonstrated that for one diffusive species, this function can be written as:

$$B_{2,2DG}(t;\tau_D) = 2\tau_D^2\left((1 + \mathrm{t}/\tau_\mathrm{d})\ln(1 + \mathrm{t}/\tau_\mathrm{d}) - \mathrm{t}/\tau_\mathrm{d}\right) \qquad (53)$$

This $\Gamma_C(\tau;T)$ describes the effect caused by correlations in the photon counts across the data segment. The contribution of these function is presented in Figure 7.

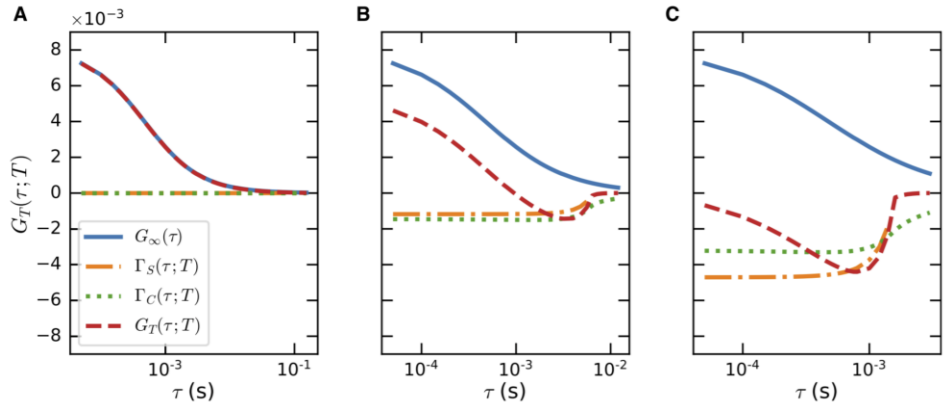

Figure 7 In red, the autocorrelation of a diffusional species with $\tau_D = 0.5$ ms with a total acquiring time of A) 6.6 s B) 13ms C) 3ms. In blue the ACF ground truth. In yellow $\Gamma_S(\tau;T)$ in green $\Gamma_C(\tau;T)$. Reprinted from Kohler et al. 2022 [48] Copyright 2022, with permission from Elsevier.

These formulae should be used to fit ACFs if the $T<50\tau_d$. For $T>50\tau_d$ a constant G_∞ (like what is proposed in eq. (40)) and a temporal threshold to the ACF ($\tau < \tau|\frac{\partial G}{\partial \tau} = 0$) can lead to good accuracy in the fitted parameters.

This can be shown by analysing the $\Gamma_s(\tau;T)$ and $\Gamma_C(\tau;T)$ as in Figure 7B: in this case $T=26\tau_d$. where the $\frac{\partial G_T}{\partial \tau} = 0$ for $\tau \sim 0.8$ms. Before this lag-time both Γ_s and Γ_C depend very weakly on τ and can be approximated as a constant G_∞. This became even more accurate when $T>50\tau_d$. This approximation to a constant is very convenient when there are presents multiple species; in this case $\Gamma_C(\tau;T)$ became very complex and, to be computed, it is needed a *priori* information about the brightness of each species.

To avoid these biases, as previous studies highlighted (an example in Figure 8), it is recommended to acquire data for a time long from 10^2 to 10^4 times the characteristic correlation time (Ries & Schwille 2008[65], Di Bona et al. 2019 [66], Wohland et al. 2020 [68]).

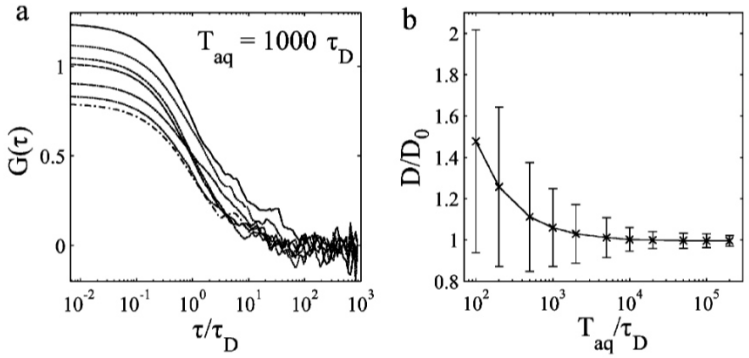

Figure 8 Statistical accuracy in dependence of the total acquisition time T_{aq}. A) simulated 2D ACF with $T_{aq} > 1000\ \tau_D$. Although the parameters are the same, the individual ACFs differ dramatically due to particle noise. B) Mean and standard deviation of the extracted diffusion coefficient from the fitted simulated ACF versus the acquisition time. Reprinted with permission from Ries and Schwille 2008 [65] Copyright 2008 Royal Society Of Chemistry.

2.1.6 Pair-correlation spectroscopy

The fluctuation measured in different pixels holds diffusional information. The first work is represented by two-beam cross-correlation (Brinkmeier et al. 1999 [69]) analysing the sample in r and r+ρ (Figure 9).

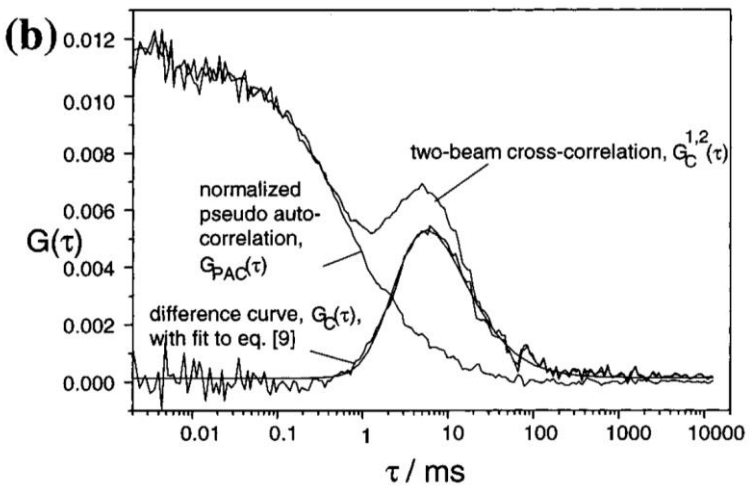

Figure 9 Two beam cross-correlation method. G_{PAC} is the autocorrelation of one beam measurement, $G^{1,2}{}_c$ is the cross-correlation between the two beams. Gc is the differential curve. Reprinted with permission from Brinkmeier et al. [38]. Copyright 1999 American Chemical Society.

A generalization easily implemented in any confocal system is the pair-correlation spectroscopy [43]. This involves an experiment in which a biological sample is repeatedly scanned over one dimension using a confocal microscope system, as in multiple point FCS (like in what we have called line-FCS and circular-FCS in 2.1.4). More specifically, the image consists of a line of N points, with the acquisition repeated a very high number of times (typically 100,000-200,000 for correctly sampling the diffusion). In this case, the collected fluorescence image can be described by a function F(p,n), where n represents the n-th acquired line and p represents the p-th pixel of the n-th line. If Δr and $\Delta\tau_l$ are the pixel's linear dimension and the time between two successive line acquisitions, respectively, p and n can be easily converted into a spatial variable and a temporal variable by $x=\Delta r \cdot p$ and $t=\Delta\tau_l \cdot n$ (an example of a *carpet* F(p,n) is represented by Figure 13). This setup will be used extensively in the thesis because it is relatively straightforward.

The pair correlation function (pCF) is then defined as:

$$\mathrm{pCF}(\delta p, \delta n) = \frac{\langle F(p,n)\, F(p+\delta p, n+\delta n)\rangle}{\langle F(p,n)\rangle \cdot \langle F(p+\delta p, n+\delta n)\rangle} - 1 \tag{54}$$

Where the averaging is applied over both the number of pixels and the number of lines (time). Essentially, pCF(δp,δn) measures the temporal correlation between the fluorescence measured in two pixels separated by a certain distance δp. Using $\tau = \Delta\tau_l n$

The autocorrelation could be fitted by [38] [70]:

$$G(x,\tau) = \frac{1}{\langle N\rangle} \cdot \left(1 + \frac{\tau}{\tau_D}\right)^{-1} \cdot \left(1 + \frac{\omega_{xy}^2}{\omega_z^2}\,\frac{\tau}{\tau_D}\right)^{-1/2} \exp\left(-\frac{(x)^2}{4D\tau + \omega_{xy}^2}\right) \tag{55}$$

An interesting propriety of this kind of curve is that for x> ω_{xy} the function is no longer a monotonic descendent curve but holds a maximum for $\tau = \tau_M$ where

$$2x^2\left(\omega_{xy}^2 + 4D\tau_M\right)^{-2} - 2\left(\omega_{xy}^2 + 4D\tau_M\right)^{-1} - \left(\frac{\omega_z^2}{\omega_{xy}^2} + 4D\tau_M\right)^{-1} = 0 \tag{56}$$

Eq. (56) can be further simplified if the diffusion is 2D or $\frac{\omega_z^2}{\omega_{xy}^2} > 5$ (like typically in a 2D STED microscope).

Under these hypotheses, we can write:

$$2x^2\left(\omega_{xy}^2 + 4D\tau_M\right)^{-2} - 2\left(\sigma_{xy}^2 + 4D\tau_M\right)^{-1} \simeq 0 \tag{57}$$

That leads to

$$D = \frac{x^2 - \omega_{xy}^2}{4\tau_M} \tag{58}$$

If x>3σ_{xy} the numerator could be approximated to

$$D \simeq \frac{x^2}{4\tau_M} \tag{59}$$

Committing an overestimation of D of around 10%

In recent years, pCF has been widely applied to the analysis of diffusion processes around physical barriers that separate intracellular regions [43] [71] [72].

Remarkably, if the system is spatially oversampled, this is one of the most effective and robust methods to compute the ω_{xy} of the system [43].

A special case and a very simple application of pCF, occurs when δp=0: in this case, pCF(0,δn) represents the average of N single-point FCS analyses, one for each pixel, under the assumption of chemical equilibrium.

Although the temporal resolution of pCF analysis is generally lower than that of a typical single-point FCS, as it is determined by the line scanning time Δt, pCF(0,δn) offers two main advantages: 1) easy implementation in a CSLM system (in many cases, it is possible to reach $\Delta\tau = 10 - 100$ μs, allowing measurement of D values in the range of 1-10 μm2/s); and 2) the ability to average single-point FCS information over a large number of pixels, thereby increasing the sensitivity for detecting dynamic processes.

This method will be used to show the characterization of liquid and order phase separation from the diffusional point of view in chapter 3.1.1.

This method could be used in coupling with STED depletion, as in Bianchini et al. [70]. This setup will be used in the study of PDL1 dynamics using a gated STED acquisition, as shown in Chapter 3.2.2.

Moreover the pCF(0,δn) is equivalent to $\langle pCF(\delta p, \delta n)\rangle_p$ plus an offset due to the immobile fraction (as it will be discussed more in detail in the tICS approach paragraph 2.1.10).

2.1.7 Image correlation spectroscopy

Image Correlation Spectroscopy (ICS) was developed as the imaging counterpart of FCS, where the autocorrelation is computed from the spatial fluorescence fluctuation (Petersen, 1993). The analysis of spatial fluctuations on one-dimensional images, such as line scans or orbital scans, also falls within this category (e.g., scanning FCS). ICS provides information on the density of clusters (Petersen, 1993) [36][73], their size, and the degree of aggregation (Wiseman, 1997) [74][75].

In ICS the autocorrelation function is just computed over the space, so for each image (with $\tau = 0$):

$$G(\boldsymbol{\rho}, \tau = 0) = \frac{\langle F(\mathbf{r}, t)F(\mathbf{r} + \boldsymbol{\rho}, t)\rangle}{\langle F(\mathbf{r}, t)\rangle\langle F(\mathbf{r} + \boldsymbol{\rho}, t)\rangle} - 1 \tag{60}$$

Where $\boldsymbol{\rho}$ is the radial spatial shift $\boldsymbol{\rho} = (\xi, \chi)$. F now no longer corresponds to the fluorescence intensity recorded at a single point, but rather to the spatial distribution of fluorescence over a much larger region. This is represented by a confocal image obtained by scanning the entire field of view of the sample.

The spatial autocorrelation could be fitted with a 2D Gaussian plus an offset if the image is obtained with a confocal microscope.

$$G(\xi, \chi) = \frac{1}{\langle N \rangle} \exp\left(-\frac{\xi^2 + \chi^2}{\omega_{xy}^2}\right) + G_\infty \tag{61}$$

As derived before in the general form (eq. (31)) the zero-lags amplitude of the G is proportional to the number of independent fluorescent particles per probing volume. G_∞ is the long-spatial lag offset used to account for the incomplete decay of the autocorrelation.

It is important to mention that the zero-lag space (as the zero lag-time in classical FCS) holds the noise contribution and must be discarded or interpolated from the nearest neighbours before performing the fit. [39] [25].

2.1.8 RICS

Raster Image Correlation Spectroscopy (RICS) [41] extends ICS by exploiting the inherent time structure of images recorded with a confocal microscope to extract dynamic system information. In confocal microscopy, a laser beam scans the sample in a raster way. If we want to acquire the intensity in a matrix of positions, the galvo-scanner starts to probe the first point. It excites and collects the photon in that position for a fixed time called *pixel dwell time* τ_p. After this time, it moves to the next point. This procedure is repeated till the last point in the first row. Then, the galvo scanner repositions the x axis to the starting point and moves the y axis to scan the second row. The time intercurred between the first points in the rows is called *repetition time* τ_l.

If we perform ICS autocorrelation on a sample in which the particles diffuse significantly on the time scale of image acquisition, the ICS autocorrelation will not be isotropic: the Gaussian shape will be stretched in the fast scan axis. We can recover the diffusional coefficients by analysing this shape.

The spatial autocorrelation will be the product of the correlating function of the diffusion $G_{diff}(\xi,\chi)$ and of scanner $S(\xi,\chi)$.

$$G_{RICS}(\tau) = G_{diff}(\xi,\chi)\, S(\xi,\chi) \; + G_{\infty} \tag{62}$$

$$G_{diff}(\xi,\chi) = \frac{1}{N}\left(1 + \frac{4D(\tau_p|\xi| + \tau_l|\chi|)}{w_{xy}^2}\right)^{-1}\left(1 + \frac{4D(\tau_p|\xi| + \tau_l|\chi|)}{w_z^2}\right)^{-1/2}$$

$$S(\xi,\chi) = \exp\left(-\frac{a^2(|\xi|^2 + |\chi|^2)}{4D(\tau_p|\xi| + \tau_l|\chi| + \omega_{xy}^2)}\right)$$

Where "a" is the distance between two probed point.

The times τ in $G_{RICS}(\tau)$ are determined by the recording time difference between two spatial points, expressed as the product of the spatial lags and the characteristic scanning times for both columns and rows, $\tau_p|\xi| + \tau_l|\chi|$. The exponential term represents the correlation of the PSF, which is broadened by diffusion and varies over time, depending on both τ_p and τ_l.

Taking advantage of this temporal information of the raster scans, RICS can explore very fast diffusion coefficients in a standard confocal system.

It is important to highlight that it is crucial, as a preprocess, to remove the slow or immobile population that can mask the correlation function.

2.1.9 Local-RICS

The standard RICS method provides only a single averaged diffusion coefficient for large regions, typically on the micron scale, but it lacks the spatial resolution necessary to capture the heterogeneity of diffusion within smaller cellular regions.

L-RICS, proposed by Scipioni et al. [42], overcomes this limitation by dividing the entire image into smaller sub-regions, or masks, of around 25 × 25 pixels (which corresponds to spatial resolutions in the range of 800 to 1000 nm). Such a subdivision allows for a localized calculation of the autocorrelation function (ACF) at each pixel, producing a more detailed map of molecular diffusion properties. The method also incorporates phasor analysis (Scipioni et al. [76]), a fit-free approach, to facilitate quick and efficient processing of the ACF data across all pixels.

The key benefit of this advanced approach over classical RICS is the possibility to resolve heterogeneities at micron scale: in the first paper, it has been used to map heterogeneous diffusion within the nucleus of live cells, highlighting differences between the nucleoplasm and nucleolus. Therefore, such an approach is particularly suited for understanding the complex, compartmentalized environments inside cells.

The major limitations rely on the autocorrelation curve's deformation when sampled over a small ROI (for a detailed description [77]), which limits this approach to near micrometre size. Another important point is that it simplifies the analysis by focusing on an apparent diffusion constant, potentially missing more complex diffusion phenomena like spatial confinement, binding reactions, or more than one diffusive component. This leads to potential biases, decreasing the accuracy of the measurement and the description of what happens at the single-pixel level.

2.1.10 tICS stICS & iMSD

The ability to capture images faster than ten times the characteristic diffusion times allows for the study of diffusion across larger biological regions. This results in an analysis that averages all diffusion occurring within the region of interest. Such averaging yields the highest signal-to-noise ratio in the autocorrelation curve when analysing intensity fluctuations.

The complete spatio-temporal autocorrelation, which holds the three spatial dimensions and the temporal one, can be written as [46]:

$$G(\boldsymbol{\rho},\tau) = \frac{\langle F(\mathbf{r},t)F(\mathbf{r}+\boldsymbol{\rho},t+\tau)\rangle}{\langle F(\mathbf{r},t)\rangle\langle F(\mathbf{r}+\boldsymbol{\rho},t+\tau)\rangle} - 1 \tag{63}$$

Where $\boldsymbol{\rho}$ is the radial spatial shift and τ the temporal *lag-time*. Like in ICS, F represents the images of fluorescence intensity. This formulation of the autocorrelation is at the basis of *Spatiotemporal Image Correlation Spectroscopy* (stICS). The average must be over the space and time.

Using the convolution $\otimes$ it can be demonstrated that the spatio-temporal autocorrelation can written as: [4]:

$$G(\boldsymbol{\rho},\tau) = \frac{1}{\langle N\rangle}\mathcal{G}(\mathbf{r}+\boldsymbol{\rho},\tau|\mathbf{r},0) \otimes [\Omega(\boldsymbol{\rho})] \otimes [\Omega(\boldsymbol{\rho})] \tag{64}$$

Where $\Omega(\boldsymbol{\rho})$ is, as eq. (33), the system's PSF. And $\mathcal{G}(\mathbf{r}+\boldsymbol{\rho},\tau|\mathbf{r},0)$ as in eq. (16) is the Brownian propagator.

Typically, the temporal acquisition is only in the 2D plane; for this reason, the radial shift becomes only on the 2D plane $\boldsymbol{\rho} = (\xi,\chi)$

Under the hypothesis of 3D Brownian motion and Gaussian PSF the autocorrelation can be written as:

$$G(\xi,\chi,\tau) = G(0,0,0) \cdot \left(1+\frac{\tau}{\tau_D}\right)^{-1} \cdot \left(1+\frac{\sigma_{xy}^2}{\sigma_z^2}\frac{\tau}{\tau_D}\right)^{-1/2} \cdot exp\left[\left(-\frac{\xi^2+\chi^2}{\sigma_{xy}^2}\right) \cdot \left(1+\frac{\tau}{\tau_D}\right)^{-1}\right] + G_\infty \quad (65)$$

Where $G(0,0,0)$ is the correlation at 0 time-lag with 0 spatial shift. τ_D is the characteristic diffusion time liked to the D with the already cited: $D = \sigma_{xy}^2/4\tau_D$.

The equation (65) can be rewritten in a simpler formula using the characteristic Gaussian shape following Di Rienzo et al. [4]

$$G_{3D}(\xi,\chi,\tau) = G_{3D}(0,0,\tau) \cdot exp\left[\left(-\frac{\xi^2+\chi^2}{\sigma_r^2(\tau)}\right)\right] + G_\infty \quad (66)$$

Where the amplitude of the autocorrelation is:

$$G_{3D}(0,0,\tau) = G(0,0,0) \cdot \left(1+\frac{\tau}{\tau_D}\right)^{-1} \cdot \left(1+\frac{\sigma_{xy}^2}{\sigma_z^2}\frac{\tau}{\tau_D}\right)^{-1/2} \quad (67)$$

And the variance of the Gaussian function is:

$$\sigma_r^2(\tau) = 4Dt + \sigma_0^2 \quad (68)$$

$G_{3D}(0,0,\tau)$ represents the value of the spatiotemporal autocorrelation calculated with zero spatial displacements, meaning it is independent of the spatial component. For this reason, $G_{3D}(\tau)$ is referred to as temporal Image Correlation Spectroscopy (tICS) and provides information analogous to single-point FCS, although it is averaged over the entire image.

$\sigma_r^2(\tau)$ is called *image-derived* MSD (iMSD) and represents the mean squared displacement in the lateral plane of the focal point (i.e., the confocal image plane). The correlation function is thus Gaussian, decreasing in amplitude and broadening over time, following the characteristics of the motion and the PSF.

σ_0^2 represents the variance of the correlation function at time zero, and it can be written as:

$$\sigma_0^2 = \sigma_p^2 + \sigma_{xy}^2 \tag{69}$$

where σ_p^2 is a characteristic parameter related to the size of the diffusive particle. For particles much smaller than the PSF $(\sigma_p \ll \sigma_{xy})$, as is the case with individual proteins, the variance of the correlation function corresponds exactly to the lateral dimension of the PSF.

G_∞ indicates the residual correlation at an infinite time. This parameter arises from the difference in normalization of $G(\boldsymbol{\rho}, \tau)$ compared to $G(\tau)$. A simple example can explain this effect. In an FCS experiment, if we consider a fixed molecule with constant emission, without photobleaching effects, localized in the observation volume, the intensity fluctuations $\delta F(t) = F(t) - \langle F(t) \rangle$ are purely caused by noise and are uncorrelated. Thus:

$$\langle \delta I(t) \delta I(t) \rangle = 0 \Rightarrow G(\tau) = 0 \tag{70}$$

This is not true for $G(\boldsymbol{\rho}, \tau)$: if there is an immobile molecule in the image, some pixels will always be brighter than others, and consequently, there will be a position with a temporally averaged intensity significantly higher than the spatial average of the image. Similarly, pixels further from the immobile molecule will have lower intensities. Therefore, the average fluctuations for these pixels are not zero, leading to a systematic deviation from zero:

$$\langle \delta I(\mathbf{r}, t) \delta I(\mathbf{r} + \boldsymbol{\rho}, t + \tau) \rangle_r > 0 \ \Rightarrow G(\boldsymbol{\rho}, \tau) > 0 \ \forall \ \tau \tag{71}$$

Due to this sensitivity of the autocorrelation function, $G(\boldsymbol{\rho}, \tau)$ will have an additive constant, usually referred to as G_∞, which indicates the residual correlation at infinite time.

For correcting this G_∞ it has been proposed different methods. The first holds in the moving median subtraction. The problem of this method, also when used as a detrend tool, is that the autocorrelation is forced to go at zero with the selection of the temporal window in which the average is computed. Hebert et al. [39] propose removing the DC component from the temporal trace for each pixel. This leads to an overcorrection of the G_∞ resulting in negative values for comparable $\rho \sim w_{xy}$.

A method that I proposed in my master's thesis relies on the subtraction from $G(\boldsymbol{\rho}, \tau)$ the $G_\infty \coloneqq \langle G(\boldsymbol{\rho}, \tau \gg \tau_D)\rangle_\tau$. This results in positive ACF, correcting for also fixed noise patterns that lead to a deformation in the correlation function.

As previously explained, in biological contexts, the assumption of isotropic Brownian diffusion is not always sufficient to model the studied phenomena, and it is convenient to generalize the motion by introducing the parameter α. In this case, the amplitude and variance of the autocorrelation function (eqs. (67)-(68)) take the following form:

$$G_{3D}(0,0,\tau) = G(0,0,0) \cdot \left(1 + \left[\frac{\tau}{\tau_D}\right]^\alpha\right)^{-1} \cdot \left(1 + \frac{\sigma_{xy}^2}{\sigma_z^2}\left[\frac{\tau}{\tau_D}\right]^\alpha\right)^{-1/2} \tag{72}$$

$$\sigma_r^2(\tau) = 4Dt^\alpha + \sigma_0^2 \tag{73}$$

Finally, an analytical form of $G(\boldsymbol{\rho}, \tau)$ does not exist for a heterogeneous context containing different diffusion regimes simultaneously, as found in living cells. An empirical approach consists of considering the total autocorrelation function as a "weighted" sum of individual autocorrelations [45]:

$$G_{tot}(\boldsymbol{\rho}, \tau) = \frac{1}{\langle N \rangle} \sum_i A_i \, G_i(\boldsymbol{\rho}, \tau) + \, G_\infty \tag{74}$$

with $\sum_i A_i = 1$

Here, N is the average number of particles present, A_i characterizes the fraction of molecules of the *i*-th species and $G_i(\boldsymbol{\rho}, \tau)$ represents the corresponding correlation function. This approach typically works for identifying well-distinguished diffusive regimes from a tICS perspective (e.g., dynamics with diffusion coefficients differing by at least 2x).

Identifying more than one component by stICS, especially by iMSD, is challenging and realistically impossible.

An useful approach for unmixing the dynamics in single components is the so-called "FRET filter," applicable when an interaction between one of the diffusing species and another molecule is known. Förster Resonance Energy Transfer is a technique based on the non-radiative energy transfer from an excited fluorophore

(called the donor) to a chromophore (the acceptor) via dipole-dipole interactions [78]. The efficiency of energy transfer depends inversely on the sixth power of the distance between the particles:

$$\mathrm{E_{FRET}} = \frac{R_0^6}{R_0^6 + r^6} \tag{75}$$

R_0 is called the Förster radius and represents the donor-acceptor distance at which the efficiency is E_{FRET}=0.5 considering all other physical parameters contributing to the energy transfer. For good D/A pairs, R_0 typically ranges from 3 to 7 nm; since energy transfer occurs on a nanosecond scale, FRET detects only molecules that form stable molecular complexes. For example, FRET has been used to visualize the complexation between proteins by labelling molecular partners with fluorophores capable of performing non-radiative energy transfer at a scale of less than 10 nm. The stICS-FRET approach relies on analysing fluorescence signal fluctuations resulting from the molecular complexation process, thus selectively identifying the diffusion dynamics of the complex "convoluted" with the dynamics of complexation when this latter causes a fluorescence signal fluctuation (flickering). More precisely:

$$\mathrm{G_{FRET}}(\boldsymbol{\rho}, \tau) = \mathrm{G_{3D}}(0,0,\tau)\, \exp\left[\left(-\frac{\xi^2 + \chi^2}{\sigma_r^2(\tau)}\right)\right] \mathrm{g_{\Phi}}(\tau) \tag{76}$$

where $g_{\Phi}(\tau) = \exp\left(-\frac{\tau}{\tau_{\Phi}}\right)$ is the flickering process function, and τ_{Φ} is the characteristic flickering time, i.e., the association/dissociation time of the complex. The diffusive part refers to the complex itself. It is important to note that flickering only affects the amplitude of the Gaussian distribution, i.e., the tICS, but not its variance, i.e., the iMSD. This decoupling allows for the "deconvolution" of the two processes (complexation and diffusion of the complex), representing one of the key advantages of the iMSD approach.

2.1.11 The effect of photobleaching and detrending

Each fluorophore, when excited, is subject to photochemical and photophysical processes that may lead to its deactivation, known as *photobleaching*. This effect increases with higher excitation light intensities, yet some fluorophores experience photobleaching even at relatively low intensities due to specific characteristics of their local environment (such as pH or oxygen concentration). In fluorescence correlation studies, it is crucial to implement a correction algorithm for photobleaching to prevent significant distortion in the results.

From a general perspective, photobleaching becomes a problem when it causes a substantial decrease in fluorescence over time. In such cases, measurements reflect an apparent loss in fluorophore concentration, which the autocorrelation function records as an additional dynamic process. This can lead to significant alterations in the correlation curve, giving misleading interpretations regarding the concentration and mobility of the fluorescent molecules. Therefore, it is necessary to apply corrections to ensure the accuracy of the analysis (Figure 10).

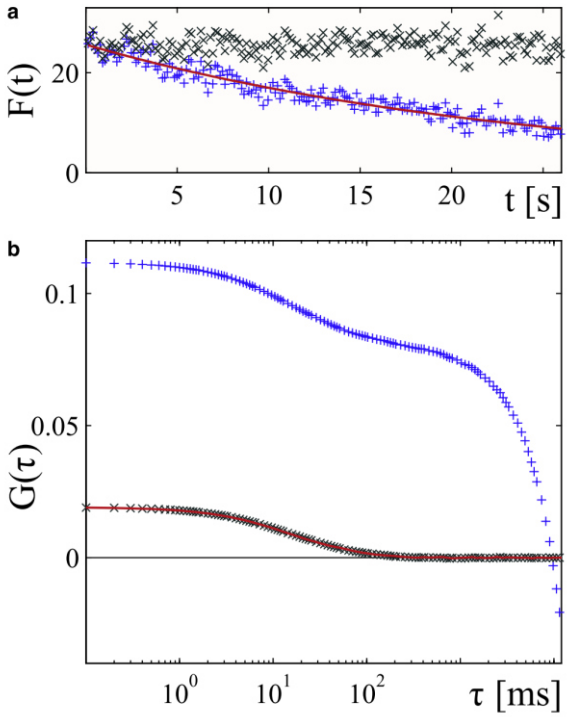

Figure 10 Intensity fluctuation with photo-bleaching (blue) and after the detrending (black) with the corresponding autocorrelation functions. Reproduced with permission from Ries et al. [79] Copyright 2007 Biophysical Journal

One of the most effective methods to correct photobleaching in the FCS context is the one proposed by Ries et al. [79]. This algorithm models the decay of the

global mean intensity trace $I(t_i) = \langle I(x, y, t_i) \rangle_{x,y}$ where the average is taken over the spatial coordinates x and y. For photobleaching effects causing less than a 50% decrease in initial counts, the decay is modelled using a single-exponential function of the form $f(t) = f_0 e^{-t/t_b}$. However, for more intense photobleaching, it is preferable to section the data stack into smaller segments for better handling.

The analytical photobleaching function is then applied to correct the temporal fluorescence trace on a pixel-by-pixel basis. In detail, this is done by imposing a constant average concentration for each pixel through a transformation, assuming that the particle distribution follows a Poisson distribution, meaning that the temporal variance is constant and equal to the mean:

$$I^c(x, y, t) = \frac{I(x, y, t_i)}{\sqrt{f(t_i)/f(0)}} + f(0)(1 - \sqrt{f(t_i)/f(0)}) \tag{77}$$

It is important to note that sectioning the stack before applying the photobleaching correction is often beneficial, allowing part of it to be excluded from analysis. This is particularly useful when there are pronounced discontinuities in the intensity trace or when applying the correction to the entire stack, which would either be ineffective or introduce artefacts into the data. By selecting only the portions of the stack that are more stable, the correction process becomes more robust, ensuring better accuracy in preserving the fluorescence signal dynamics.

Especially when dealing with CMOS camera-based measurement, it could be useful to fit each pixel independently instead of fitting the global spatial mean intensity because of different gain/offset for different pixels.

Another important consideration is to use a trimmed average, where the brightest and dimmest pixels are discarded, instead of relying on a simple average. This approach helps exclude outlier pixels, such as those that may correspond to bright vesicles or regions outside the cell.

Other methods based on moving temporal averages force the autocorrelation to zero for a time equal to the moving window. This could be useful, but if not done correctly, it could also lead to artefacts in the analysis. One particularly effective method is adding random numbers to the intensity trace that restores the constant value of the fluorescence [80].

We could also use a new method based on the Single Value Decomposition computation, which we have introduced in detrending Single Molecule Localization Microscopy dataset to estimate the trend [81].

2.1.12 Model Selection

When selecting the most appropriate model for fitting Fluorescence Correlation Spectroscopy (FCS) data, it is essential to balance simplicity and biological relevance. Even with perfect signal-to-noise ratios and ideal data, choosing the right model for diffusion can still be challenging due to the intrinsic complexity of cellular environments. Biological systems often exhibit phenomena like macromolecular crowding or sub-diffusion, which can deviate from idealized Brownian diffusion.

An important statistical tool to guide model selection is the F-test [68]. This test compares two competing models, assessing whether adding a new parameter is justified. In practical terms, the F-test compares the goodness-of-fit of two models by analysing their reduced chi-squared values (χ^2). If the F-statistic exceeds a critical value (which is based on the degrees of freedom and the desired confidence level), the more complex model is justified. For example, if Model 1 has fewer parameters but a higher χ^2 than Model 2, the F-test helps decide if the additional parameter(s) in Model 2 significantly improve the fit.

However, the F-test has limitations. It only allows pairwise comparisons and relies on assumptions about the normal distribution of errors, which are not always valid in FCS data. FCS measurements often produce autocorrelation functions with non-normally distributed data points.

In cases where multiple models need to be compared, Bayesian model selection can be more effective than the F-test, as it allows for a broader comparison across different models [82] [83].

In model selection, starting with simpler models and gradually increasing complexity is a good strategy, ensuring that the residuals and goodness-of-fit improve. For instance, in living cells, where crowding and subdiffusion are common, adding parameters to account for anomalous diffusion or confinement could yield a better fit.

Calibration measurements also play a significant role in model selection. Parameters such as the structure factor (ω_z/ω_{xy}) and confocal volume size, which are critical to FCS analysis, can be predetermined using standard dyes or ICS techniques. Fixing these parameters reduces uncertainty in fitting more complex biological systems. In cases where multiple diffusive pools are present (for instance, when both free diffusion and confined diffusion occur), calibration simplifies the fitting by eliminating potential sources of ambiguity.

SESAME Method

During my PhD, we developed an alternative model selection approach based on a Bayesian framework. We successfully applied such a method, named SESAME and originally developed by Sorrentino and Sommariva [84], to FCS [85].

The SESAME method (SEquential Semi-Analytic Monte Carlo Estimation) is a Bayesian framework that is able to address the limitations of classical fitting techniques in FCS. While traditional approaches, like least squares fitting, require the number of diffusing species to be predetermined, SESAME allows for simultaneous estimation of both the number of species (i) and their associated diffusion times (τ_{Di}) and the fraction (ρ_i). This flexibility is key to its advantage over methods relying on an F-test, which compares only two models at a time.

Another advantage of the SESAME approach is that it provides a full posterior distribution for all parameters. This allows, not only for a point estimate of the parameters but also for uncertainty quantification.

Moreover, contrary to fit based on the chi-square minimisation, this approach does not require a normal distribution of errors. This is very useful in FCS context in which the data are correlated in time.

By leveraging the full posterior distribution and prior information, SESAME can use the data more efficiently, potentially reducing the required acquisition time without sacrificing accuracy.

In future generalizations, we also want to extend the research space, including the anomalous diffusion. We would also like to improve the prior distribution of τ_{Di}, instead of a constant distribution, by taking advantage of other information, i.e. the cross-correlation introduced by Chapter 3.4.

2.1.13 MEM on Autocorrelation functions

Another method to extract diffusive characteristics from the autocorrelation curve is to apply the Maximum Entropy Method (MEM). This algorithm was developed firstly in the eighties by Skilling et al. [86] in astrophysics and then applied to analyse dynamics by Steinbach et al. [87][88].

Traditionally, the fits rely on models that assume few components (one or two), inferring the diffusion coefficient of each population. However, the problem can be reframed by setting a high fixed number of components (more than 100) each with a fixed diffusion coefficient, subsequently inferring each population's amount. In this way, among the possible distributions, we seek the one that *best* fits the data.

The autocorrelation function will be described as a sum of diffusive populations as eq. (46):

$$G(\tau) = \frac{1}{N}\sum_{i=1}^{N_c} \alpha_i \left(1 + \frac{\tau}{\tau_{\mathrm{Di}}}\right)^{-1} \left(1 + \frac{\tau}{\eta\tau_{\mathrm{Di}}}\right)^{-1/2} \tag{78}$$

Where we have N_c diffusive pool with a fixed characteristic time τ_{Di}. These diffusive populations have a logarithmically equidistributed τ_{Di} from a minimum (τ_{D1}) and maximum ($\tau_{\mathrm{DN_c}}$). The parameter to infer with this method is α_i.

The definition of *best* fit depends on prior information. Typically, if we were to minimize only the chi-squared (χ^2), multiple solutions, with this such high N_C, might exist. Therefore, the chi-squared will be weighted using the Maximum Entropy criterion: among all the distributions that minimize the chi-squared, we choose the one that maximizes entropy S defined as:

$$S = -\sum_i \alpha_i \ln(\alpha_i) \tag{79}$$

The entropy value of a distribution is inversely proportional to its degree of structure. A flat, uniform distribution has the highest entropy, while a distribution with many peaks has a lower entropy.

To achieve accurate fits, the relative weight of the entropy must be adjusted experimentally. This adjustment balances the influence of the entropy against the chi-squared minimization, preventing overfitting or underfitting of the data [89].

For a better understanding, a theoretical description of the algorithm will follow. For Bayes' theorem:

$$p(\Theta|y) \propto \pi(\Theta)p(y|\Theta) \tag{80}$$

Where $p(\Theta|y)$ is the posterior probability, representing the likelihood of having the collection Θ given the data y. In this specific context Θ refers to the collection of α_i; $\pi(\Theta)$ is the prior distribution of Θ; $p(y|\Theta)$ is the likelihood of obtaining the data y given the collection Θ.

If we have τ points and the ACF data y, which are affected by Gaussian noise with variance σ^2_{noise}

$$p(y|\Theta) \propto \prod_{\tau} \exp\left(-\frac{\left(\sum_i \alpha_i f_{\tau,i} - y_\tau\right)^2}{2\sigma^2_{\tau_{noise}}}\right) \tag{81}$$

where $f_{\tau,i} = \left(1 + \frac{\tau}{\tau_{Di}}\right)^{-1}\left(1 + \frac{\tau}{\eta\tau_{Di}}\right)^{-1/2}$

We can define different *a priori* functions. Maximum Entropy methods assume that the prior is:

$$\pi(\Theta) \propto \exp\big(S(\alpha_i)\big) \tag{82}$$

With S is the Entropy as defined by eq. (79)

Inferring is equivalent to maximizing the probability of having a collection of parameters given a set of data. In statistical terms, this involves determining the most likely set of parameters that could have generated the observed data. Eq. (80) could be maximized as:

$$\begin{aligned}\boldsymbol{max}(\mathrm{p}(\Theta|\mathrm{y})) \\ &= \boldsymbol{max}\left(\exp\left(S(\alpha_i)\right)\right. \\ &\left.\cdot \prod_{\tau} \exp\left(-\frac{\left(\sum_i \alpha_i f_{\tau,i} - \mathrm{y}_\tau\right)^2}{2\sigma_{\tau^2 noise}^2}\right)\right)\end{aligned} \tag{83}$$

Applying the natural logarithm, it translates in [86]:

$$\begin{aligned}\boldsymbol{max}(\ln(\mathrm{p}(\Theta|\mathrm{y}))) \\ &= \boldsymbol{max}\left(\left(S(\alpha_i)\right) - \sum_{\tau}\left(\frac{\left(\sum_i \alpha_i f_{\tau,i} - \mathrm{y}_\tau\right)^2}{2\sigma_{\tau^2 noise}^2}\right)\right)\end{aligned} \tag{84}$$

From this equation, it appears clear that to maximize the function it has to maximise the entropy and minimise the chi-squared $\sum_\tau\left(\frac{\left(\sum_i \alpha_i f_{\tau,i} - \mathrm{y}_\tau\right)^2}{2\sigma_{\tau^2 noise}^2}\right)$.

As anticipated before, to get better-fit convergence, it has been proposed to weight the entropy of a constant factor p [86]:

$$\boldsymbol{max}\left(p\, S(\alpha_i) - \sum_{\tau}\left(\frac{\left(\sum_i \alpha_i f_{\tau,i} - \mathrm{y}_\tau\right)^2}{2\sigma_{\tau^2 noise}^2}\right)\right) := \boldsymbol{max}\, Q \tag{85}$$

To search for the optimum, it can be used the iterative search for the gradient to maximize Q

$$\alpha_i(new) = \alpha_i(old) + step \cdot \alpha_i(old) \cdot \partial Q_i / \partial \alpha_i \tag{86}$$

Where

$$\partial Q_i / \partial \alpha_i = \left(p\frac{\partial S}{\partial \alpha_i} - \frac{\partial \chi^2}{\partial \alpha_i}\right) \tag{87}$$

$$\frac{\partial S}{\partial \alpha_i} = -1 - \ln(\alpha_i) \qquad \frac{\partial \chi^2}{\partial \alpha_i} = 2\frac{\sum_\tau[(\sum_i \alpha_i f_{\tau,i} - y_\tau)(f_{\tau,i})]}{\sigma^2_{noise}\tau} \tag{88}$$

After a sufficient number of iterations, that have to be selected according to the step size, from each ACF will be extracted a spectrum of diffusive populations that describe the curve. This approach will be used for the first time, coupled with imFCS, in the next chapter.

3 Local-FCS

Both the microscopic and macroscopic viscosity of the protoplasm are of importance; the first in relation to diffusion processes and the second in relation to the organization of the cells.
Gregorio Weber, PhD Thesis

The cellular world, with its spatial organization and dynamic interactions, is an extremely complex system. The physical approach aims to simplify the problem by focusing on a few measurable observables through experiments on living cells. From this perspective, studying dynamics on a global scale using image-based methods (such as Image Correlation Spectroscopy) offers a significant advantage: for a given area, one or two diffusion coefficients can be assigned to populations of fluorescent molecules. Knowing the molecular brightness allows us to determine the stoichiometric ratios of different populations. The signal-to-noise ratio is typically good, making the analysis relatively straightforward analysis.

As discussed in the theoretical chapter, the analysis is based on the assumption that the system is ergodic and spatially invariant. This leads to the selection of a region where a coherent biological function is present, such as the cellular or nuclear membrane. In a first approximation, this could also extend to the nucleus or cytoplasm. Within an entire area (typically a few square microns), a target biomolecule has a limited number of functions. The analysis will detect at least a *free* diffusion component and other diffusive features related to specific biological functions of this biomolecule within the spatial context. Each biological function can be associated with a subpopulation of the labelled biomolecule, characterized by its diffusion coefficient, as outlined in the first chapter.

Verifying the assumptions of ergodicity and spatial invariance is notably challenging. While some techniques and applications, such as studying cellular movements with spatiotemporal image correlation spectroscopy (stICS) [90][91], do not strictly depend on these criteria, they remain essential in most other contexts, particularly when analysing autocorrelation functions. If these conditions are not met, artefacts may arise, which are not always apparent through visual inspection of the autocorrelation curve alone. This interpretative challenge is one of the main limitations of applying FCS techniques, particularly in living cells, where these assumptions are only weakly verified.

As discussed earlier, the main causes for the failure of these assumptions include photobleaching, insufficient temporal sampling, cellular movement (even local), spatial heterogeneity (e.g., the presence of regions where different processes occur,

such as inside and outside an organelle), nonspecific signal, and the presence of aggregates/vesicles. Some of these issues can be mitigated by reducing the area of investigation: for instance, if a bright vesicle passes through a region or the cell moves at a certain point in the recording, the stack can be cropped in both time and space to minimize artefacts. How can we ensure that no other artefacts are yet present? It may happen that some spatiotemporal regions are "invisible" in terms of contrast when only studying the mean intensity. In this work, various methodologies will be proposed to identify potential artefacts and, ideally, isolate them from the analysis. The simplest solution is to reduce the area over which the assumption must be satisfied.

Another challenge with these ICS techniques when transitioning from in vitro to living cells is the oversimplification required to describe what happens in a given region within a complex biological context. From a biological perspective, how many functions does the biomolecule perform in this region? Mathematically, this question translates into selecting a model to fit an autocorrelation curve. As presented in 2.1.12, there are techniques, such as Bayesian algorithms, which aim to select the best model (but only after an a priori definition). Unfortunately, stICS iMSD RICS fails to describe more than one diffusive component.

We can confidently state that fewer events occur in smaller spaces. Therefore, reducing spatial dimensions may simplify the model selection problem by minimizing biological complexity.

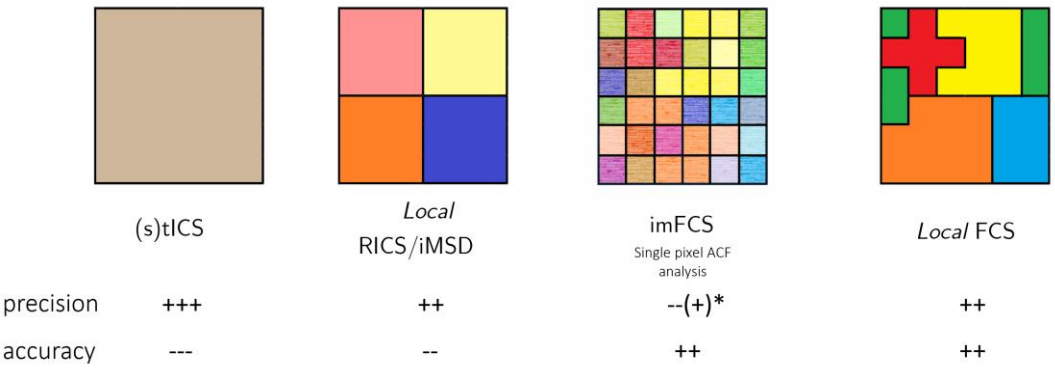

Figure 11: Scheme of *local* techniques. The heterogeneities could lead to a bias in the extracted parameters in ICS techniques (tICS stICS iMSD RICS). Some of the Local-ICS techniques suffer from oversimplified models (especially RICS and iMSD); the precision depends on how many pixels are used to compute the correlation functions. imFCS has a low precision in the fitted parameters caused by the low S/N ACFs (*improved by PCA filter in chapter 3.5). This single-pixel analysis has higher accuracy since it analyses the minimum complexity / smallest region accessible. Local-FCS exchange some spatial description ability for higher precision.

Naturally, as the area used for ICS analysis is reduced to the single-point level (imFCS), the signal-to-noise ratio (S/N) becomes critical [92]. We move from a curve with an excellent S/N—though it mixes multiple biological functions and artefacts due to the challenge of satisfying assumptions over larger areas—to curves with a lower S/N, where fewer biological functions (and thus fewer artefacts) are expected to coexist. According to Koppel's (1974) [32] theory of FCS noise, the S/N is inversely proportional to the acquisition time fixed by the sample movement in both approaches. Furthermore, in ICS, this ratio is divided by the squared number of pixels used for analysis, which increases the precision of the inferred diffusional parameters. For these reasons, using an ICS approach on small images seems to be a good compromise between precision and accuracy. But how much can the area for stICS or l-RICS be reduced? Malacrida et al. (2018) [93] claim that it is possible to recover a single diffusion coefficient (with a CCD camera) in the range of 400 $\mu m^2/s$ to 3×10^{-4} $\mu m^2/s$ for regions of interest (from 64 to 8 pixels – 6.4 µm to 1 µm) used in the iMSD analysis.

Scipioni et al. (2018) [42] noted that the size of the regions analysed must not be too small, as the ACF would deviate from its theoretical shape, leading to inaccurate fitting results for regions of interest smaller than 128×128 pixels. With typical pixel sizes used for RICS (30–50 nm), this corresponds to a spatial resolution of approximately 5 µm.

Longfils et al. (2019) [77] recently proposed a modified function for fitting the RICS autocorrelation when evaluated in regions of interest smaller than 50 × 50 pixels, accounting for the bias caused by insufficient spatial sampling. They demonstrated that this method works for areas as small as 6 × 6 pixels (1 × 1 μm). Compared to classical single-point FCS, Local iMSD and Local RICS methods offer the advantage of generating diffusion maps across large areas. Additionally, unlike approaches that only analyse the temporal autocorrelation decay of each pixel (such as imFCS), these methods can resolve faster diffusion coefficients using a standard confocal microscope. However, the limitation of these local ICS techniques is the oversimplified analysis. In detail, iMSD extracts only a few diffusion parameters [93] and after various attempts during this thesis, it is impossible to discern more than one diffusive pool. (Local-)RICS provides only a single diffusion coefficient for each ROI and cannot distinguish between different diffusion modalities. This oversimplification makes it difficult to quantitatively analyse and describe the complex diffusion network inside a living cell.

A bridge from the "*little* image" approach and a single point FCS is represented by the work of Scipioni et al. 2018 [53]. In this work, the authors develop a method to take advantage of image scanning microscopy (ISM) to recover the modality of diffusion in a single spot of FCS data using a spot variation approach. Additionally, they used the concept of pair correlations to analyse the diffusion modalities. Slenders et al. [54] extended the concept for a square detector 5x5. Currently, these micro-images are not collected at multiple points over an area but just in a single spot. Using a posteriori filtering with the collected micro-images over the scans would surely lead to extracting the diffusion modality with l-RICS (one of our future projects). Another way to do it is with a SPLIT-STED approach followed by spot variation analysis (Lanzanò et al. 2017 [52][94]).

In this work, we present a different strategy to overcome some of the ICS and single-pixel level problems:

The key idea of this work is to merge the autocorrelation data from regions where *similar* biological events occur.

In this way, we reduce the area in which the ACF is computed to the smallest possible unit (a single point/pixel) minimising the underlying biological complexity and simplifying the model selection. Moreover, this approach reduces the probability of including artefacts, as exposed above, ensuring the typical high accuracy of the single-pixel approach. To resolve the problem of the fitted parameters' precision, we merge (by simply averaging) the ACF that arise from *similar* points.

ICS methods rely on a "squared" *proximity* concept to define *similarity*. These approaches group pixels by a fixed ROI size in which the global ICS correlation functions are computed. By contrast, single-pixel analysis enables the exploration of a wider range of *similarity* criteria.

The linearity given by fluorescence between collected photons and concentration is one of the easiest sources of contrast in microscopy: it is possible to separate regions by sorting the intensity. Using this *similarity* definition, Chapter 3.1.1 will show measurements on lipid bilayers, and using this method, we can recover slightly diffusional features in multiple phases. The fluorescence probe has a higher affinity to one phase, resulting in a clear identification just by looking at the intensity.
Different biophysical aspects, such as fluorescence lifetime, could provide contrast and other *similarity* definitions.
An example of defining *similarity* could be comparing the shape of the autocorrelation in different positions. As shown in the previous chapter, the ACF contains a diffusion fingerprint. The evaluation of the shape could be addressed in several ways.
The simplest way consists of just fitting the ACFs with a theoretical model and merging the ACFs that share some parameters. This has been successfully used by analysing the dynamics of different proteins linked to EGFP, segregating the pixel where slow vesicles pass through the focal volume of excitations or related to clusters that move along with the cell membrane (chapter 3.3.4).

Another way of fitting explored in this work is the Maximum Entropy Method (MEM) [86][89][88]. For each spatial point, this method computes a spectrum of Brownian diffusion coefficients as the description of the autocorrelation curve. MEM is advantageous because it does not require a priori information. These spectra represent quantitative diffusional information that could be used to aggregate pixels that share a *similar* diffusional spectrum. In the chapter 3.3.2, MEM will be described in detail.

Clearly, it is possible to combine different techniques to increase the level of information in the concept of similarity. In this work, I explored a new, fast way of computing the radial pair correlation. This pair correlation could be fitted with a classical fit, or by MEM, alone or as a global fit with the ACF. The analysis of the shape of the ACF can also be addressed by a mathematical transformation that reduces the dimensionality instead of fitting. This has been done elegantly by a phasor transformation in different contexts first by Gratton's group (Digman et al. 2008 Phasor on Fluorescence Lifetime Intensity Microscopy FLIM [95]; Ranjit et al. 2014 Phasor on short ACF [96]; Scipioni 2016 phasor ICS [76]). Applying the phasor transformation, a similar normalized shape ACFs become near in the phasor plot. We have

used this method to automatically discard rare bright events in different biological measurements (Civita et al. 2024 [97], chapter 3.2).

Local-RICS and other local ICS techniques could be understood in this framework: in these cases, *similarity* is defined by the proximity distance in real space. The reduction of dimensionality could also be addressed in other ways, such as using Principal Component Analysis (PCA). This has been used on the fitted parameters or on the diffusional spectra from MEM. By clustering methods, it is possible to separate different pixels into different classes, making it less user-dependent on selecting the pixels and permitting the exploration of multidimensional distances between diffusional features.

Another way of sampling better the *similarity* is by having better S/N curves. This is a critical step that is involved in all the previous methods. Because the ACFs have a strong structure (shared among all ACFs) and the data points are typically correlated, we considered using this information as a *naïve* filter to estimate the noise of a measurement. Besides this deterministic method, we tried to use a deep neural network to extract diffusional parameters directly from the fluctuation. This work is ongoing, but recent findings by Wohland et al. 2023 [98] encourage further exploration.

To summarise: after this single-pixel analysis, we mapped the heterogeneity of the sample, discovering which region satisfies the ergodicity hypothesis and avoiding artefacts in the analysis. Then, we can proceed using the local-FCS approach to create classes of pixels. These higher S/N groups' ACFs, which respect single pixels, can be used to recover diffusion coefficients with higher precision and accuracy (Figure 11).

3.1 Intensity as simple *similarity* measurement

The use of fluorescent markers is particularly effective in resolving the spatial heterogeneity of different biomolecules. The contrast provided by variations in fluorophore concentration is, in fact, the simplest measurement obtainable with fluorescence microscopy. Other means of contrast, such as polarization state, lifetime, emission spectrum, or pH, represent more complex measurements. To begin the discussion on local-FCS, we use the concept of fluorescence intensity as a feature to identify regions where *similar* phenomena occur.

A classical single-point FCS measurement could be easily performed in a relatively simple system where different intensity levels can identify distinct phases. However, to achieve statistically significant results, multiple measurements are required. Moreover, most commercial setups are not designed to halt the galvo-scanner at a fixed position to record intensity fluctuations necessary for a traditional FCS analysis. In some cases, there is also the issue of not knowing the precise size of the PSF (point spread function) in advance, which adds complexity when attempting to measure diffusion.

To address these limitations, if the characteristic diffusion times are slower than the repetition rate of a scan line and there is no need to investigate rapid photodynamic transitions, a "temporal line-FCS approach" can be used effectively. For cases where the diffusion is faster, a spatial local-RICS approach could be applied, but it will not be shown. The temporal line-FCS method has already been successfully employed in Di Bona 2019 [66] to measure the differing mobility of GFP across various chromatin regions. In the following section, this method will be resumed with additional considerations regarding the experimental protocol.

This method involves calculating the temporal autocorrelation function $G(x,\tau)$ at each position, treating each location as an independent measurement. The $G(x,\tau)$ function becomes particularly insightful when the scan (whether along a line or a circular path) crosses multiple compartments or phases. In such cases, the resulting $G(x,\tau)$ image will capture the distinct dynamics as a function of the position x, as illustrated in the next paragraph.

This method is useful for several reasons:

1. Signal-to-Noise Improvement: By averaging the autocorrelations corresponding to those that come from the same region, there is an increase in the S/N of the autocorrelation curves. This improvement is proportional to the square root of the number of positions averaged.

2. Bleaching Reduction: respect the single pixel FCS measurement, the scans over a region reduce the excitation dose, providing a better ACF curve (if the dynamics are slow enough)

3. Calibration-Free Measurement: It provides a calibration-free way to assess the ratio of diffusion between different phases. This is useful when a precise calibration measurement is not practical, such as in cases where differences in substrate thickness or other experimental limitations prevent accurate calibration.

In this modality, in which each position is considered an independent measurement, the user can choose the sampling distance for the measurement without strictly adhering to the Nyquist criterion. Oversampling could be discouraged as it can lead to increased photobleaching. With this temporally resolved method, if the aim is to analyse only a few discrete points (without utilising pair correlation analysis to estimate the PSF size), measurements can be taken at fewer points spaced more than one PSF apart to ensure independent measurements. Using the same scanning frequency, reducing the number of pixels increases the dwell time in a confocal system and yields more photons. This leads to an improvement of the S/N of the resulting curves. A camera-based system can also achieve this by acquiring a single line at a high frame rate using a de-magnifying lens, as is commonly done in Single Molecule Localization measurements. In a confocal setup, multiple lines can be acquired, although returning to the same point will naturally take longer, reducing the effective frame rate. If the backward scan is also acquired, it is typically necessary to calibrate the phase shift between forward and backward scanning. A more straightforward approach is to offset the even-numbered lines (those acquired on the mirror's return) to create a seamless continuation of the odd-numbered lines. This way, losing the possibility of spatial cross-correlation analysis, it can effectively expand the probed points virtually. This produces a data carpet with dimensions (number of repetitions/2)×2×number of pixels. It is also possible to define two or more thresholds to group similar pixels and analyse the dynamics within these regions, focusing on their distinct diffusional behaviours, as shown in the next paragraph.

3.1.1 Characterization of phase separation in supported lipid bilayer

A relevant case study where we applied the approach of combining FCS curves based on the collected fluorescence intensity was for an investigation of viscosity within a supported lipid bilayer (SLB). SLBs are model membranes that are formed over a solid substrate (typically mica). They are convenient systems for studying the physical properties of a phospholipidic membrane [99]. The measurements performed are particularly useful and interesting within a broader biological context,

particularly in relation to photodynamic therapy (PDT). In recent years, PDT has been proposed as a treatment for various viruses, including SARS-CoV-2 [100]. Specifically, the photodynamic agent under examination is hypericin, a molecule derived from a plant called *Hypericum perforatum* [101].

Hypericin is a lipophilic molecule with a high affinity for biological membranes. When irradiated, it can emit fluorescence and trigger the production of singlet oxygen, a very strong oxidant able to damage membranes [102]. It exhibits antiviral properties on enveloped viruses, with light irradiation and unexpectedly also in the absence of light (Delcanale et al. 2022 [103]). One biologically relevant question to which FCS can contribute is whether specific properties, such as viscosity, change after hypericin administration. The model membranes used in this study have a composition that mimics the viral envelope (Mariangeli et al. 2024 [104]). Prior to hypericin treatment, this composition leads to the formation of at least two distinct phases, which are easily detectable through AFM measurements [105]. Specifically, one can refer to an ordered phase (enriched in cholesterol and sphingomyelin) and a liquid phase (composed of unsaturated lipids, such as DOPC and DOPS). The use of DPPE ATTO 647N, a fluorophore with a higher affinity for the liquid phase, highlights this phase separation, as illustrated in Figure 12. The first step of this study is to measure the viscosity of the ordered and disordered phases before applying the treatment. A challenge in these measurements is that the mica substrate beneath the lipid bilayer affects the PSF (point spread function), distorting it based on the thickness of the solid support [106]. The extent of these distortions, and consequently the size of the PSF, varies depending on the position and the sample being examined. This is where the line-FCS method proves to be particularly useful. By scanning along a line, we can gather data from different points within the same measurement, allowing us to sample both phases—ordered and disordered—over a region of several tens of microns, where we can assume the PSF size remains constant. This method allows us to compare the diffusion coefficients (and, by extension, the viscosity) of the two phases without requiring external calibration, making the analysis more straightforward.

Very recently, we have been using this approach to quantify changes in viscosity following the administration of hypericin. While experiments are still ongoing, preliminary results highlight a higher viscosity in the presence of hypericin without excitation.

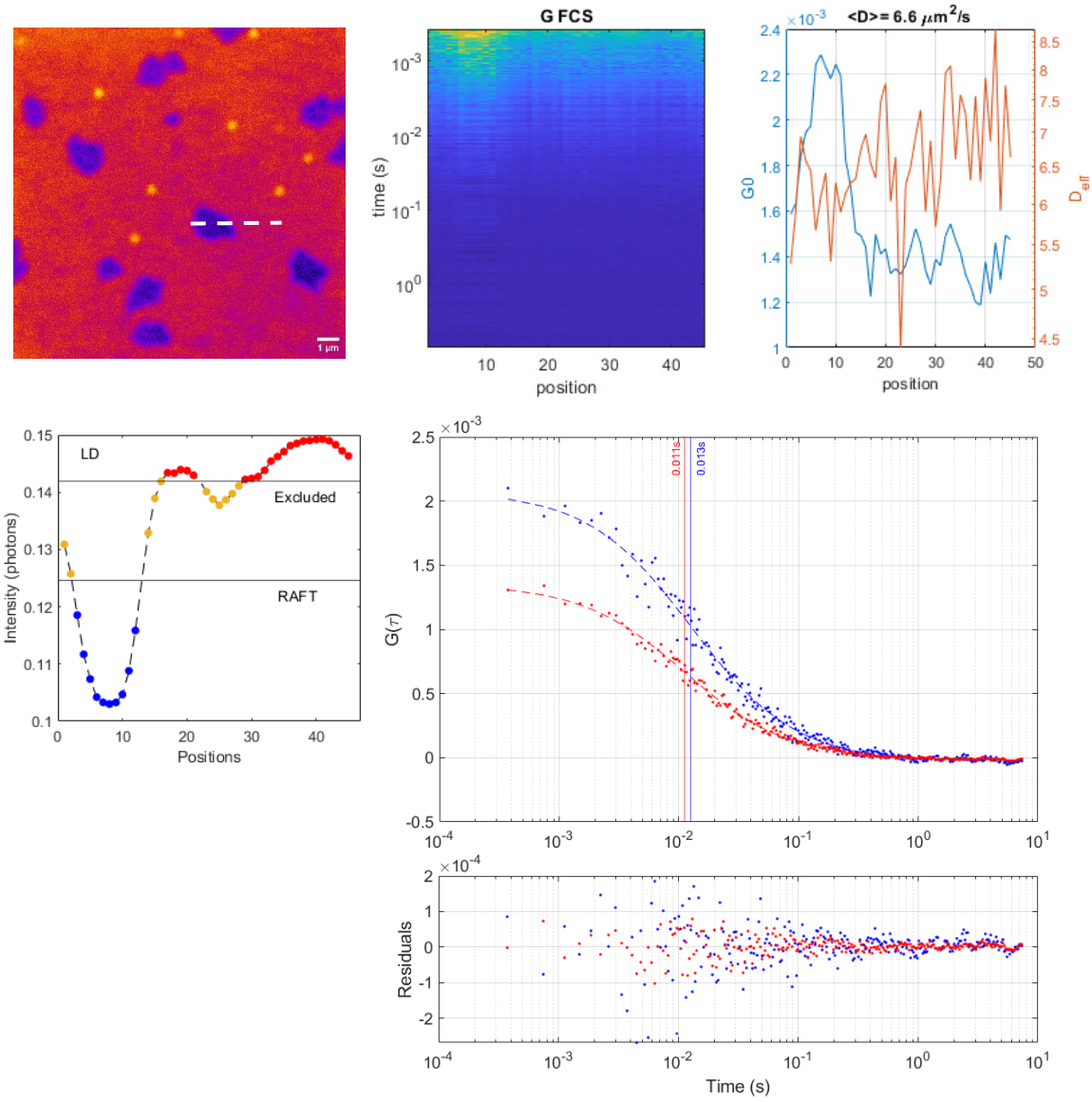

Figure 12 Supported lipid bilayer deposited on mica. Composition: DOPC 66%, DOPS 13%, Sphingomyelin 20%, Cholesterol 1%, fluorophore DPPE ATTO 647N. A) Fluorescence image of liquid-ordered (violet area) and liquid-disordered phases (red area). The dashed line defines where line-FCS is performed. B) single pixel autocorrelation $G(x,\tau)$ of the line FCS. It is clear the autocorrelation with higher G(x,0) that belongs to the liquid-ordered (lipid raft) phase. C) fit of 1c for each $G(x,\tau)$: in red the diffusion coefficient vs position, in blue the G(0). From this analysis, it appears that the diffusion coefficient in the raft is slower, but the precision of the fits is lower than the difference. D) line intensity profile, in which the phases are divided. E) the autocorrelation for the liquid disordered (τ=0.0112 ±0.0008 s) and ordered (τ=0.0126 ±0.0008 s) phases fitted with one component. From this measurement, the ratio between the hydrodynamic viscosity is $\frac{\mu_{LO}}{\mu_{LD}} = 1.13 \pm 0.10$

3.2 Phasor filter to remove rare events

Quite often, during an FCS measurement, a rare bright event occurs. Numerous case scenarios could cause this: i.e. an aggregation of beads in a calibration measurement, a bright and slow vesicle that passes through the confocal volume etc. These events appear as high amplitude ACF shifted to longer lag-time. Averaging the curves that belong to the pool of interest with these rare events strongly deforms the averaged ACF and leads to biased inferred diffusive parameters. The typical procedure to solve this problem is to remove the chunks in which these events occur. For example, in SimFCS, the most advanced program for FCS analysis (available at www.lfd.uci.edu), this is possible through hand selection.

In this thesis, we use a simple phasor transformation inspired by Scipioni et al. [76] to separate the pixels where these slow events occur.

By the element-wise multiplication of the ACF with the sine and cosine function, we compute respectively the s and g:

$$s = \frac{\sum_\tau G(\tau) \cdot \sin\left(\frac{2\pi[\log(\tau) - \log(\tau_{start})]}{[\log(\tau_{end}) - \log(\tau_{start})]}\right)}{\sum_\tau G(\tau)} \tag{89}$$

$$g = \frac{\sum_\tau G(\tau) \cdot \cos\left(\frac{2\pi[\log(\tau) - \log(\tau_{start})]}{[\log(\tau_{end}) - \log(\tau_{start})]}\right)}{\sum_\tau G(\tau)} \tag{90}$$

Where $G(\tau)$ is the ACF, $\boldsymbol{\tau}$ the lagtime at which the autocorrelation is computed. τ_{start} and τ_{end} are the limits of the range between the autocorrelations considered for the phasor transformation. These parameters are usually the $\tau_{start} = \tau_{repetition}$ and $\tau_{end} \approx 15s$ (long lag time at which no Brownian diffusion is ongoing).

After these element-wise multiplications, the ACF became a point in the phasor plot. The position of a Brownian diffusive pool appears on a circle; if the diffusion is confined, the circle becomes wrung, while it is inflated if the diffusion is super-diffusive. For simplicity, we will define the "circle of diffusion" the circle of Brownian diffusion. The position of the circle's centre depends on the τ_x selected; for this reason, the code computes, for each dataset, the position of the diffusive circle, then the circle's centre and the relation between angle and diffusive

coefficients. In Figure 14 C there are present the *circle of diffusion* and the positions for super-diffusive (α=1.5) and sub-diffusive (α =0.5).

Remarkably, the transformation leads to a normalisation of the ACF and the position in the phasor plot is related only to the shape of the ACF, losing the information on the amplitude.

Using this method, isolating the chunks that belong to rare events is simple and fast as they appear as separated points in the phasor plot.

If only one diffusive population is present in an ACF, this is a fit-free method to recover the diffusive coefficient by just multiplications. An arctangent transformation makes this from the ratio of s and g. This angle is then projected on the diffusion circle, decoding a diffusion coefficient.

Contrary to what happens in the FLIM phasor plot (where the functions are exponentials), the presence of more than one diffusive population does not lead to a position in the phasor plot between the population's diffusion coefficients. In this case, the position is related to a weighted average diffusion coefficient. For this limitation that could not be resolved by increasing the harmonics used in the phasor approach, the phasor method has to be considered a qualitative method for discriminating where the diffusion is faster or slower on average.

This does not preclude the method's effectiveness in excluding rare events from the averaged ACF and having a fast visualisation of the average diffusion coefficient present in a chuck by just looking at the shape of the ACF.

3.2.1 Simulation Example

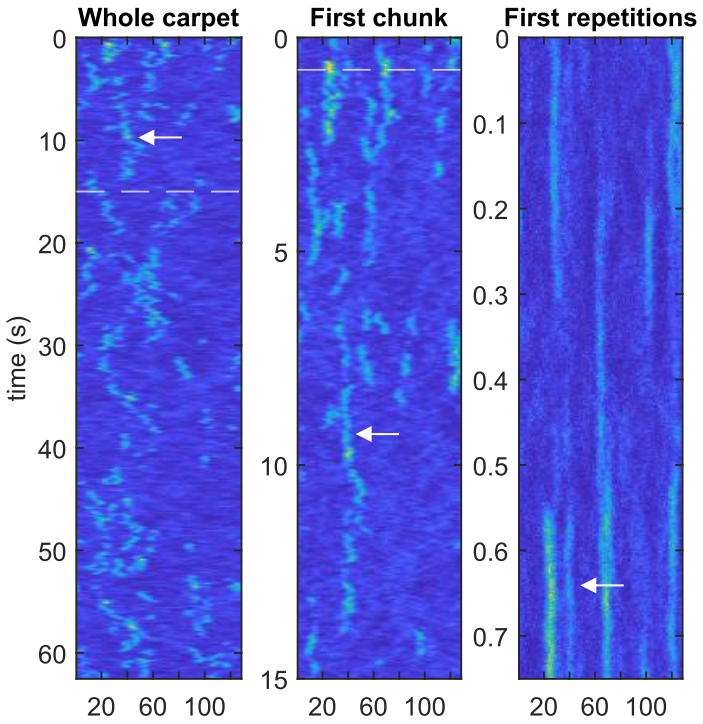

Figure 13 Carpet of the simulation with rare bright aggregates (highlighted by the white arrows) at three different temporal scales. The x position is relative to the position of the scan. On the y-axis, the time of acquisition. The first graph represents the whole temporal acquisition, the second is a zoom of the first chunk (represented by the dashed line in the first graph) and the third graph represents the first 0.75 s of the acquisition (dashed line in the second graph).

In this simulation, two diffusive populations with the parameters are present in the table. These parameters are chosen to simulate the case scenario of a fast diffusive pool with some rare and bright aggregates, similar to the one found in the real measurement presented in Chapter 3.2.2. The total length of acquisition is around 60s with a repetition time of a line of 125 us (500 000 repetitions), with 1kcps of background. At the end of the simulation, we added Poisson noise.

	1st Component 1	2nd Component
Diffusive coefficient ($\mu m^2/s$)	0.5	0.05
Brightness (kcps per molecule)	1	10
Concentration (molecules/μm^2)	24	1.2

As is clear from the carpet in Figure 13, where the x and y axes refer to the pixel position along the scanning line and the acquisition time, there are some bright columns that represent the brighter aggregates in a sea of faster-moving beads. Applying the phasor transformation (Figure 14), it is clear that two populations of chunks are present: 1) less populated in the upper part of the phasor plot (faster diffusion) signed by a black circle, 2) a more populated near the middle of the circle of diffusion (slower diffusion) signed by a green circle. Confronting Figure 14A and B, the positions of the slower brighter beads colocalise perfectly with the slower chunks identified by the "phasor radial transformation". This last map colours each chunk's angle position in the phasor plot. We could cluster all the ACFs by distance in the phasor plot to get quantitative measurements of these two diffusional pools. The chunks not affected by the slower diffusion beads are the ones encircled by black. The chunks selected are displayed in D. In F is present the averaged ACF with the fit that reports that is present only one component with D=0.44 $\mu m^2/s$. Analogously, figures E and G are for the chunks with an average slower diffusion behaviour, which was selected by a green circle in C. From the fit, it is clear that there are two diffusive pools: one with 0.52 $\mu m^2/s$ and one with 0.049 $\mu m^2/s$.

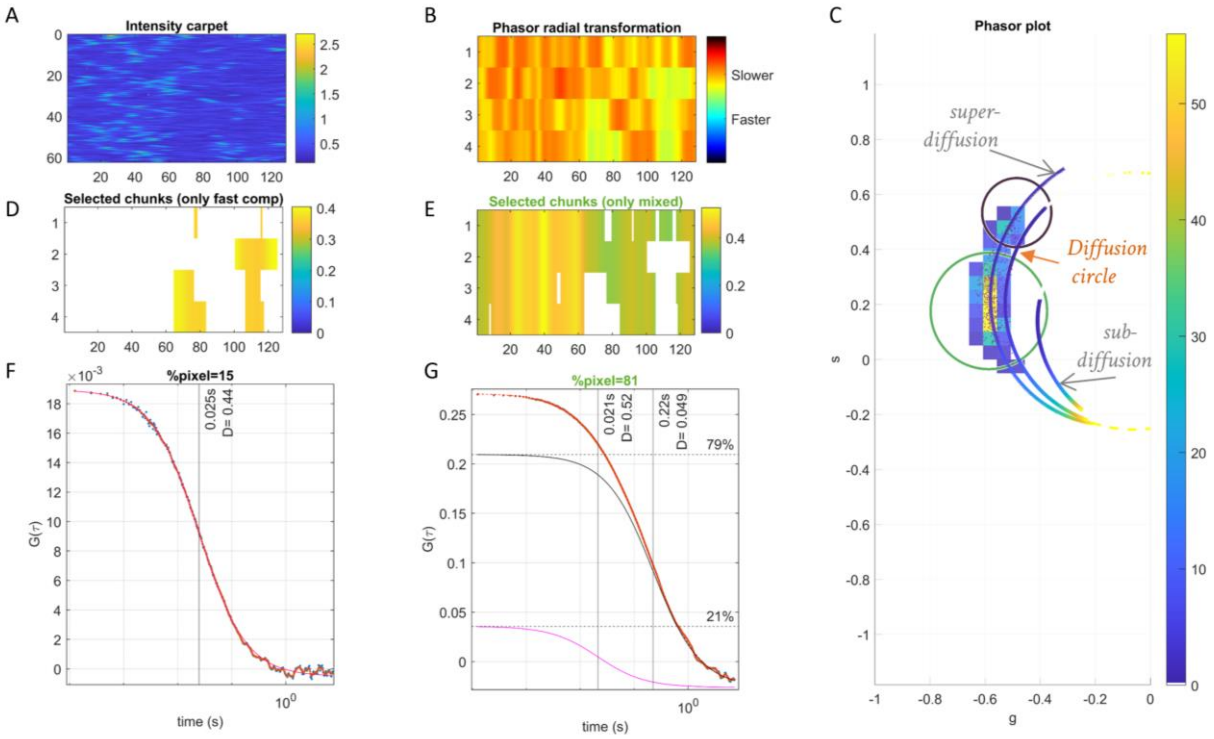

Figure 14 Phasor plot filter to segment the diffusional species. A) Intensity carpet. B) Phasor transformation that highlights the presence of slower beads (red pixels) against their absence (green pixel in which faster dynamics occurs). C) Phasor Plot of the diffusion: in the upper part ($s > 0.4$) are present, as small orange dots, the chunks in which only a fast diffusion pool is present (encircled by black). On the lower part (s around 0.2) are present the majority of the chunks (the histogram reports > 50 chunks) in which both populations are present. The green circle selects these chunks. D) Selected chunks for "only fast diffusion" pool black circle. E) selected chunks for "mixed pools" green circle. F) Autocorrelation of the "only fast diffusion" pool autocorrelation function fitted with 1 component with D=0.44 $\mu m^2/s$. G) Autocorrelation of the "mixed diffusion" pools autocorrelation function: 2 components with D1=0.52 $\mu m^2/s$ and D2= 0.049 $\mu m^2/s$.

For this simple example, it could be possible to sort the autocorrelation with the average intensity instead of using the phasor. This would select the same chunks for the mixed and unmixed species. The advantage of the phasor method is that contrary to the intensity-based approach, it also works if the average intensity is very similar, as it will be shown in 3.3.1.

3.2.2 Study of PDL1 by spot variation STED-FCS

This phasor approach of selecting and discarding rare events has been used with profit in Civita et al. [97].

In this study, we focused on investigating the distribution of PDL1, a membrane protein that plays a significant role in immune regulation, especially in different cancers. We used a combination of fluorescence microscopy techniques, such as single-molecule localization microscopy and FCS, to discover how PD-L1 organizes itself in nanoclusters on the membrane. These clusters, which we have observed in various experimental setups, are believed to be associated with the lipid-rich regions of the membrane, such as cholesterol-enriched lipid rafts. Understanding this organization helps clarify PD-L1's role in cellular signalling and its potential as a target in immunotherapy.

More in detail, we conducted studies on fixed cells using various super-resolution techniques (SPLIT-STED [107] and directSTORM [108] [109]). This led us to discover a nanometric clustering organization of this protein, with a typical radius of 30 nm. Furthermore, functional colocalization measurements revealed a co-presence, at a resolution scale of 150 nm typical of Image Scanning Microscopy [110], with proteins commonly associated with lipid rafts (glycosylphosphatidylinositol (GPI) and caveolin-1 (Cav-1)).

These results were obtained on fixed cells, and to gain a deeper understanding of this protein's behaviour in living cells, we decided to explore the dynamic aspects through FCS. We employed the Spot Variation approach (par 2.1.3) to determine whether the movement of the protein was confined, free, or super-diffusive, comparing it to GPI, a protein with known sub-diffusive behaviour reported in the literature. To achieve this, we induced the expression of the PDL1+EGFP protein via transfection and performed line-FCS measurements under confocal and time-gated STED (gSTED [111]) modes (confocal: ω_{xy} = 210 nm; gSTED: ω_{xy} = 80 nm) on living cells. In comparison with classical STED measurement, gated STED relies on discarding the photons that arrive in a determined temporal window. Since the probability of the emission of the photons is linked with the intensity of the depletion beam, the emitters that are in the zero intensity centre of the depletion beam will have a longer lifetime. On the other hand, the emitters not in the centre of the depletion beam will be favoured for emitting at a faster temporal scale. Using this information makes it possible to shrink the STED resolution further.

As shown in the fluorescence carpets in Figure 15, the analyses revealed at least three diffusive components. This complexity will be further unmixed using the phasor filter. The carpet a) is long around 220s and there are present *quasi*-vertical lines representing very slowly diffuse aggregates. The diffusion coefficient is estimated to

be <0.001 μm^2/s, which corresponds to a $\tau_d > 15\,s$ compatible with the movement of the cell. We will refer to these aggregates as *clusters*. If we segment the FCS traces with a chunk length 15 s, we will have excluded this component from the ACFs' contributions. Moreover, a good practice is to detrend before doing the segmentation to correct slow xy drift/photobleaching/very slow movement of the cell/very slow movement of aggregates. In this case, we used a random number approach with a moving average of 8 s [80]. With this setting, we are sure that this contribution will not affect the analysis. Besides this filtered *cluster*, other slow and bright objects appear on the carpet, highlighted by the black arrows. By microscope images not reported here, they are presumably vesicles. Since they are not everywhere in the carpet, the phasor approach can efficiently filter the chunks in which they are present. By phasor selection, reducing the contribution of these slow and bright objects, the diffusion coefficient of the PDL1+EGFP on the membrane can be recovered more precisely, unmixing different diffusional contributions. Typically, more than 60% of the chunks are conserved.

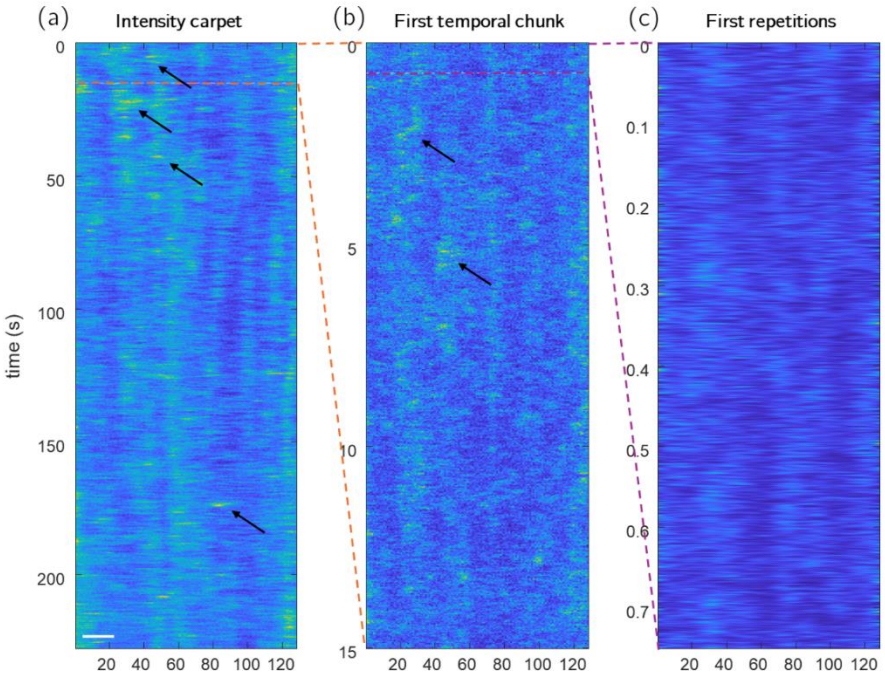

Figure 15 Comparison of PD-L1 diffusion at different temporal scales at confocal resolution according to "carpet" representation, where the x and y axes refer to the pixel position along the scanning line and the acquisition time, respectively. The pseudocolour scale accounts for fluorescence intensity. a) Carpet of whole acquisition (around 220 s): very slowly moving aggregates (possibly *clusters*) are visible as quasi-vertical brighter lines. The arrows show brighter slow-moving spots that may be identified with vesicles (diffusion coefficient < 0.05 μm^2/s). b) First 15 s of acquisition, where vesicles are still visible. c) The first 750 ms of acquisition shows the PD-L1+EGFP slow-diffusing component as

brighter lines. In this last carpet a Gaussian filter with $\sigma = \omega_{xy}$ was applied for better visualization. Scale bar 1 μm.

The autocorrelation using a time-gated STED-FCS (gSTED) for squeezing the PSF to $\omega_{xy} = 80$ nm makes the ACF signal-to-noise very low. For this reason, we keep only the autocorrelation chunks with a value of G0>0.1 (Figure 16). The results obtained from analysing the autocorrelation are confirmed by the cross-correlation approach (in which no chunks are discarded) (Figure 17). In particular, we fit the ACFs obtained with a confocal volume FCS with a two components model (for both GPI and PDL1) and with only one component for the gSTED measurement. This is because the strong reduction of the xy waist of the focal volume by gSTED prevented the observation of the faster component of PD-L1+EGFP and GPI+EGFP, given the maximum time resolution of our apparatus (0.125 ms/line).

With these strategies we measure for confocal setup D_{fast}=5±1 μm²/s D_{slow} =0.24±0.02 μm²/s, for PD-L1+EGFP; D_{fast}=5±1 μm²/s, D_{slow} =0.48±0.05 μm²/s for GPI+EGFP. Appling the gSTED we found for the slower components PD-L1+EGFP: D=0.19±0.02 μm² /s; GPI+EGFP: D=0.31±0.03 μm² /s.

Spot-variation analysis revealed a statistically significant reduction of the diffusion coefficient with spot size for GPI+EFGP (Figure 18), in agreement with the confined motion reported for raft-associated GPI [51]. For PD-L1+EGFP, we indeed observed a D reduction upon squeezing the diffusion spot, albeit the statistical significance was borderline (Figure 18).

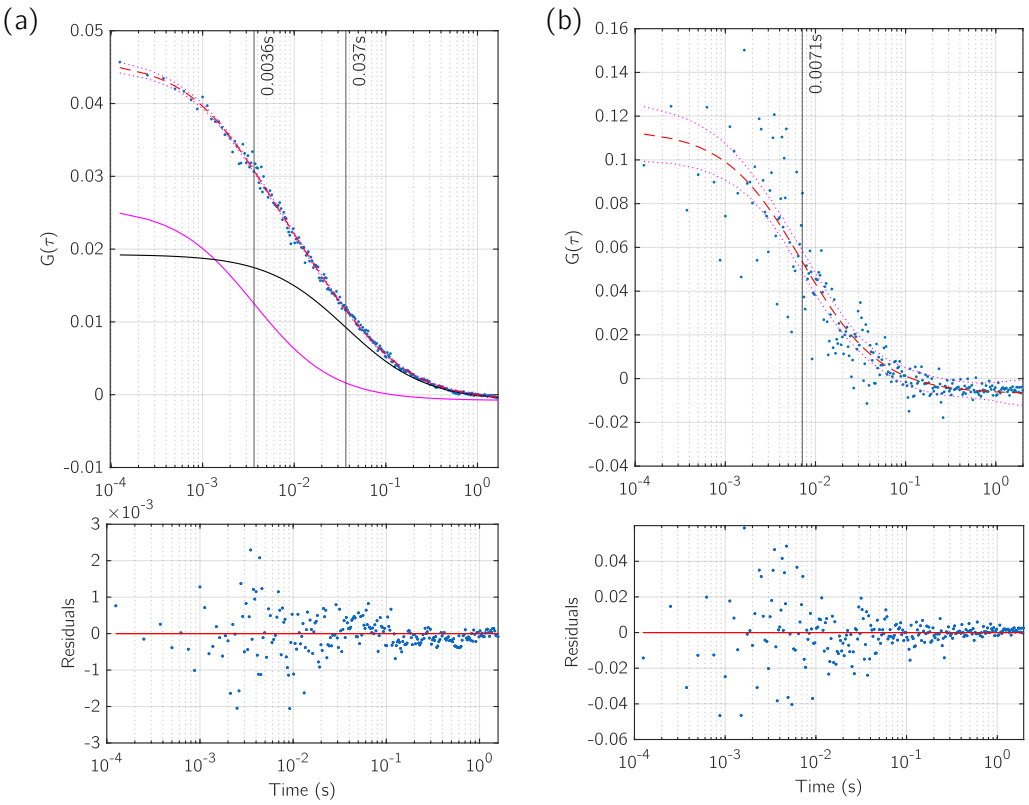

Figure 16 Representative ACF from line FCS measurements of PD-L1+EGFP without a) and with b) gSTED. After detrending, the general autocorrelation G(τ) was obtained as the average of the 128 single autocorrelation functions, filtered with the phasor approach to remove the brighter slow-moving (Figure 15), and recovered for each pixel along the scanning line. (a) In confocal mode, G(τ) was fitted with a sum of a fast (pink curve) and a slow (black curve) 2D isotropic diffusion functions (red dashed line); D_{fast} = 3.0 μm^2/s and with D_{slow} = 0.3 μm^2. (b) In gSTED mode, G(τ) was fitted to a single slow 2D isotropic diffusion (red dashed line) with D = 0.22 μm^2/s. The residual panels are shown at the bottom.

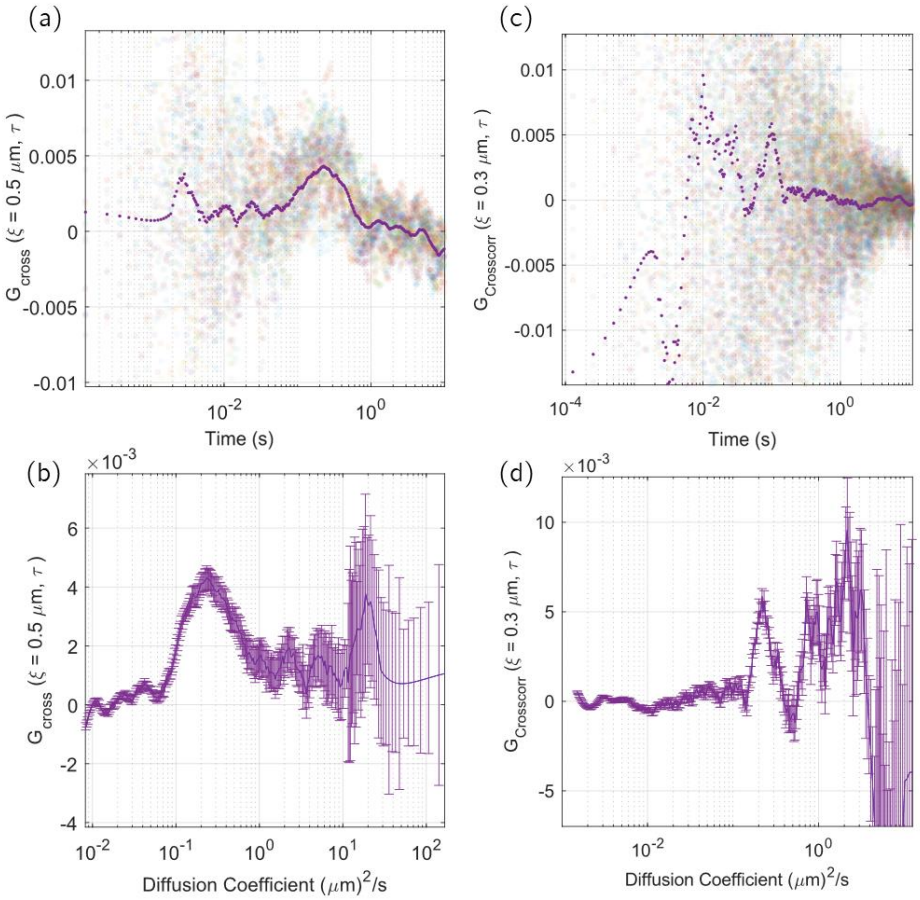

Figure 17 Cross-correlation analysis of the same measurement presented in Figure 16. a) cross-correlation computed at a distance of 500nm vs time-lag in the confocal setup: purple dots are the average of 57 pixels (coloured semi-transparent dots). b) The same cross-correlation with the error bar represents the standard error of each point vs the diffusion coefficient. Cleary visible the peak at D_{slow} = 0.26 μm^2/s (where the autocorrelation reported 0.3 μm^2/s). c) cross-correlation computed at a distance of 300 nm in a gSTED setup: the purple dots are the average of 25 pixels. d) the same dots with the error bar of the SE. The first peak is at D = 0.20μm^2/s (where the autocorrelation analysis reports 0.22 μm^2/s)

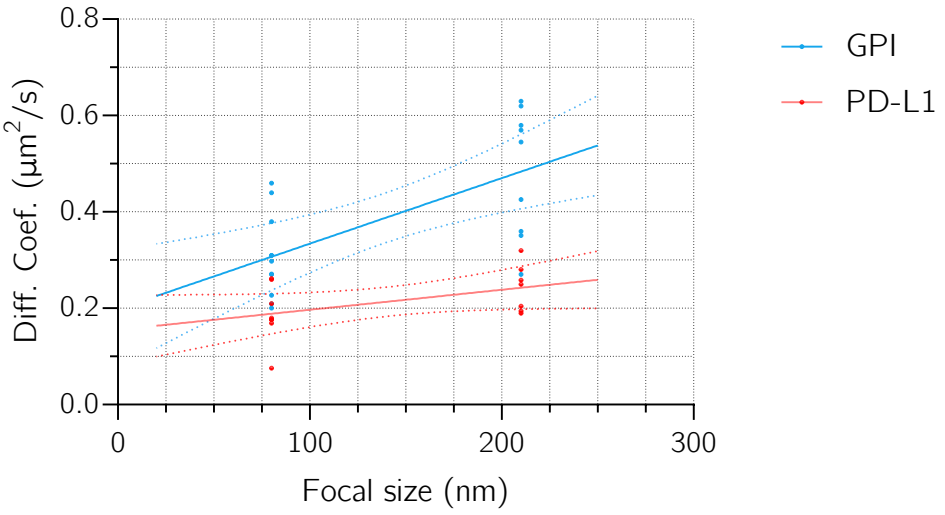

Figure 18 Spot-variation analysis of PD-L1+EGFP (red) and GPI+EGFP (blue). The diffusion coefficient of each protein is plotted at confocal (210 nm) and gSTED (80 nm) xy resolution, together with the linear fits (full lines) and the 95% confidence range (dashed lines).

3.3 Diffusional maps

The concept of local-FCS is based on the hypothesis that similar molecular behaviours are present within certain spatial regions. By quantifying diffusional characteristics on a pixel-by-pixel basis, we can generate maps for each feature. *Similar* dynamics occur in pixels that share comparable values across different maps.

Creating diffusion maps can be seen as a method to reduce the complex information stored in fluorescence fluctuations into a few easily interpretable parameters, a dimensional reduction from millions (billions) of intensity points to a couple of physical parameters. The first dimensional reduction occurs through the computation of the autocorrelation function (ACF), which reduces the data space by a factor of about 100 to 1000.

During my PhD, we explored an alternative approach for data reduction using neural networks, specifically Long Short-Term Memory (LSTM) algorithms, to quantify the persistence of molecules within the probing volume and classify the diffusional behaviour into 16 different categories (like a MEM approach). Recently, Wohland's group published methods utilizing convolutional neural networks (CNNs) to extract a single diffusion coefficient for each fluctuation series [112]. This method creates diffusion coefficient maps from fluctuation matrices, and they demonstrated that it reduces the acquisition time required by a factor of ten compared to traditional autocorrelation methods while maintaining precise and accurate inferred values. These successes of the Neural Networks approaches rely on the fact that fluorescence fluctuations contain a vast amount of information that cannot be fully compressed by calculating the autocorrelation function. Indeed, other deterministic methods that do not rely on the ACF computation have been proposed. Among them, Number and Brightness (N&B) [113] or higher-moment analyses [114] extract relevant information by the temporal traces through the momenta computations. Undoubtedly, future developments with neural networks will aim to extract more information directly from fluorescence fluctuations beyond the current autocorrelation approaches.

Typically, autocorrelation curves contain approximately a few hundred logarithmically equally binned points for each spatial location. The subsequent information compression in a few maps can be done in different ways, depending on the specific biological question. A typical question might be: How fast does the biomolecule move at this position, on average? This could be represented by describing the diffusion using a single-component model. By fitting the autocorrelation functions with this theoretical model (eq. (40)), we can obtain three diffusion maps: the number of molecules present in each position (represented by N), the diffusion coefficient D, and the goodness of fit quantified by the chi-squared value or the coefficient

of determination (R^2). However, as previously explained, in a cellular context, molecules are unlikely to exhibit purely Brownian motion. Therefore, obtaining information on where molecules diffuse freely and where they do not could be interesting. The degree of freedom represented by the anomalous diffusion parameter α allows for a better description of the autocorrelation curves (eq. (41)). In this case, an additional map of α is generated. The vast temporal range probed by FCS techniques enables the investigation of different phenomena or dynamics at the same spatial position. The contributions of some of these, such as photobleaching or cellular movement, can be mitigated, as discussed in detail in Section 2.1.11. However, having multiple diffusive populations coexisting at the same location is common. Therefore, describing the autocorrelation functions using a generic bi-component model for each pixel is often necessary. In cases where only one population is present, the algorithm should report a low fraction for the second population. For typical imFCS curves, the signal-to-noise ratio does not allow for precise inference of the diffusion coefficients obtained. In this model, we are utilizing five parameters. In the context of a low signal-to-noise ratio, incorporating prior information can be beneficial to enhance this procedure, as will be explained in detail later in this chapter. The phasor transformation previously introduced provides an entirely different approach to answering the first question. The autocorrelation curve is compressed into two coordinates, which can be associated with an *effective* diffusion coefficient.

Another, more quantitative alternative to the phasor method is the use of the maximum entropy method. This technique enables the generation of diffusion maps by fitting the autocorrelation curves as introduced in 2.1.13.

As will be shown, there is no universally superior method; each has advantages and disadvantages. The following paragraphs present simulations and a biological case study using these methods. We will explain the pros and cons of all methods in these two case scenarios.

3.3.1 The simulation

To validate and rigorously test our analysis methods, we developed a comprehensive platform for simulating FCS experiments and analysing their results. For this purpose, we created a simulated temporal stack with distinct regions, each displaying unique diffusional behaviour. The simulation consists of 40,000 frames with an exposure time of 2 ms. Three types of molecules are present in the simulation, all having the same brightness of 10 kcps, which is compatible with EGFP brightness [115] in living cells. The molecules diffuse bidimensionally across a square surface of 16 μm per side. The diffusion coefficients of the three species are as follows:

$a = 1\ \mu m^2/s$ for fast molecules

$b = 0.1\ \mu m^2/s$ for slow molecules

$c = 0.5\ \mu m^2/s$ for medium-speed molecules

Figure 19 presents the temporal average intensity of the stack that clarifies the following geometry.

The average density of the faster molecules is 31 molecules/μm^2, corresponding to approximately 2 molecules per PSF, and these are present everywhere except in the regions C3 and E.

The central circle C1 is populated by 75% of *a* molecules and 25% of *b* molecules.

The triangle T contains 50% *a* and 50% *b* molecules.

The small circle C2 contains 25% *a* and 75% *b* molecules.

The ellipse E is populated solely by *c* molecules.

The circle C3 contains only *b* molecules.

These last two regions are populated in a way that preserves the overall average density, making them indistinguishable when analysing only the intensity. Additionally, 24 slow molecules (species b) move inside a tube L with a width of 20 nm, corresponding to a very low linear density of 1.5 molecules per μm.

The dynamics of the individual molecules were simulated using a Monte Carlo simulator called MCell (Stiles, JR, et al. [116]). Using this tool, the dynamics of individual molecules were simulated, with the output being a list of the positions of the molecules for each frame. In MATLAB, a matrix representing the fixed-size photosensitive elements of a camera was created. The molecular positions were imported and convolved with a Gaussian representing the PSF. This probability density was then multiplied by the number of photons each molecule emits per unit acquisition

time. To simulate a noisy measurement (paragraph 3.3.3) a Gaussian noise of a variance of 10 times the signal is added. The Poissonian noise is added to all simulations.

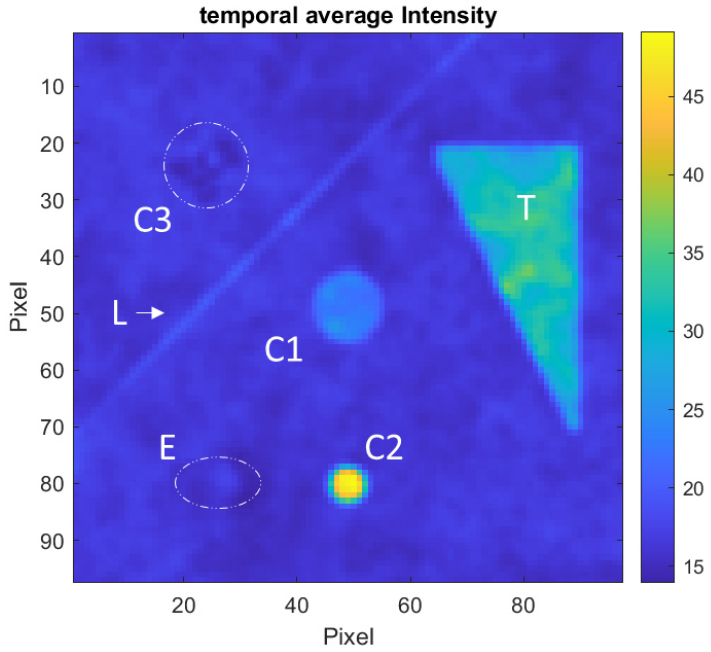

Figure 19 Temporal average intensity of the simulations, with the different diffusive regions highlighted in white.

tICS & iMSD

Even with an extremely high signal-to-noise ratio, it is still very challenging to accurately select the mathematical model that correctly describes the diffusion process. By observing the curves in Figure 20, it seems that both the models, anomalous single component and Brownian two components, fit the data almost perfectly. The subtle trend present in the first fit is nearly negligible in a real measurement, where the PSF is not perfectly Gaussian, and/or there is some level of correlated noise within the acquisition system or from dynamic factors within the sample (such as bleaching, sample movement, autofluorescence, etc.). Despite this, the tICS measurement provides a global and accurate description of the system when described using a two-component model (Fig. b), yielding diffusion coefficients of D1 = 0.988 ± 0.001 $\mu m^2/s$, with G1r = 92%, and D2 = 0.0692 ± 0.0005 $\mu m^2/s$. If, on the other hand, the system is modelled as a single component undergoing anomalous diffusion, the curve is characterized by an α value of 0.860 ± 0.005 and an effective diffusion coefficient D_{eff} = 0.54 ± 0.02 $\mu m^2/s$. However, this latter description is less consistent with the original simulation parameters. A summary of the iMSD analysis is shown in Figure 21. As for the tICS analysis,

the immobile fraction is subtracted by the novel filter method described in 2.1.10. iMSD fit reports a diffusion coefficient of 0.75 ± 0.01 μm²/s in the first second of lag time. It has to be highlighted that the considerable compression of all diffusion-related information over such a large area makes it challenging to obtain accurate measurements from a global iMSD analysis, even though the signal-to-noise ratio is remarkably high. The inferred diffusion coefficient represents an average of the diffusion coefficients of the simulated populations.

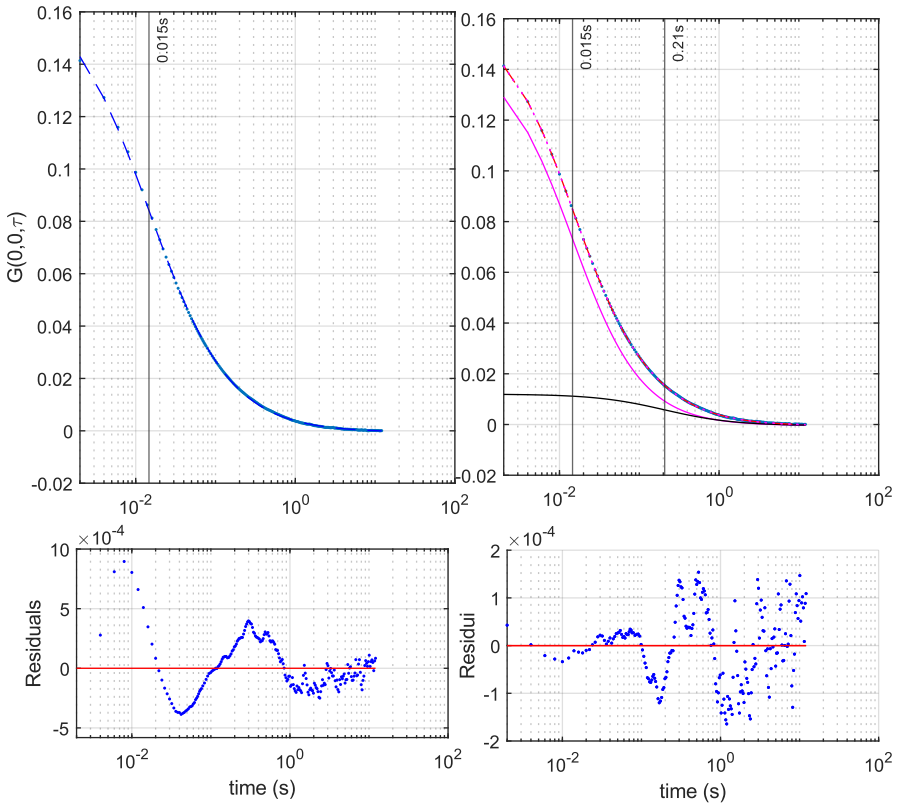

Figure 20 tICS curve fitted with different models: on the left with a single component model with anomalous diffusion (α = 0.75 ± 0.01 μm²/s D_{eff} = 0.54 ± 0.02 μm²/s), on the right with two components (D1 = 0.988 ± 0.001 μm²/s, with G1r = 92%, and D2 = 0.0692 ± 0.0005 μm²/s). The vertical lines indicate the characteristic times of each component. The residuals are displayed at the bottom. The $G(\xi, \chi, \tau)$ is filtered with the novel method proposed in 2.1.10 to remove the immobile fraction.

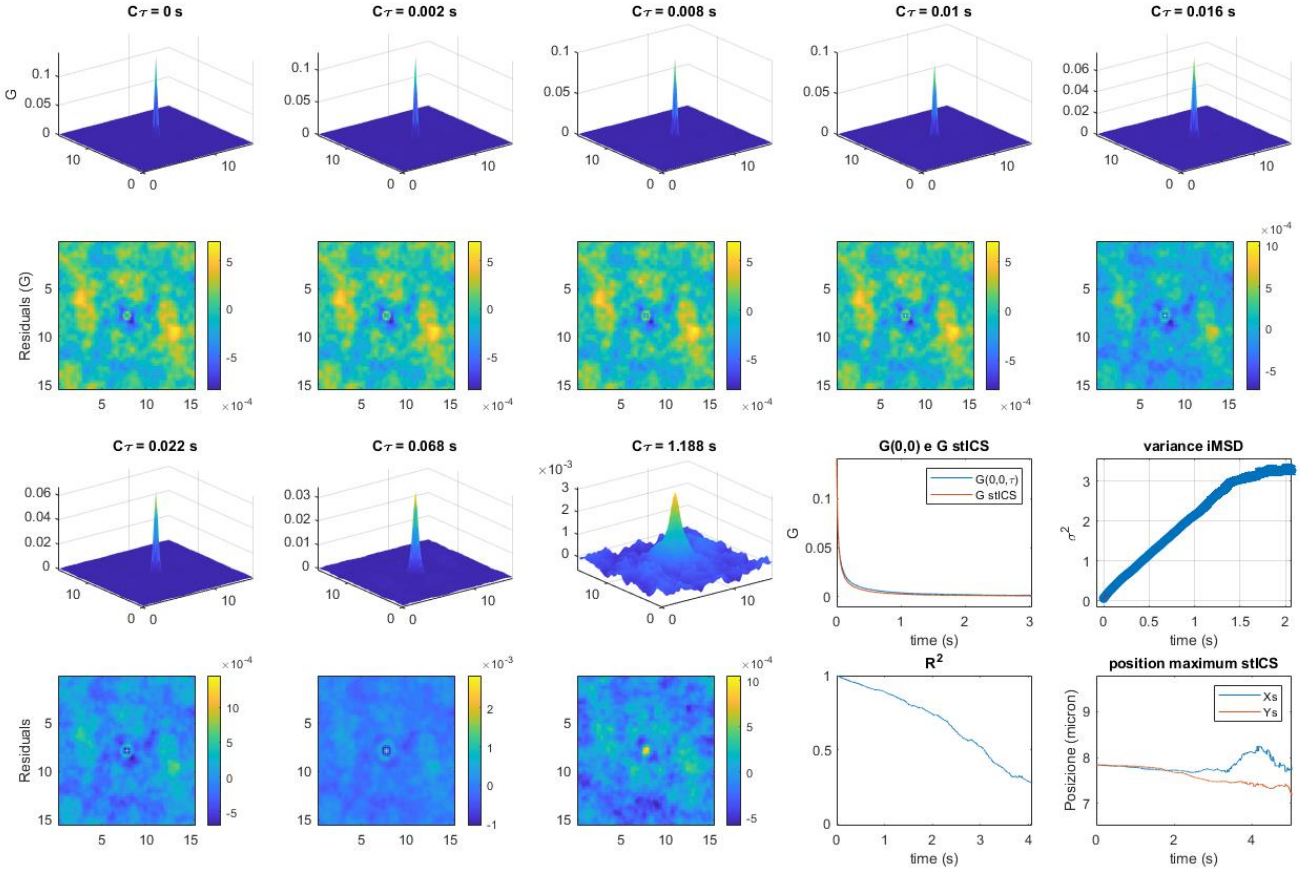

Figure 21 $G(\xi,\chi,\tau)$ fitted with stICS formula. The first and third rows show $G(\xi,\chi,\tau)$ computed at different lag-times τ. The correspondent residuals are displayed in the second and fourth rows. At the bottom right, the plots show the fitted parameters vs time (s). Including the variance analysis (iMSD). While the fitting is highly accurate for $\tau<1$, the variance fitting (iMSD analysis) demonstrates limited accuracy, yielding a diffusion coefficient D=0.75 $\pm$ 0.01 $\mu m^2/s$ and failing to capture insights for a two-component model.

Fit 1C

A more accurate way to investigate diffusion characteristics is to analyse them at the single-pixel level. Various diffusion models can be selected to describe the dynamics. As mentioned earlier, reducing the complexity of the analysis to a single spatial point allows for the use of simpler theoretical diffusion models compared to what is required for analysing larger areas (as in the case of ICS approaches). For this reason, we chose to fit the autocorrelations with a single-component (1C) model that includes the anomalous diffusion parameter α (eq. (41)).

In this simulation, the signal-to-noise ratio is very high, so we do not attribute the failure to accurately describe the dynamics in different regions to noise. As shown in Figure 22, the diffusion coefficients in regions with a single component are correctly identified on average. In the homogeneous region, there is a deviation from the simulated coefficient of 1 $\mu m^2/s$: an increase in the effective diffusion coefficient is correlated with a reduction in α, suggesting confinement effects. This is particularly interesting as it demonstrates FCS's ability to identify barriers simply by detecting a less steep decline in the ACF shape. In this simulation, reflective walls are present at the edges of the image. Additionally, the region where the tube containing 24 confined molecules is correctly described by a confined diffusion. The amplitude G0 correctly reflects an inverse relationship to the number of molecules present in each area.

In the Triangle region, the average diffusion coefficient is 0.5 $\mu m^2/s$. This value is a weighted average between the diffusion coefficient of the *a* molecules (1 $\mu m^2/s$) and that of the *b* molecules (0.1 $\mu m^2/s$), similar to what is observed in region C1. In C2, where the slow population is dominant, the coefficient shifts towards slower diffusion values. The coefficients for E and C3 are correctly determined. The R^2 map shows that the fits are generally good across all regions, with a slight reduction in accuracy within the triangle (consistent with the two diffusive populations).

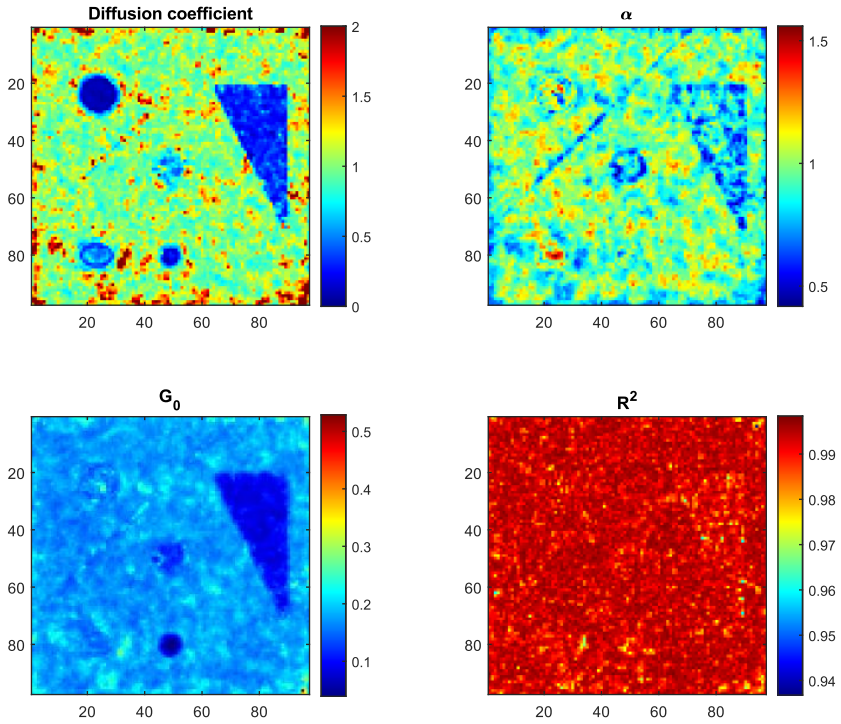

Figure 22 Maps of the fitted parameters, D α G_0 R^2, obtained using the single-pixel FCS applied to the noise-free simulation dataset. The dataset is described with a single component with anomalous diffusion model.

Fit 2C

Although the description using a single component with the anomalous diffusion parameter α appears highly accurate on average, it cannot describe situations where two components are present in the same location. The implementation of two diffusion components can be approached in various ways. The method chosen here ensures that the two diffusion coefficients differ by at least 1.5 times, favouring the existence of two distinct components, even with fractions as extreme as 1:0. This approach is useful because when only one component is present, rather than identifying two diffusive populations with the same diffusion coefficient, it accurately reflects the presence of a single population with a 100% fraction.

In real biological experiments, a free-diffusing component (representing free fluorescent biomolecules) is almost always present and can be identified through techniques such as line-FCS or RICS. If the temporal sampling is sufficient, this

component can also be derived from tICS analysis. For this reason, an effective method for fitting at the single-pixel level is to impose a constraint on the diffusion coefficient, fixing the fast component within a user-configurable interval. This also increases the method's reliability by using prior information in a higher-noisier single-pixel context. For these reasons, the faster diffusion coefficient obtained from tICS was constrained within a ±20% range in these fits.

In Figure 23 the maps of the two components fitting parameters are shown. G1 and G2 represent the fractions of the two populations, respectively. G1r, defined as G1/(G1+G2), represents the relative abundance of the faster population. The offset, as defined in eq.(40), corresponds to the amplitude of the autocorrelation at the longest lag time; on the other hand, G(τ=0)) corresponds at zero lag time. $\tau_{1/2}$ is a calculated parameter that estimates the autocorrelation halving time. This parameter is useful for speeding up the fitting process by providing a starting point and generating a map of the effective diffusion coefficient for a single component. In detail, this estimation is done using the PCA filter discussed in 3.5. τ1 and τ2 are the characteristic times obtained from the fit.

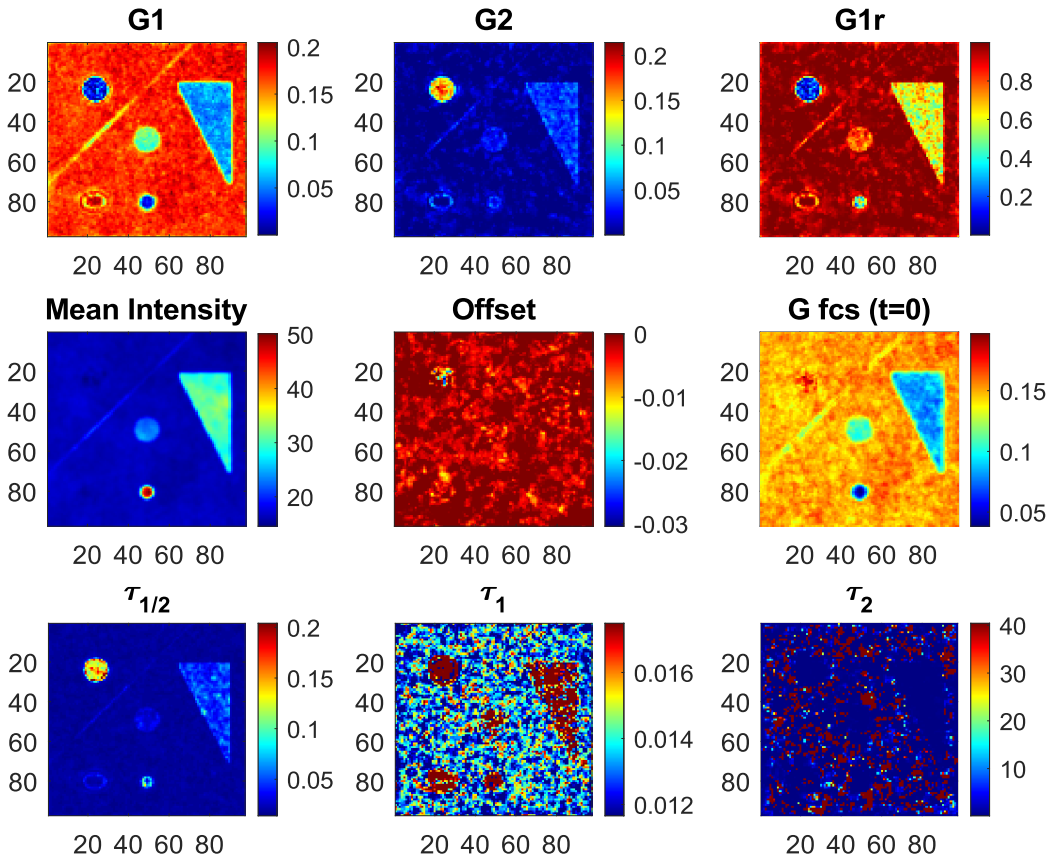

Figure 23 Maps of the fitted parameters obtained using the single-pixel FCS method applied to the noise-free simulation dataset. The dataset is described with a two Brownian component model.

As can be seen in Figure 23, all regions are correctly identified. The G1r map is the most significant in this panel, as it accurately reflects the stoichiometric ratios of the different populations. The two components model effectively describes all the simulated characteristics. Of note is that the offset map shows higher values for slower diffusion processes. As explained in paragraph 2.1.5, this is due to the longer acquisition time required for slow dynamics. In the context of local-FCS, we will leverage the information from the G1r map to select only the fits where fast dynamics occur, allowing for a more precise estimation of the fast component.

Phasor approach

Phasor analysis can be viewed as a fit-free method for obtaining an average diffusion coefficient that describes the ACF. In summary, the ACF is decomposed into two components, s and g, whose position in the phasor plot is linked to the dynamics present in the ACF. The projection onto the phasor plot serves as an effective dimensional reduction to describe the ACF, and, as explained in Chapter 4.2, it can be used to map the diffusion coefficient onto the diffusion circle (Figure 24). This efficient method, without any fitting and in just a few tenths of a second, provides an effective diffusion coefficient for each pixel. The resulting map is similar to the one obtained using a one-component model with $\alpha = 1$. One of the key advantages of this method is the ability to group autocorrelation curves that are close to each other in phasor space. This proximity ensures a high degree of similarity in the shape of the ACF. As previously mentioned, regions can be defined within the phasor plot to identify similar ACF curves. These curves can then be averaged, resulting in a single high signal-to-noise (S/N) curve that effectively captures the underlying dynamics of that region in the phasor plot. In this approach, similarity is determined purely by the shape of the ACF, independent of spatial proximity in real space or from the amplitude of the ACF. In Figure 25, three circles have been defined in phasor space, each corresponding to different diffusion regions in real space (Figure 26). By aggregating the ACFs from these positions in the local-FCS framework, the diffusion coefficients can be obtained with high precision, even in the presence of low signal-to-noise ratios.

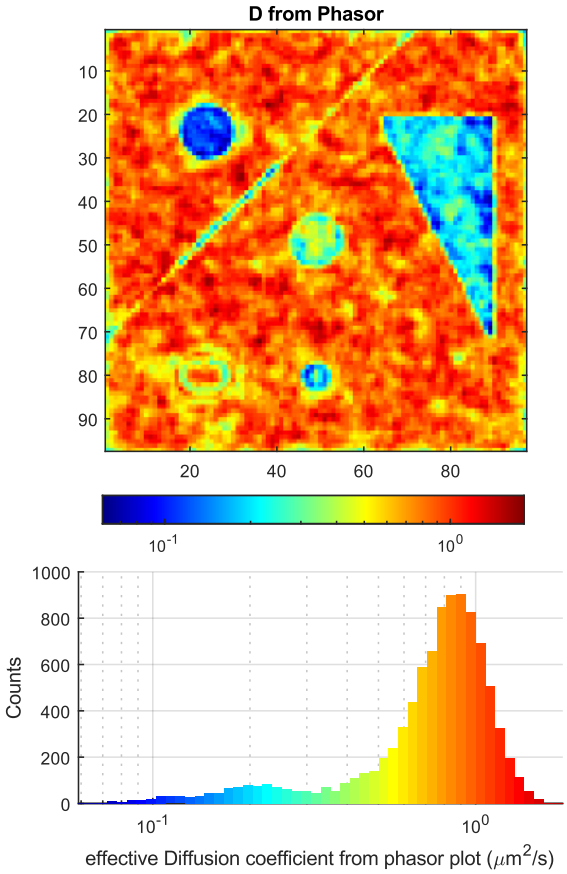

Figure 24 Effective diffusion coefficients (D_{eff}) obtained from single pixel FCS method applied to the noise-free simulation through phasor transformation. The histogram displays the distribution of D_{eff} values, with the majority of pixels correctly showing $D_{eff} = 1\mu m^2/s$. The triangle highlights a $D_{eff} = 0.2\ \mu m^2/s$, representing a weighted average of 1 and 0.1 $\mu m^2/s$. In the circle C3 (at the top left) D_{eff} =0.1 $\mu m^2/s$ is accurately identified.

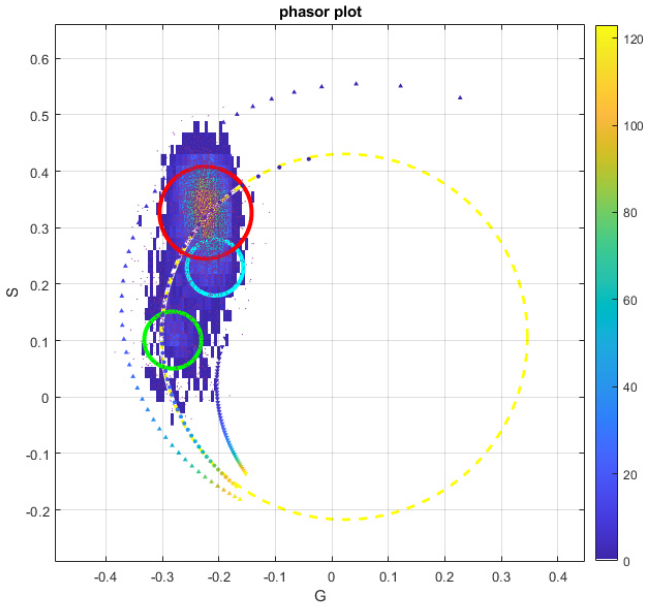

Figure 25 Phasor plot of the single-pixel FCS method applied to the noise-free simulation dataset. The yellow circle is the *diffusion circle* (defined in 3.2) in which the Brownian diffusion ACFs lies. The bi-dimensional histogram highlights the regions in which most ACFs are present. The angular position of the ACFs in the phasor plot, calibrated using the diffusion circle, is used to generate Figure 24. We can identify multiple regions on the phasor plot, and, using a local-FCS approach, we can average the ACFs that arise from those pixels. In this case, three regions are highlighted (in green, cyan, and red circles). Figure 26 illustrates their respective positions in real space along with the corresponding averaged ACFs.

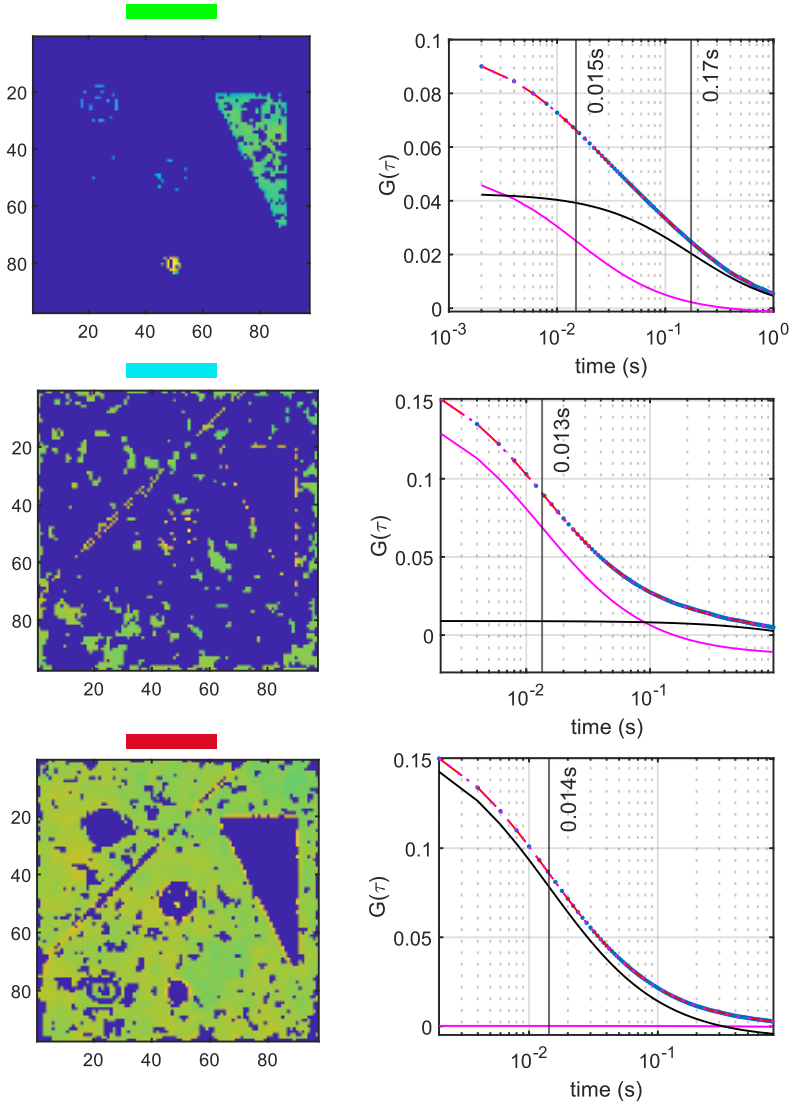

Figure 26 Local-FCS by phasor plot: On the left the maps show the pixels selected by the circles in Figure 25, respectively green, cyan and red. The selected pixels here are represented as the mean intensity value, and blue pixels are discarded. On the right side, the corresponding averaged ACFs fitted by the 2c model. In the first row, the green circle selects the autocorrelations that are, in the real space, belonging to the triangles and circle C2. This refers to an ACF correctly described by two equally populated diffusive components with the correct D values (0.9 and 0.01 $\mu m^2/s$). The points inside the *diffusive circle* in the phasor plot (Figure 25), here selected by the cyan circle, correctly represent the pixels which show a sub-diffusive modality. These occur especially at the border of the diffusional shape. To describe this modality with a 2c, a low amplitude and very slow component (black curve) is needed. The majority of the pixels are easily selected by the red circle in the phasor plot. The averaged ACF can be described clearly by a single component with 1 $\mu m^2/s$ (black curve).

3.3.2 Maximum Entropy Method: from ACF to diffusional spectra

Paragraph 2.1.13 introduces the Maximum Entropy Method. This approach has been used since the nineties to fit ACFs. An interesting approach is represented by the work of Steinbach et al. [88] that binds NLS fitting and MEM. In this paragraph, we implement the MEM in imaging FCS measurement.

The key advantages of this MEM method are:

1. It is easy to apply with no other *priori* information
2. For each ACF it will extract a spectrum of diffusive populations
3. A sub-diffusive diffusion 2D (with $\alpha < 1$) can be represented with a more dispersed spectrum with the same peak position with $\alpha = 1$. This is not the case for a super-diffusive case.

Following the eq. (78), if we have used a parallel FCS measurement, MEM will export multiple spectra $\boldsymbol{\alpha}_i(\boldsymbol{x}, \boldsymbol{y}, \boldsymbol{\tau})$. These spectra can be analysed in different ways. The easiest is to merge up all spectra $\sum_{x,y} \boldsymbol{\alpha}_i(\boldsymbol{x}, \boldsymbol{y}, \boldsymbol{\tau})$. Since the spectra are normalized, for having representative spectra proportional to the number of the molecules, they could be weighted with the reciprocal of $G(\tau = 0)_{x,y}$. One problem with this approach is that positions with very low $G(\tau = 0)_{x,y}$ could be places where a large number of molecules or no molecules are present. In this latter case, the inverse of the G(0) would lead to a very large value, ruining the weighted averaged spectra. Another way of weighting is performing a N&B analysis [117],[113], [118], [119] and using the extracted *N*. An even simpler method is to suppose the Brightness constant over the space and weigh the spectrum with the average number of photons collected for each pixel. If we sum up all the spectra weighted, we will have a global diffusion spectrum of the molecules. The spectra peaks should be similar to the ones found with tICS, without the need to choose the theoretical model. This could be a better model selection than the F-test (Chapter 2.1.12). Another way to analyse the spectra is in an orthogonal view: the spectra can be binned temporally in 2 or more temporal windows: $\sum_{\tau=\tau_1}^{\tau_2} \boldsymbol{\alpha}_i(\boldsymbol{x}, \boldsymbol{y}, \boldsymbol{\tau})$. The sum of these windows can be considered as the contribution of those timescale molecules to the diffusion population.

A critical aspect of this method, as highlighted in the theoretical MEM derivation, is the estimation of $\sigma^2_{noise}(\tau)$. This is not straightforward in FCS measurement. The first theoretical noise estimation was done by Koppel, considering the correlation function of fluorescence under assumptions of Gaussian statistics [32]. Another way of calculating the noise is to split the ACF into different chunks and measure how

much, for each lag-time, the ACFs are dispersed over the chunks [67]. Saffarian & Elson extended the theoretical framework and for the first time they computed also the "particle noise" that is relevant for long lag time[120]. Indeed, when the concentration is low, there are very few possibilities that the same configuration will reappear after a very long lag time. Moreover, in a biological context, we must consider that we are near the situation of $\tau_D < 100$ time of acquisition. This leads to the bias expressed in chapter 2.1.5, one of the major problems in this kind of analysis, even when the S/N is very high. A simple way of considering the noise when applying the MEM method to imFCS is by considering the standard deviation of the 4 nearest points for each lag time. Unfortunately, this method leads only to an estimation of the shot noise because the origin of "particle noise" should disappear, at least, only after 3 ω_{xy}. A new approach that relies on the use of the Principal Component Analysis will be presented in the subchapter 3.5. Using this method as an estimation of the noise-free ACF, it could be used to compute the $\sigma^2_{noise}(\tau)$ as a moving variance.

MEM on simulated data

Through MEM approach, each curve is transformed into a spectrum of diffusive populations α_i, each associated with a fixed diffusion coefficient (D_i), which populate the corresponding pixel. By summing these populations for each pixel, we obtain the graph shown at the top of Figure 27. As expected, the population with τ = 0.14s, corresponding to D = 1 $\mu m^2/s$, is by far the most dominant, in agreement with the theoretical predictions. By examining the fractions of populations with different diffusion coefficients, we can identify the regions with the correct diffusion rates Figure 27.

An interesting method to visualize the contributions of the different populations is shown in Figure 28. Here, the different parts of the spectrum are coloured in R, G, and B, with the slowest populations in red and the fastest ones in blue. This is similar to how a camera with three bandpass filters interpolates a real colour. Below the figure, the logarithmic *calibration* curves and the averaged spectrum across all pixels are shown. The yellow colour can be the result of the combined contributions of the green population with τ = 0.1 s (D = 0.1 $\mu m^2/s$) and the red population with τ = 0.014 s (D = 1 $\mu m^2/s$). In regions where only one component is present, such as in C3, or where one component dominates, such as in C2, the colour reflects the corresponding population (e.g., green). These false colours can be used to separate different spatial regions based solely on dynamic information, similar to the approach used with phasors.

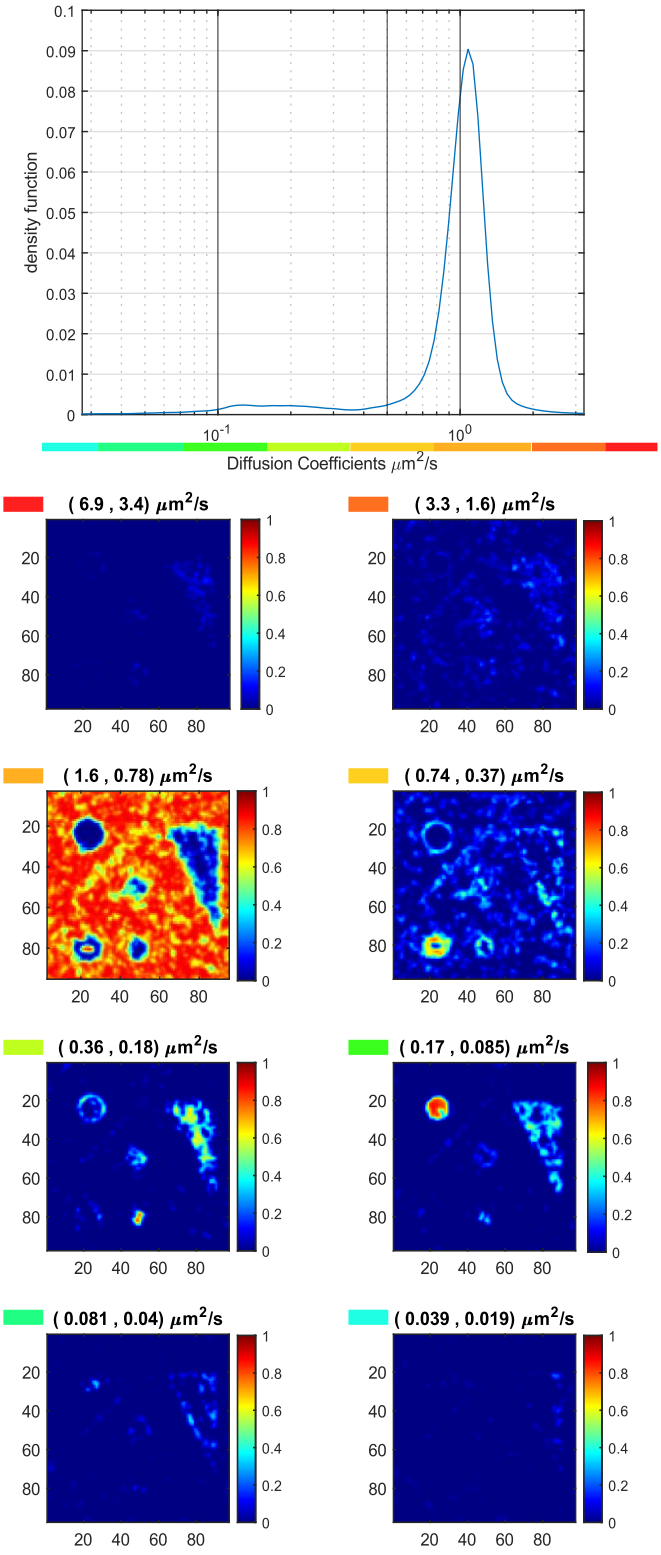
density function
Diffusion Coefficients $\mu m^2/s$
(6.9 , 3.4) $\mu m^2/s$
(3.3 , 1.6) $\mu m^2/s$
(1.6 , 0.78) $\mu m^2/s$
(0.74 , 0.37) $\mu m^2/s$
(0.36 , 0.18) $\mu m^2/s$
(0.17 , 0.085) $\mu m^2/s$
(0.081 , 0.04) $\mu m^2/s$
(0.039 , 0.019) $\mu m^2/s$

Figure 27 MEM panel for noise-free simulation. At the top, the weighted average of all spectra is presented. In this case, the weights used are the Numbers obtained through N&B method. The resulting spectrum shows two peaks. These are similar to the ones found with tICS approach and to the simulated values (black lines). It worth noting that the intermediate component (middle line) is only slightly represented in the simulation stack and appears to be missed by the averaged MEM spectra. Nonetheless, MEM allows for the extraction of the pixel's contribution at different temporal windows. For each temporal window, depicted with different colours, it is reported which position gives the major contribution. As it is clear, all the shapes containing the different diffusion coefficients are well represented (the fast component in the triangle is recognized slightly faster than simulated).

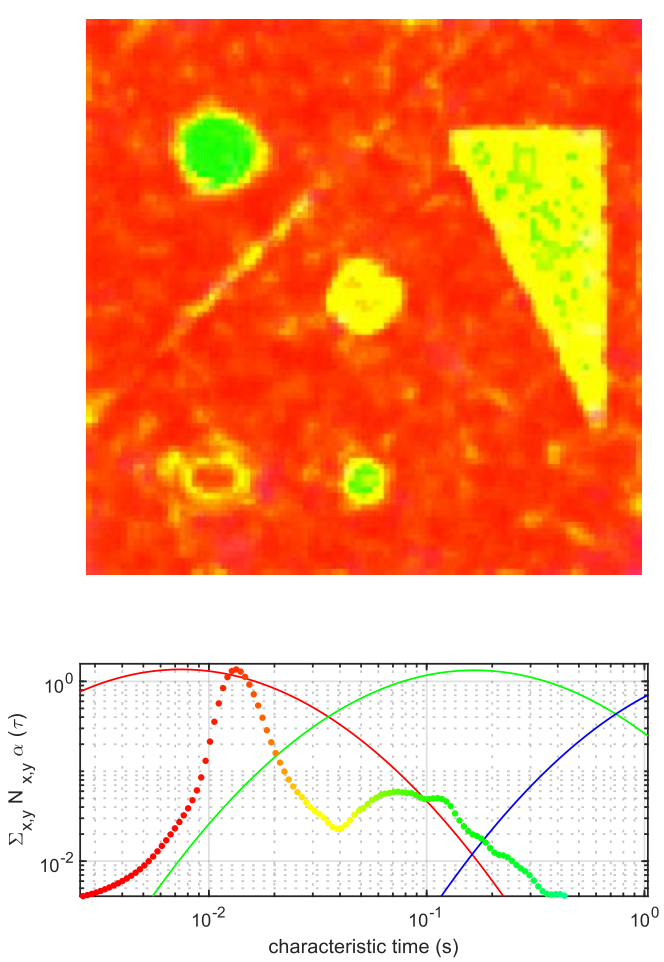

Figure 28 Hyperspectral view of MEM spectra. Different parts of the spectra are coloured in Red, Green, and Blue, with the slowest populations in blue and the fastest ones in red. In this representation, yellow pixels may indicate the presence of two equally populated components (one fast in red and one slower in green) or a single intermediate population. At the bottom, the logarithmic graph represents the weighted averaged spectra superimposed to the calibration colourimetric curve. This is an alternative map with respect to Figure 27.

These diffusion spectra can be used as multidimensional spaces on which distances can be calculated to perform clustering of regions with similar characteristics. A possible execution of this approach is shown in Figure 29. Six distinct diffusion regions were identified using a clustering algorithm applied to the diffusion spectra. By employing the concept of local-FCS, the ACFs originating from these regions can be aggregated and fitted with high precision. Remarkably, this automatic method analyses only the shape of the MEM spectra. Other information can be added, like the number of molecules present in each pixel or the mean intensity, etc. The challenge in that case would be to weigh each biophysical quantity differently. This will be one of the future explorations.

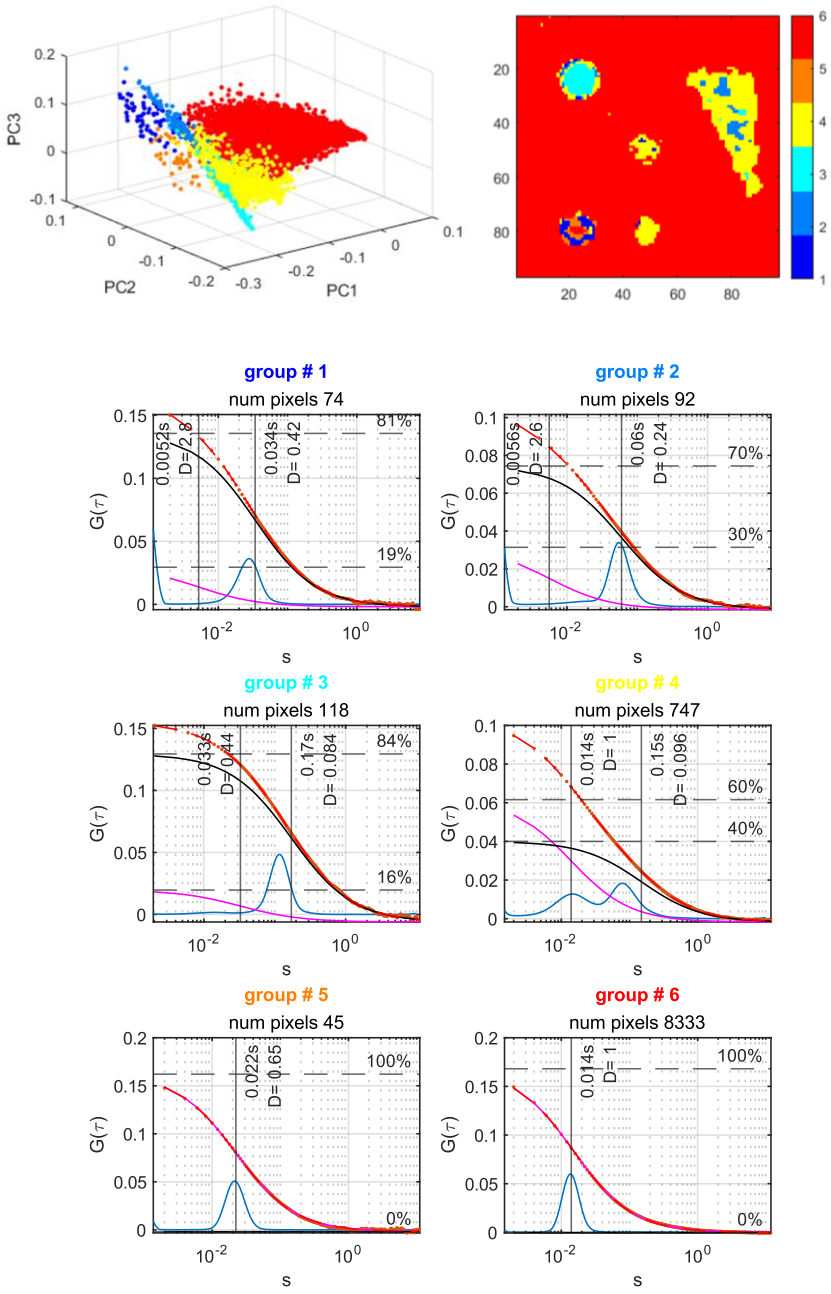

Figure 29 Automatic segmentation of diffusive regions by clusters analysis over the MEM spectra. Through a principal component analysis, the dimensionality of the spectra has been reduced to a few (10) components. Then, computing the distance of the spectra in this hyperspace with 10 dimensions, 6 classes are defined and depicted in different colours. At the bottom, the fitted curves for each class are shown. This automated approach effectively classifies all simulated diffusional regions solely based on the spectral shape.

3.3.3 High-noise simulation

To evaluate the robustness of these analysis methods, we simulated a scenario where the measurement is affected by a Gaussian noise centred in zero with a standard deviation approximately ten times the signal amplitude. As shown in Figure 30 this significantly reduces the signal-to-noise ratio (S/N) of the ACFs.

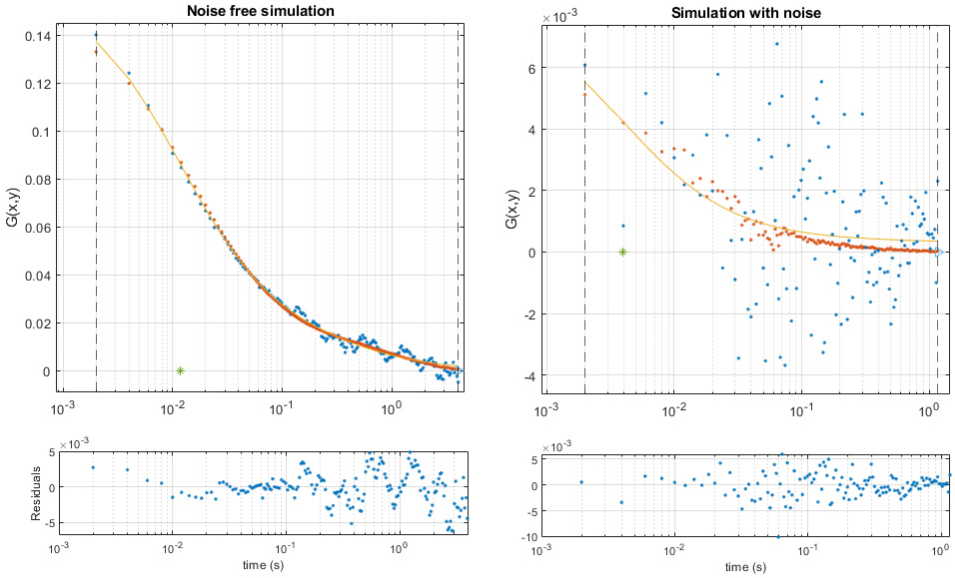

Figure 30 Single pixel autocorrelation function (blue points) of the noise-free simulation (par 3.3.1) and the high-noise simulation. The ACF filtered using PCA is shown in orange (chapter 3.5), while the yellow curve represents the fitted data using a two-component model. Due to the low S/N ratio, the second fit underestimates the characteristic diffusion time τ_D from 0.014 s to 0.002 s.

This chapter will show how the previously introduced methods perform in this low signal-to-noise context. Although the two-component tICS analysis is noisier with respect to the noise-free simulation, it still accurately reports the simulated fast diffusion coefficient.

Using the single-pixel approach, some tuning can be made to improve results. The most effective is the application of a spatial Gaussian blur to the ACFs. This helps to restore the S/N at the cost of reduced spatial resolution. To avoid losing resolution, the noise suppression algorithm presented in the final chapter based on Principal Component Analysis could be implemented (Figure 30). Since the two-component method with a fixed fast diffusion coefficient effectively describes the experiment better than the one-component model, we will focus on that. From the

tICS curves, a diffusion coefficient of 1 $\mu m^2/s$ is recovered, and this value is used as a constraint in the two-component fits.

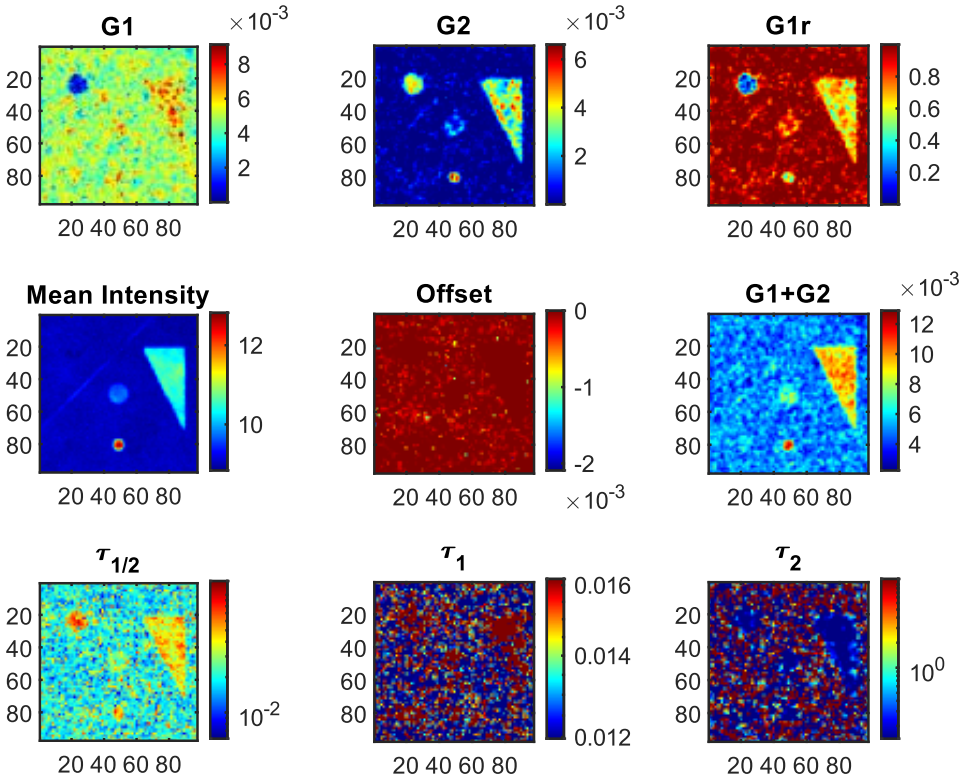

Figure 31 Maps of the fitted parameters obtained using the single-pixel FCS method applied to the high-noise simulation dataset. The dataset is described with a two Brownian component.

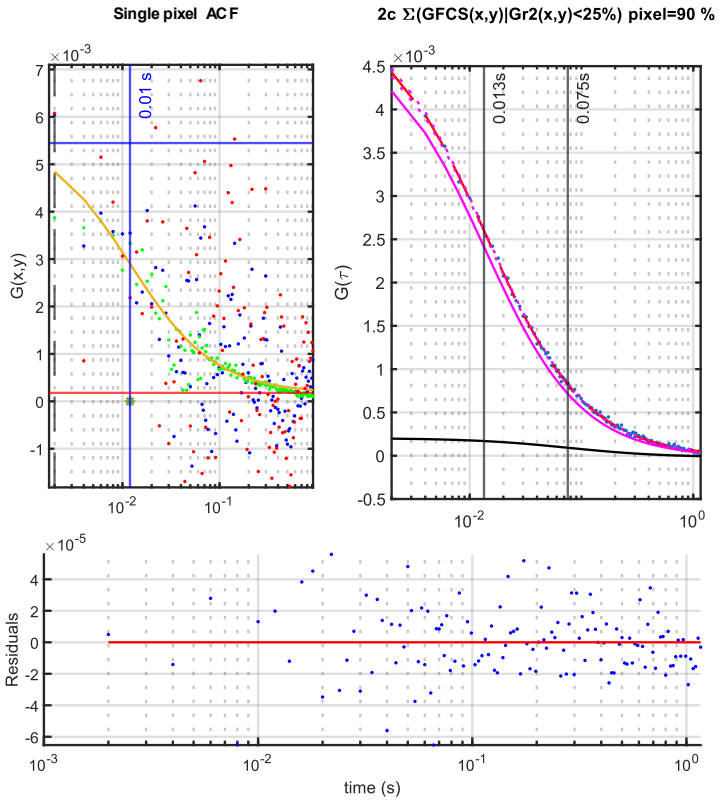

Figure 32 On the left, in red, the single-pixel ACF of the high-noise simulation. In blue the ACF is averaged over one PSF. In green the ACF is filter by PCA (chapter 3.5). All the autocorrelations are fitted with two components fixing the faster component from tICS (yellow curve). By selecting only the pixel in which the faster component is dominant (G1r>75%), we recover a very high signal-to-noise curve that could be fitted precisely and accurately (right panel). Local-FCS of the only fast diffusional pixels panel reports the correct simulated values even in this critical high-noise context (D = 1.07 ± 0.07 μm²/s). Of note 90% of the pixels are selected.

In the first panel of Figure 32, the spread of the data to be fitted is evident, highlighting the need for at least a PSF-level filter to improve the S/N (blue data points). By applying the PCA method, we obtain the green data points. The resulting fit is shown in yellow. The fitting parameters of the ACFs, filtered with the size of a PSF, are summarized in Figure 31. Although the fitted τ values are quite noisy, we still achieve a good contrast in the G1r map. Using this, it becomes possible to obtain a highly accurate fit for the faster component by excluding areas populated with mixed molecules (Figure 32). For instance, the theoretical diffusion coefficient D = 1 μm²/s is measured as D = 1.07 ± 0.07 μm²/s.

Similarly, the triangular region can be easily identified by examining the intensity (or the G0=G1+G2 value), allowing us to average all the internal autocorrelations. Despite the poor signal-to-noise ratio for fitting the ACFs at individual pixels, this approach enables us to accurately retrieve the simulated parameters ($D1_{theoretical}$ = 1, $D1_{measured}$ = 1.03 ± 0.05 μm²/s; $D2_{theoretical}$ = 0.1, $D2_{measured}$ = 0.100 ± 0.005 μm²/s, $G1r_{theoretical}$ = 0.5, $G1r_{measured}$ = 0.54 ± 0.05).

Similar to the approach used with MEM, clustering algorithms can also be employed to leverage these maps, segmenting them into different regions for further fitting.

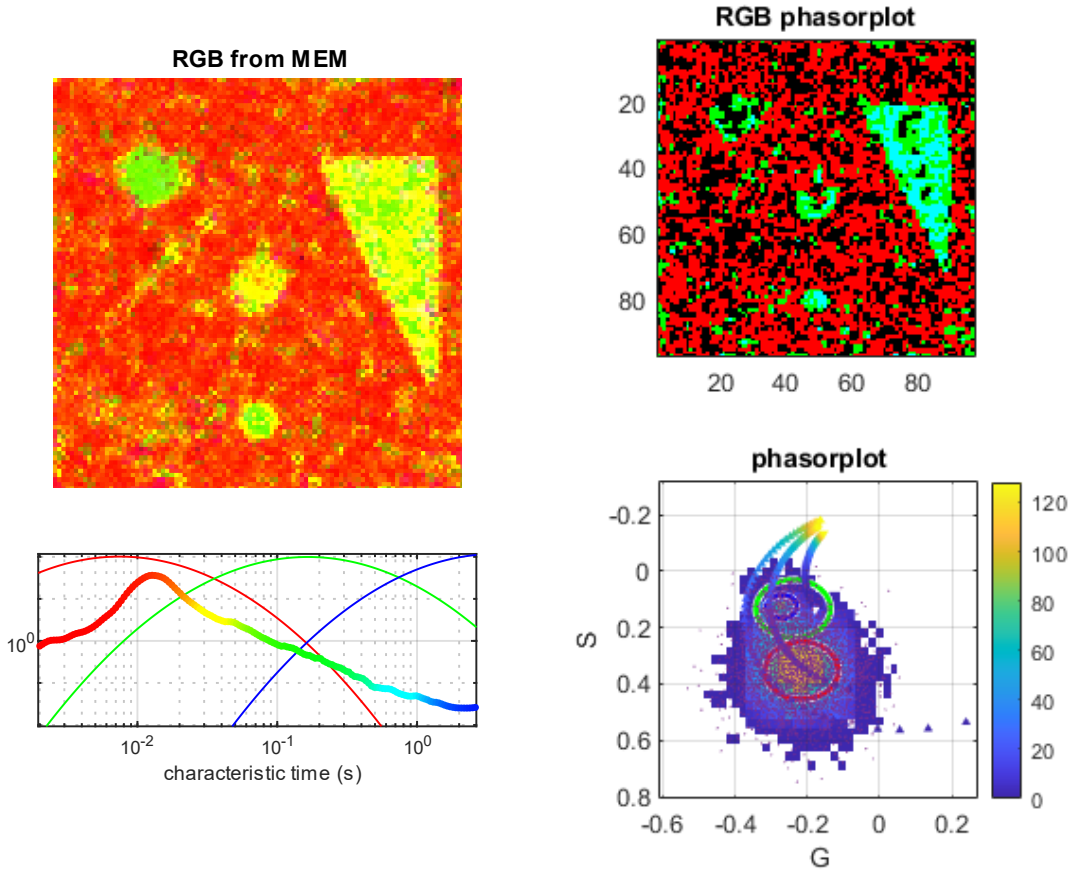

Figure 33 MEM and Phasor Maps obtained for high-noise simulation. On the left, by MEM, all the diffusive shapes are recovered. These regions can also be clearly identified in the phasor space. In the "RGB phasorplot", the pixels are coloured by the hue of the belonging circle.

Even through phasor and MEM analysis, the diffusion coefficients and relative populations for C3 and the Triangle can be obtained using the local approach. The L structure becomes slightly visible through MEM analysis.

In summary: even when the autocorrelation curves present a signal that is too weak to reliably infer a diffusion model/coefficients, they can still be used to generate maps. These maps can then be employed to identify regions with similar dynamic behaviours. Combining the autocorrelations from spatial points within these *similar* diffusion regions makes extracting precise and accurate dynamic information possible.

3.3.4 Increasing the precision and accuracy in studying ACE2+EGFP

The simulations have demonstrated the effectiveness of local-FCS even in low signal-to-noise ratio contexts. By applying this approach, we significantly improved the precision and accuracy of our measurements compared to the conventional tICS method, particularly when studying ACE2 dynamics on the cell membrane. In this study, we focused on ACE2 tagged with EGFP in VERO-E6 cells. ACE2 is a membrane-bound protein that plays a critical role in various biological processes and is especially important as it is the receptor for SARS-CoV-2, interacting with the receptor-binding domain (RBD) of the viral spike protein. Using TIRF microscopy, with high temporal resolution (18 ms per frame over 1000 to 2000 frames), we were able to capture real-time diffusion of ACE2 on the cell membrane. By observing the temporal evolution of fluorescence intensity and applying a moving median to improve the signal-to-noise ratio, distinct luminous structures, comparable to clusters, become evident on the cell membrane. An initial iMSD analysis indicates a globally confined diffusion pattern in the sub-second scale. Furthermore, the tICS analysis reveals at least two distinct diffusive populations: 1) a faster population with a diffusion coefficient around 0.1 $\mu m^2/s$, and 2) a much slower population with a diffusion coefficient around 0.001 $\mu m^2/s$.

To better understand these dynamics' spatial distribution, we adopted a single-pixel approach. All previously developed and demonstrated methods were designed to extract dynamic information in this low signal-to-noise ratio context. In the following section, we will present the analysis of two individual measurements and demonstrate how the use of local-FCS approach improves the precision and accuracy of the results. As can be observed from the average intensity (which is more evident when looking at the moving average of the video), several bright regions are present, displaying very slow dynamics related to cellular movement (first panel of Figure 34). The tICS analysis was performed (Figure 35 A) using a two-component fit. As described in the simulations paragraph, the faster diffusion coefficient is imposed in the single-pixel two-component fit. The fitted 2c parameters are present in Figure 35. Except for the bright and slow structures, the signal from the fast component (G1) correlates well with the average intensity. The relative abundance of the first component (G1r) accurately describes areas where the cell is present (notably, the cell does not seem well-adhered in the upper right region) and where no bright, slowly varying structures are observed.

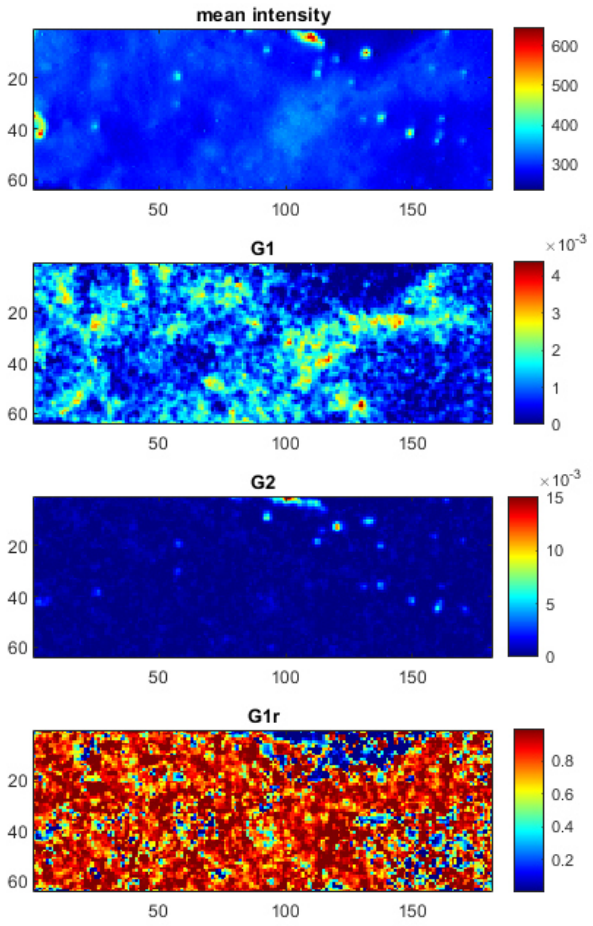

Figure 34 Mean intensity and corresponding parameters obtained from the two-component Brownian fit model of the first EGFP+ACE2 measurement. A scale of 20 pixels corresponds to 3.2 µm.

To more precisely estimate the movement of ACE2 on the membrane and subsequently assess whether biochemical treatments affect its dynamics, we selected all the autocorrelations where the fast component was dominant (G1r > 0.75). This allowed us to obtain the curve shown in Figure 35 B, taking into account 66% of the total pixels. When comparing the two curves in Figure 35, a clear reduction in the second component is observed. This reduction effectively unmixed the fast component from other dynamics. The diffusion coefficient shifted from 0.097 ± 0.05 µm2/s in the tICS analysis to 0.110 ± 0.005 µm2/s. In this measurement, the bright, stationary structures did not excessively distort the ACF; however, in other more common experiments, the difference is much more pronounced, as shown in a second measure Figure 37.

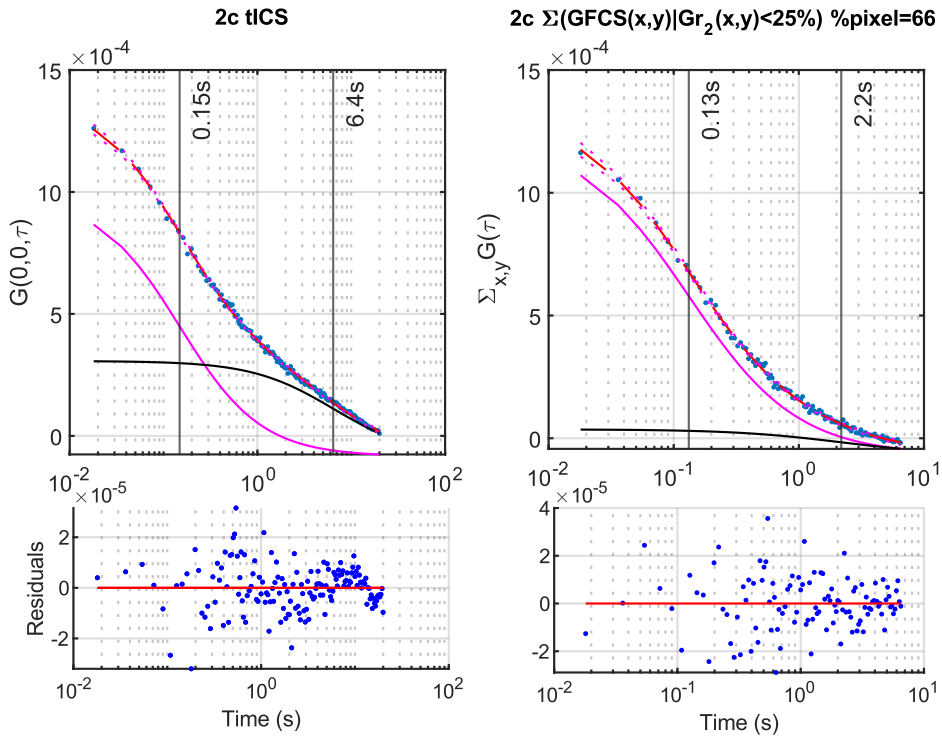

Figure 35 tICS (right) and local-FCS based on high G1r (left) data fitted with a two-component model of the first EGFP+ACE2 measurement. In these plots the magenta curve is related to the contribution of fast component to the ACF, the black to the slow component. The vertical lines indicate the characteristic times of each component. The residuals are displayed at the bottom.

This procedure of imposing the tICS value and selecting the 75% threshold can be criticized for being highly user-dependent. However, as shown in Figure 36, similar results can be achieved using MEM analysis and a clustering algorithm based on colour classification from the figure. The red pixels, equivalent to those where the fast component's contribution is dominant, return a similar diffusion coefficient. The same can be achieved through phasor analysis combined with manual selection. Nevertheless, the selection based on G1r is straightforward, effective, and computationally accessible, taking approximately one minute for 256x64 fits.

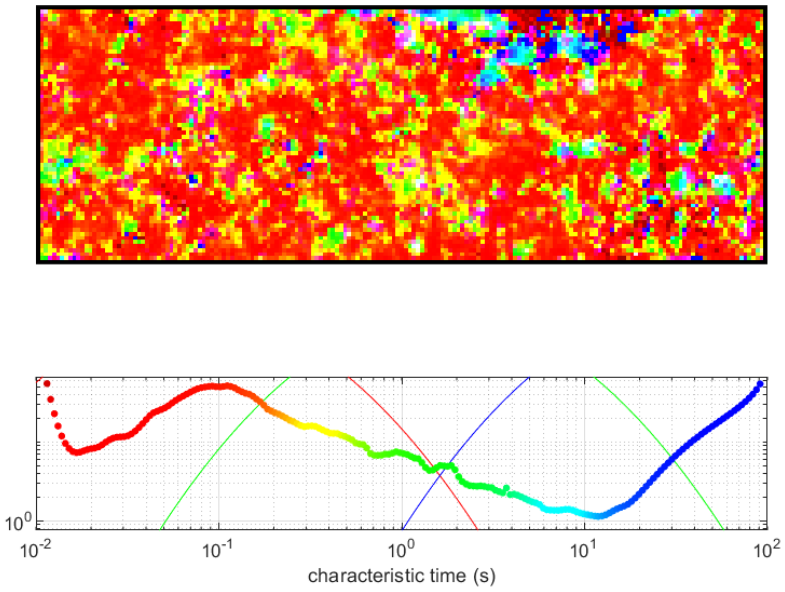

Figure 36 Hyperspectral MEM visualization on the first EGFP+ACE2 measurement. Vertical axis length 10 µm. Red indicates pixels where faster diffusive molecules are present, green corresponds to regions with slower molecules, and blue represents pixels containing very slow molecules.

In the following presented measurement (Figure 37), the number of clusters is higher, and the use of local-FCS becomes crucial for obtaining an accurate description of the dynamic at the play. In this case, the diffusion coefficient improves from 0.030 µm2/s with tICS to 0.10 µm2/s with local-FCS. Notably, we discarded 63% of the pixels during the analysis.

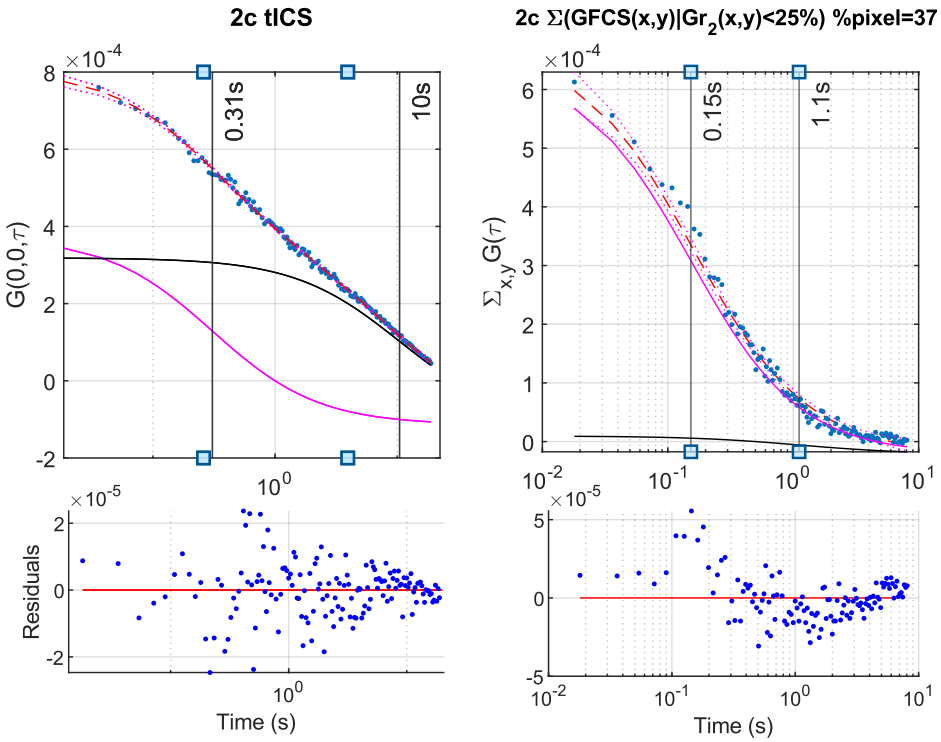

Figure 37 tICS (right) and local-FCS based on high G1r (left) data fitted with a two-component model of the second EGFP+ACE2 measurement. In these plots the magenta curve is related to the contribution of fast component to the ACF, the black to the slow component. The vertical lines indicate the characteristic times of each component. The residuals are displayed at the bottom.

We used this method to analyse a set of 20 ACE2-EGFP measurements, achieving a 50% reduction in the standard deviation and ensuring more accurate results by excluding areas with bright spots (Figure 38). The characteristic times are shifted from 0.15 ± 0.07 s (D=0.10 ± 0.05 μm²/s) with the tICS analysis to 0.108 ± 0.028 s (D=0.13 ± 0.03 μm²/s).

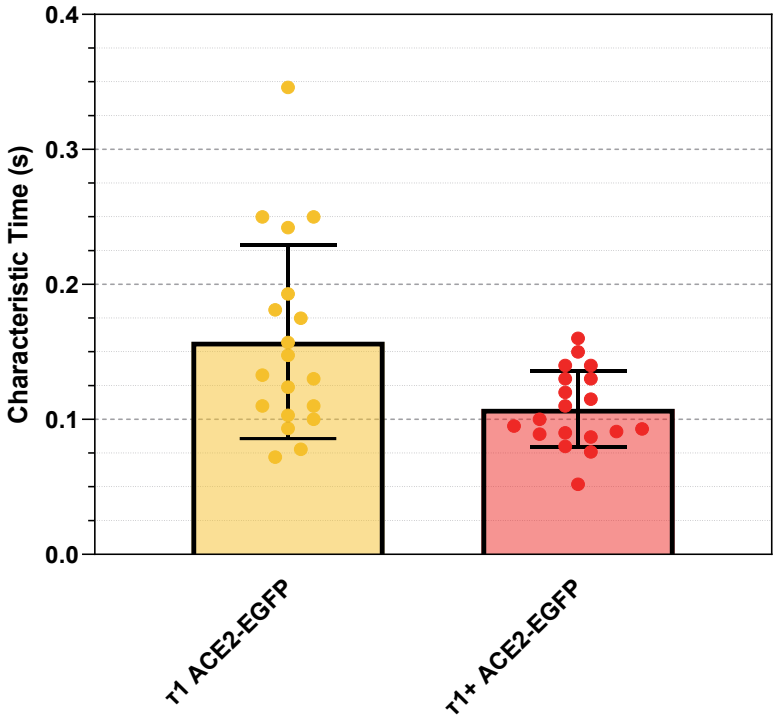

Figure 38 Characteristic time of ACE2+EGFP's fast component by tICS (yellow) and local-FCS (red) for 19 different cells.

Furthermore, we observed that the proteins moved more rapidly at 37°C compared to 25°C. This temperature-dependent increase in mobility is consistent with the general principle that molecular motion accelerates at higher temperatures due to enhanced kinetic energy. However, the lack of significant changes in response to the biochemical treatments suggests that the protein mobility may not be strongly influenced by the cytoskeleton or lipid membrane alterations under the conditions tested.

We applied several biochemical treatments (Figure 39) to assess potential changes in protein mobility. Among these, nocodazole, which disrupts microtubule polymerization; sphingomyelin depletion, which alters the lipid composition of the membrane; methyl-β-cyclodextrin, which extracts cholesterol from the membrane; were used to affect membrane organization and dynamics. Additionally, cytochalasin D, which disrupts actin filaments, was employed to explore the role of the actin cytoskeleton in protein mobility. Despite these treatments, no substantial modifications in protein mobility were observed. The only significant change in dynamics occurs when the ACE2 protein is conjugated with the RBD. The RBD is a crucial part of the spike protein of the SARS-CoV-2 virus, responsible for binding to the ACE2 receptor on the surface of host cells. This interaction allows the virus to gain entry into the cell, making ACE2 a key target in viral infection mechanisms.

When ACE2 binds to the RBD, it alters the dynamics of ACE2's mobility, likely due to changes in its spatial configuration and interactions with the surrounding membrane, as well as potential downstream effects on the cytoskeleton or membrane microdomains. To avoid the entrance of RBD inside the cell, the measurements are acquired at 25°C.

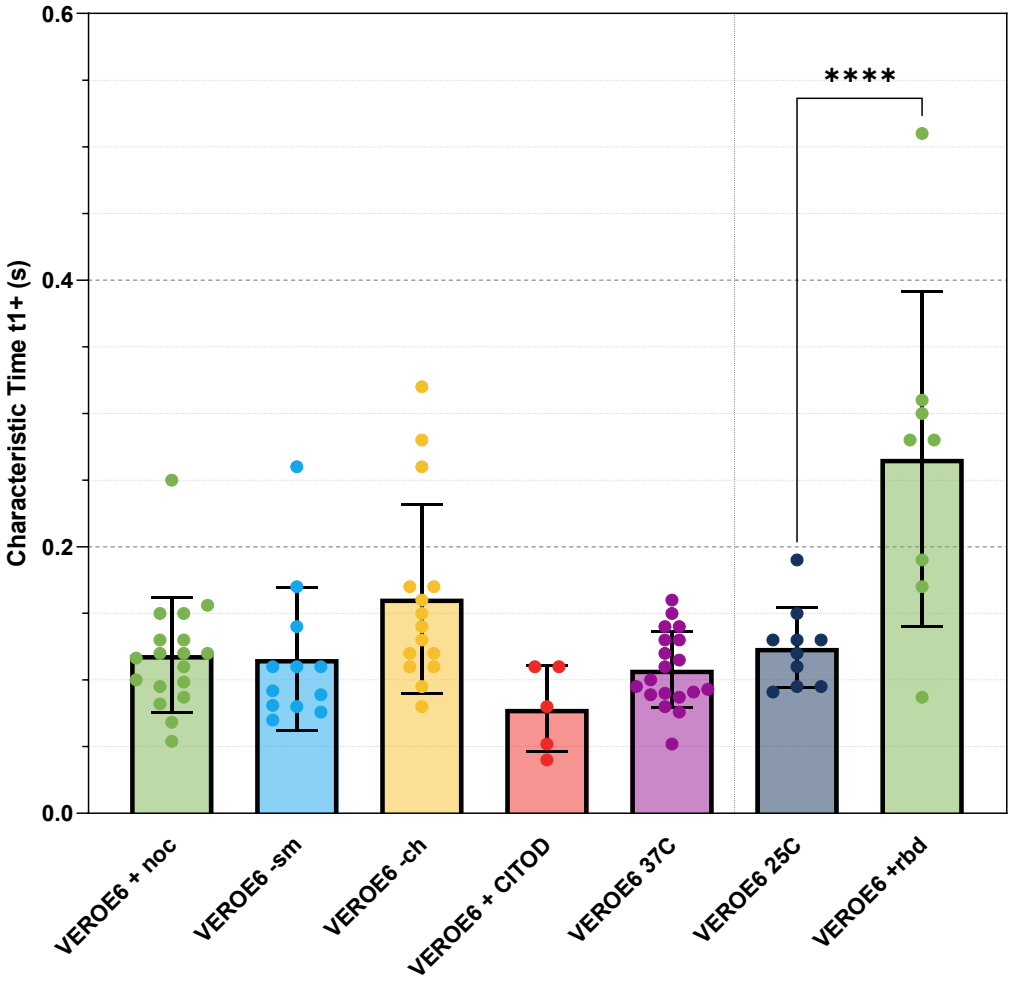

Figure 39 Characteristics time, obtained by local-FCS, of ACE+EGFP's fast component under different biochemical treatments. From left: nocodazole, sphingomyelin depletion, cholesterol depletion, cytochalasin D, Physiological condition 37C, Physiological condition 25C, addition of RBD. From the t-test the measurements with and without RBD statistically differ.

3.4 Cross-correlation Ring function

In this chapter, we propose a novel, faster and more efficient (in the case of an isotropic scenario) method to perform the pair correlation function over images. Moreover, this method will lead to quantitative maps related to the presence or the absence of barriers. From the local-FCS perspective, this could be used to have new information to discriminate pixels that present different diffusion modalities. This information can also help to discriminate how many diffusive components are present by looking at the numbers of peaks in the cross-correlation functions (CCFs).

In the classical generalization 2D-pCf of the method exposed in 2.1.6, the pair correlation function computed for the pixel (x,y) is just a cross-correlation computed with a fixed space-distance (ξ, χ):

$$\begin{aligned} \mathrm{pCF}_{x,y}((\xi,\chi),\tau) &= \mathrm{G}_{x,y}((\xi,\chi),\tau) \\ &= \frac{\langle \mathrm{F}_{x,y}(t)\mathrm{F}_{x+\xi,y+\chi}(t+\tau)\rangle}{\langle \mathrm{F}_{x,y}(t)\rangle\langle \mathrm{F}_{x+\xi,y+\chi}(t)\rangle} - 1 \end{aligned} \tag{91}$$

Remarkably ξ and χ has to be an integer. This formulation is recently used by Malacrida et al. 2018 [93], [121]

If the special case that diffusion is isotropic

$$\begin{aligned} &\mathrm{G}_{x,y}\Big(\big((x+\xi, y+\chi)\big),\tau\Big) \\ &\quad = \mathrm{G}_{x,y}\big((x-\xi, y+\chi),\tau\big) \\ &\quad = \mathrm{G}_{x,y}\big((x+\xi, y-\chi),\tau\big) \\ &\quad = \mathrm{G}_{x,y}\big((x-\xi, y-\chi),\tau\big) \end{aligned} \tag{92}$$

In this case, it could be used to merge these CCFs to increase the S/N of a CCF computed in x,y at a distance of $\rho = (\xi, \chi)$.

The approach explored is to cross-correlate the raw image with the fluorescence intensity that arises at a distance $\rho = (\xi, \chi)$. This $\mathrm{F}_{x+\xi,y+\chi}(t)$ could be computed as a spatial average over a ring with radius ρ and with $w < \omega_{xy}/2$

An analytical formula for this ring can be derived as a convolution ($\otimes$) of a Dirac Circle $\mathrm{D}(r)$ with $\rho = r - r_0$ with a Gaussian beam Ga(x,y)

$$D(r-r_0)=\frac{1}{2\pi r_0}\delta(r-r_0) \tag{93}$$

$$\mathrm{Ga(x,y)}=\frac{2}{\pi \mathrm{w}^2}\mathrm{e}^{-2(\mathrm{x}^2+\mathrm{y}^2)/\mathrm{w}^2} \tag{94}$$

Writing the Gaussian beam in polar coordinates

$$\mathrm{Ga(r)}=\frac{2}{\pi \mathrm{w}^2}\mathrm{e}^{-2(\mathrm{r}^2)/\mathrm{w}^2} \tag{95}$$

The convolution over the radius r and the angle θ can be written as:

$$Ga(r)\otimes \mathrm{D(r\text{-}r_0)}=r_0\int_0^{2\pi} Ga\left(\sqrt{r^2+r_0^2-2rr_0\cos\theta}\right)d\theta$$

$$\begin{aligned}\frac{Ga(r)\otimes\delta(r-r_0)}{2\pi r_0}&=\frac{r_0}{2\pi r_0}\int_0^{2\pi} Ga\left(\sqrt{r^2+r_0^2-2rr_0\cos\theta}\right)d\theta\\&=\frac{r_0}{2\pi r_0}\int_0^{2\pi}\frac{2}{\pi \mathrm{w}^2}exp\left(-\frac{2}{\mathrm{w}^2}(r^2+r_0^2-2rr_0\cos\theta)\right)d\theta\\&=\frac{r_0}{\pi^2 w^2 r_0}e^{-\frac{2}{w^2}(r^2+r_0^2)}\int_0^{2\pi} exp\left(\frac{4rr_0\cos\theta}{\mathrm{w}^2}\right)d\theta\\&=\frac{r_0}{\pi^2 w^2 r_0}e^{-\frac{2}{w^2}(r^2+r_0^2)}2\pi B\left(\frac{4rr_0}{w^2}\right)\end{aligned}$$

$$Ga(r)\otimes \mathrm{D(r\text{-}r_0)}=\frac{2}{\pi w^2}e^{-\frac{2}{w^2}(r^2+r_0^2)}B\left(\frac{4rr_0}{w^2}\right) \tag{96}$$

Where $B(z)$ is the zeroth order, modified Bessel function of the first kind.

$$\mathrm{K(r_0,w,x,y)=Ga\otimes D}=\frac{2}{\pi \mathrm{w}^2}\mathrm{e}^{-2(\mathrm{x}^2+\mathrm{y}^2+\mathrm{r}_0^2)/\mathrm{w}^2}\mathrm{B}\left(\frac{4\mathrm{r}_0\sqrt{\mathrm{x}^2+\mathrm{y}^2}}{\mathrm{w}^2}\right) \tag{97}$$

$K(r_0, w,x,y)$ is the new normalized filter that depends on the size of the radius of the Dirac disk $r_0 = (\xi, \chi)$. Fixing the radius ρ we can now write the cross-correlation as:

$$G_{x,y}(r_0, w, \tau) = \frac{\langle F_{x,y}(t)\widetilde{F_{x,y}}(r_0, t+\tau)\rangle}{\langle F_{x,y}(t)\rangle\langle\widetilde{F_{x,y}}(r_0, t)\rangle} - 1 \qquad (98)$$

Where $\widetilde{F_{x,y}} = F_{x,y} \otimes K(r_0, w,x,y)$

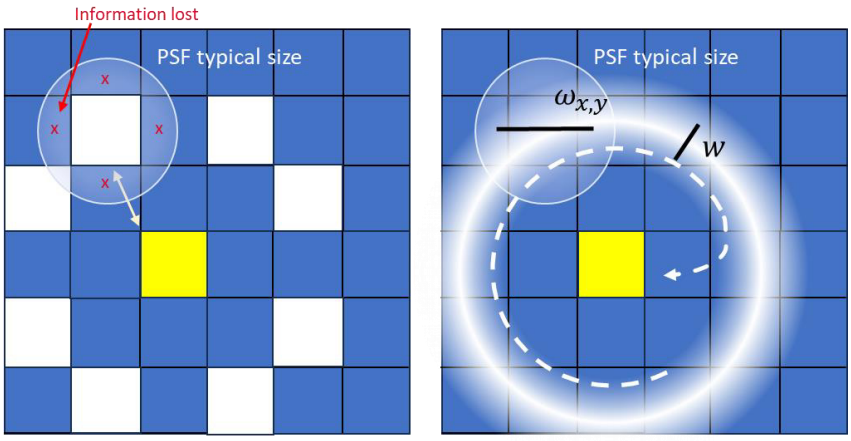

Figure 40 On the left, the classical 2D Pair correlation procedure with the CCF computed for the yellow pixel and the white pixels at a discrete distance ρ. The size of the PSF of the microscope is represented by thin circle. Using this method, if the PSF is larger than a single pixel, some fluctuations are not used in the computation of the CCF, which does not consider all the accessible information. In a Brownian context, to increase S/N, all the CCFs computed between the yellow pixel and the white pixels can be averaged. On the right is presented the new approach, which consists of convolving the image of fluctuation with the ring having a width w and a radius of ρ. Then the new CCF is obtained by cross-correlating the raw intensity fluctuations with the filtered one.

This approach, with respect to the classical one, could be helpful in several contexts:

1. Resolve the problem of having a limited and discrete distance to compute the pair correlations. For example, in the classical method, if we want to compute the cross-correlation at a distance of 3 pixels we can average only 4 CCFs. At a distance of $\sqrt{3}$ pixels we can average 8 CCFs. We can choose a distance from a continuum space with the new ring method. Averaging more points will increase the S/N of the correlation curve.

2. In ICS measurement, typically, the images are oversampled. Tuning w it is possible to not lose any fluctuations in the spatial grid. Again, this increases the S/N of the CCFs.

3. Reduced computational cost and the complexity of the analysis focusing only on the parameter r_0.

For a theoretical derivation of the $\mathrm{G_{x,y}}(r_0, \tau)$ it should be started from eq. (29) imposing:

$$\Omega(\mathbf{r}') = \Omega\widetilde{(\mathrm{r}', \mathrm{z})} = \exp\left(-2\frac{(r'-r_0)^2}{(\omega_{xy}^2 + w^2)}\right) \cdot \exp\left(-2\frac{\mathrm{z}^2}{\omega_{\mathrm{z}}^2}\right) \tag{99}$$

We can simplify by introducing w_{eff} as the average between the measurement PSF (ω_{xy}^2) and the convoluted one with the ring by defining $w_{eff}^2 = 1/2(\omega_{xy}^2 + (\omega_{xy}^2 + w^2))$ and writing the cross-correlation as:

$$\mathrm{G_{x,y}}(r_0, \tau) = \mathrm{G_0}\left(1 + \frac{4\mathrm{D}\tau}{w_{eff}^2}\right)^{-1} \cdot \exp\left(-\frac{r_0^2}{4D\tau + w_{eff}^2}\right) \tag{100}$$

In Figure 41, the advantage of this method becomes clear. Here, the light and the dark blue curves represent the classical method. In particular, the light blue curve represents the cross-correlation computed at a single pixel level in the simulation (noise-free) presented in chapter 3.3.1. It is not possible to recover any precise information from this noisy CCF. If we average around 300 CCFs, it appears clear that only one component is present, represented by a single peak. The peak is perfectly described by eq. (58) and represented by the blue vertical line. The Ring correlation functions, represented by the orange (the single pixel CCF) and red (the average over 300 CCFs) curves, have a higher S/N because they use information that arises from more than 4 points. In this case, the single-pixel curve can also be used to fit diffusional parameters. Using the eq. (58), with the substitution of w_{eff}^2 over $\omega_{x,y}$, it can be recovered the diffusional coefficient associated with the peaks. In the figure the simulated maxima is represented by the red vertical line, and it is perfectly matched by the CCFs maximum.

This analysis is advantageous for identifying how many diffusive pools are present for each point in the space because it links such an amount to the number of

peaks in the CCF. Of course, this is limited at the border of the image because of critical padding when performing the convolution.

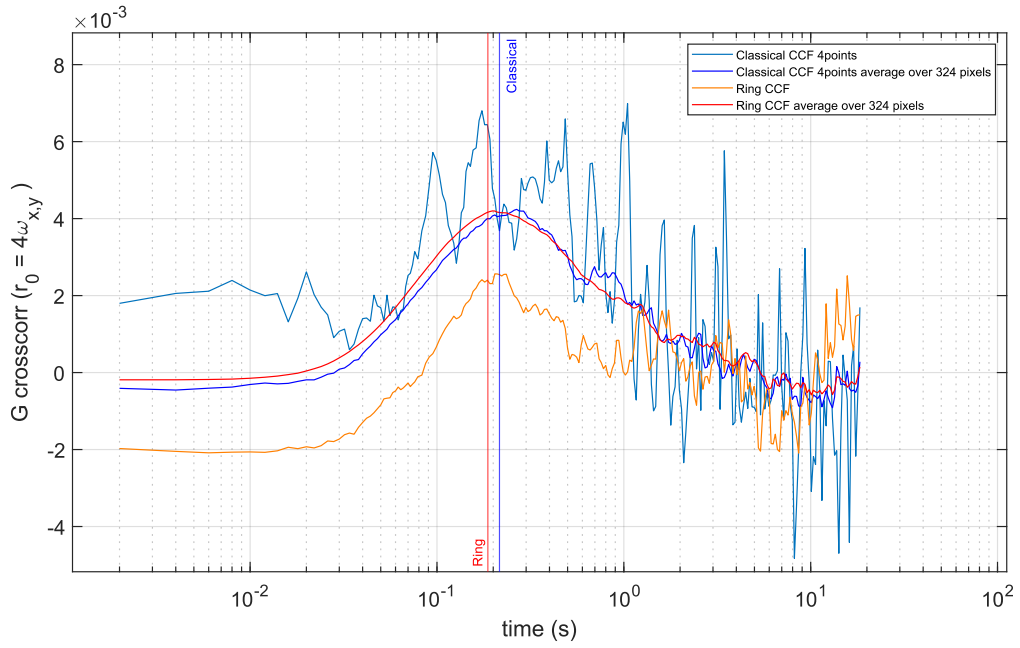

Figure 41 Comparison of the classical cross-correlation method (blue and light blue curves) and the cross-correlation curve computed with the new ring method, at a distance of 4 $\omega_{x,y}$ (red and orange curves). In light blue the CCF is computed by the classical method in a single pixel. In dark blue the CCF is averaged over 324 pixels. In orange the CCF is computed by the new ring method in one pixel. In red, the CCF is computed over the same pixels as for the blue curve. The width of the ring is $w = \omega_{x,y}$. The blue and red vertical lines represent the maximum expected from eq. (58) for the classical and the ring methods, respectively.

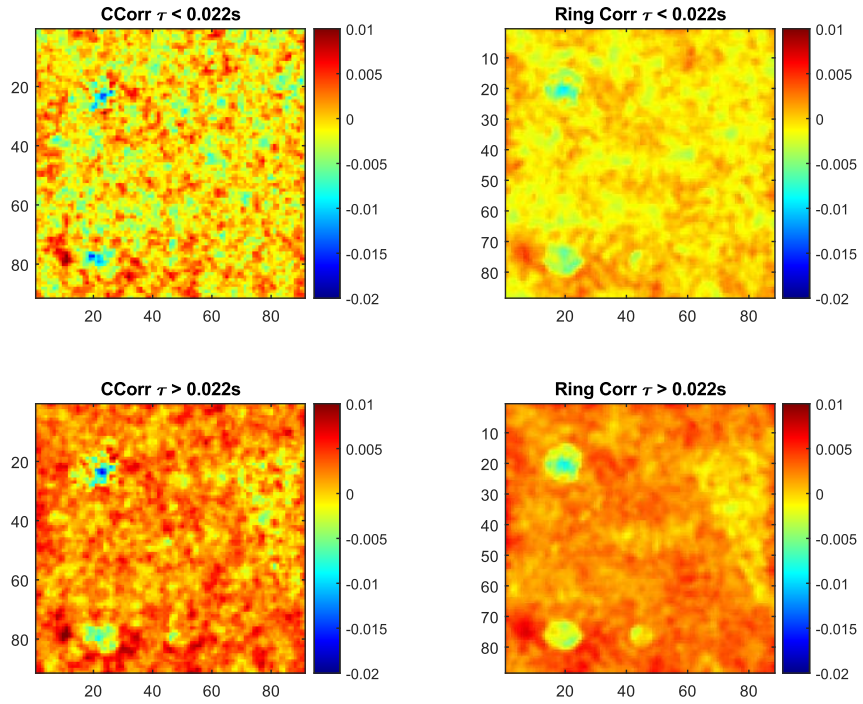

Figure 42 Mean temporal cross-correlation of the noise-free simulation (chapter 3.3.1) computed at a distance of 4 $\omega_{x,y}$ for classical cross-correlation on the left and ring cross-correlation on the right. In the first row, the maps of the CCF average for lag-times $\tau < 0.022s$, while in the second row the CCF average for $\tau > 0.022s$. Remarkably the signal-to-noise ratio of the ring method is higher, enabling to define different diffusive regions. The ellipse, at the bottom left, almost invisible to the sole autocorrelations and intensity, is recognized clearly.

The most critical limitation of this method, with respect to the classical single pixel cross-correlation, is when a strong pattern is present in the stack that is not completely corrected (i.e., dark and read noise of the camera). If the fluctuations are of the same order of magnitude as the pixels' offset variance, they become averaged out. Another assumption made is that all the samples are probed at the same time. If the acquisition speed is comparable to the diffusional time, this would lead to a more complex autocorrelation function, and the idea of the circular disk would have the wrong geometry. An interesting aspect of this method is creating maps to identify different diffusion behaviours, such as confined motion, where cross-correlation amplitude became neglectable as displayed in Figure 42. Alternatively, it could be used to add information to the model selection since the CCF holds a peak for each number of diffusion pools. In the context of MEM, a transformation in the time of cross-correlation could be used as the starting

spectrum for each pixel. The transformation retakes advantage of the eq. (58): if we have a maximum at τ_M it will be highly probable that in the MEM spectrum, there will be a peak around

$$D = \frac{r_0^2 - w_{eff}^2}{4\tau_M} \rightarrow \tau_D = \frac{\tau_M w_{eff}^2}{r_0^2 - w_{eff}^2} \tag{101}$$

The same approach could be applied on the prior distribution of the τ_{Di} of the SESAME approach (chapter 2.1.12).

Moreover, it is possible to couple MEM with a global fitting of the ACF and the CCF. The weight for the auto and the cross-correlation must be decided. It has been used with a profit ratio of 50:50.

For analysing the anisotropy could be proposed, instead of the Dirac Disk $K(r_0,x,y)$, different geometrical shapes. In particular, it could be coupled with other techniques like stICS.

3.5 ACF shapes and PCA filtering

The ACF curve computed for each pixel has a strong "structure", i.e., it is a monotonic decent curve and can be described as a sum of functions plus a noise. Furthermore, when dealing with high parallelized acquisition, we have multiple ACFs which share this *similar* structure. This is the *a priori* information we want to use to filter the data without making any fit.

The core idea is to use the Principal Component Analysis (PCA) to decompose the data on an orthonormal basis and reconstruct the signal truncating the component related to the noise. PCA is a powerful method for dimensionality reduction and noise filtering. PCA operates by identifying the underlying patterns in the data in terms of orthonormal vectors on which the spread of data is maximized. These orthonormal bases can be computed as eigenfunctions of the covariance data matrix. When applied to autocorrelation matrices typical of imFCS (x,y,τ), PCA decomposes the data into principal components, where each component is represented by an eigenfunction and its associated eigenvalue that represents the variance of the data in that direction. In mathematical terms, PCA seeks to transform the data into a new coordinate system where the axes are the eigenfunctions of the covariance matrix of the data. The covariance matrix captures how different variables in the dataset co-vary with each other. The eigenvectors of the covariance matrix point in the directions where the data has the most variance. These are the principal directions that PCA identifies. This relies on the fact that the data can be represented by a linear combination of orthogonal basis functions that describe the underlying dynamics.

Given a matrix $G(x, y, \tau)$, where G represents the autocorrelation function at each spatial position (x, y) over time τ, the data can be reshaped in a matrix having dimension i, that represent the coordinates (x,y), and τ. The covariance matrix C is calculated from this data, and PCA involves solving the following eigenvalue problem:

$$C v_j = \lambda_j v_j \tag{102}$$

Where:
C is the covariance matrix, v_j are the eigenfunctions (or principal components), λ_j are the eigenvalues corresponding to the eigenfunctions.

The eigenfunctions v_j represent the principal modes of variation in the data. Eigenvalues λ_j indicate the amount of variance captured by each principal component. Large *eigenvalues* correspond to components that capture the significant

dynamics of the system, while smaller eigenvalues typically correspond to noise or less important variations in the data.

The process of noise filtering in this context involves keeping only the principal components associated with large eigenvalues, which correspond to the dominant dynamic modes of the autocorrelation functions, while discarding components with small eigenvalues, which are likely to represent noise.

This is done in a sequence of steps:

1. Computation of the eigenvalues and eigenfunction of the covariance matrix of a dataset
2. The data matrix $G_i(\tau)$ is projected onto the eigenfunctions ν_j, described as a function of a set of principal components.
3. Eigenvalues are examined, and a threshold is applied to determine which components to keep. Typically, components with smaller eigenvalues are discarded as they contribute minimally to the overall variance and are presumed to represent noise.
4. The filtered data are reconstructed using only the principal components associated with the largest eigenvalues. This reconstruction ensures that the filtered data retains the significant autocorrelation features of the system while minimizing the impact of noise.

In the context of the autocorrelation function, we often have prior knowledge that the data should be describable as a sum of known functions (eq. (46)). The eigenfunctions computed through PCA will approximate these known functional forms, providing a compact representation of the autocorrelation data. Interestingly, these eigenfunctions can be computed on a large set of synthetic noise-free data to have a coordinate system that does not account for the noise.

The autocorrelation reconstructed $\tilde{G}(x, y, \tau)$ will be obtained by:

$$\tilde{G}_i(\tau) = \mu_{G(i,\tau)}(\tau) + \sum_{j}^{R} \theta_{i,j} \nu_j(\tau) \tag{103}$$

Where the position (x,y) at which is computed the ACF is represent by the index i, j the number of eigenvalues used, $\mu_{G(i,\tau)}(\tau)$ is the mean autocorrelation value, R is the total number of eigenvectors used for the reconstruction and $\theta_{i,j}$ are the projection coefficients of the data $G_i(\tau)$ on the base ν_j. Remarkably it is good practice to normalize the data by subtracting the mean $\mu_{G(i,\tau)}(\tau)$:

$$\theta_{i,j} = \sum_{k} v_j(\tau)(G_i(\tau) - \mu_{G(i,\tau)}(\tau)) \tag{104}$$

If the summation is over all eigenvectors, the input curve is completely described without loss of information.

For an estimation of the number of eigenvectors needed to be used, we performed different evaluations, as represented in Figure 43 and Figure 44. In these examples, we simulated 256 temporal traces with a diffusion coefficient of 1 $\mu m^2/s$. In orange one ACF and in blue the ACF filtered with different numbers of PCs. In the dashed vertical line, the fitted characteristic time has to be compared to the black simulated one. As it appears clear in all cases, the parameters inferred by the fitting on the PCA-filtered data are better than those on the raw, noisier dataset. Figure 44 shows the histograms of all the diffusion coefficients recovered from fits. The fitted parameter on PCA is always more precise and accurate, particularly with a PCs' number minor than 7.

As shown in Figure 45 this method can be used to estimate the noise present at each τ of the autocorrelation function. This method can also clean the distortion of the ACF due to the short sampling ("particle noise") without using deep learning algorithms like Wohland 2024 [112].

This approach is general and could also be used to filter cross-correlation datasets, as shown in Figure 46.

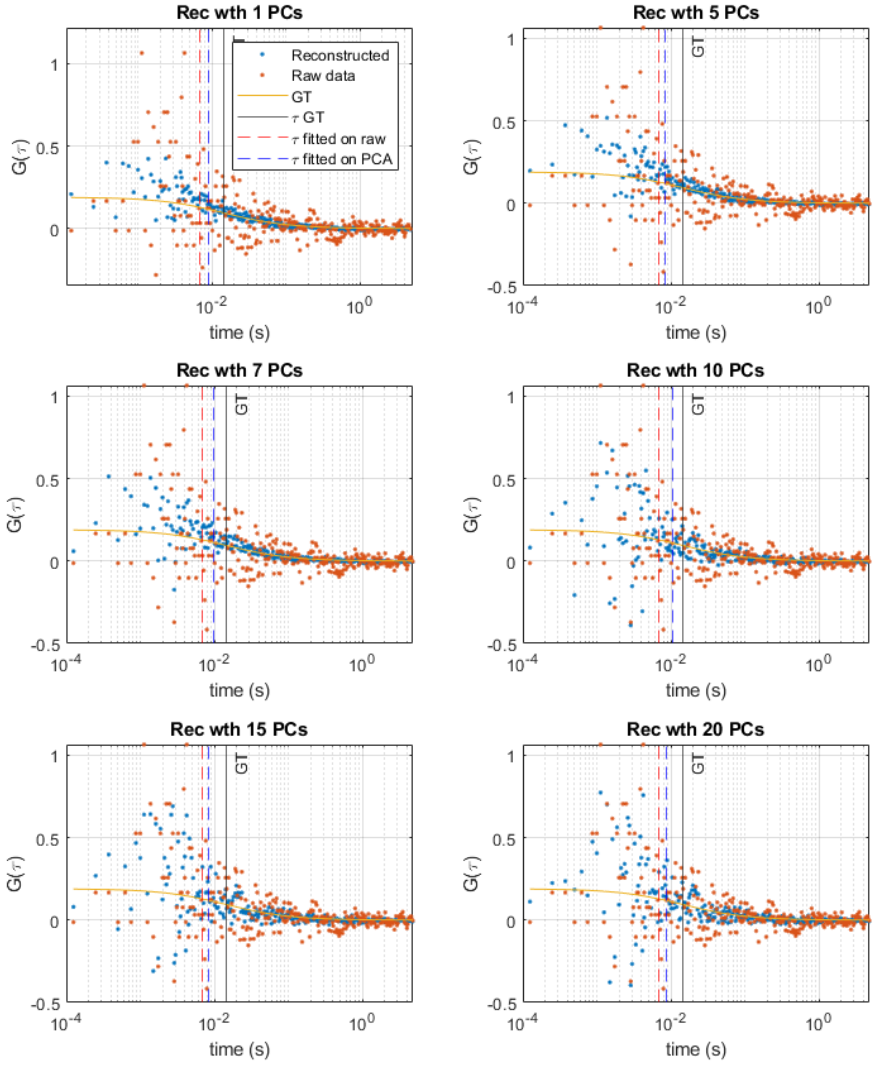

Figure 43 Different numbers of principal components (PCs) used to reconstruct the ACF. The orange point represents the raw ACF data of a single pixel in a 10 s line FCS experiment with a repetition time of 0.125 ms, dwell-time of 0.4 µs, $\omega_{x,y}$=0.24µm. The simulation consists of one population with D = 1µm^2/s with molecular brightness of 10 kcps. In blue, the reconstructed ACF with different numbers of PCs. The black vertical line represents the simulated characteristic time. The dashed red is the characteristic time fitted using the raw data, and the blue is the PCA-filtered data.

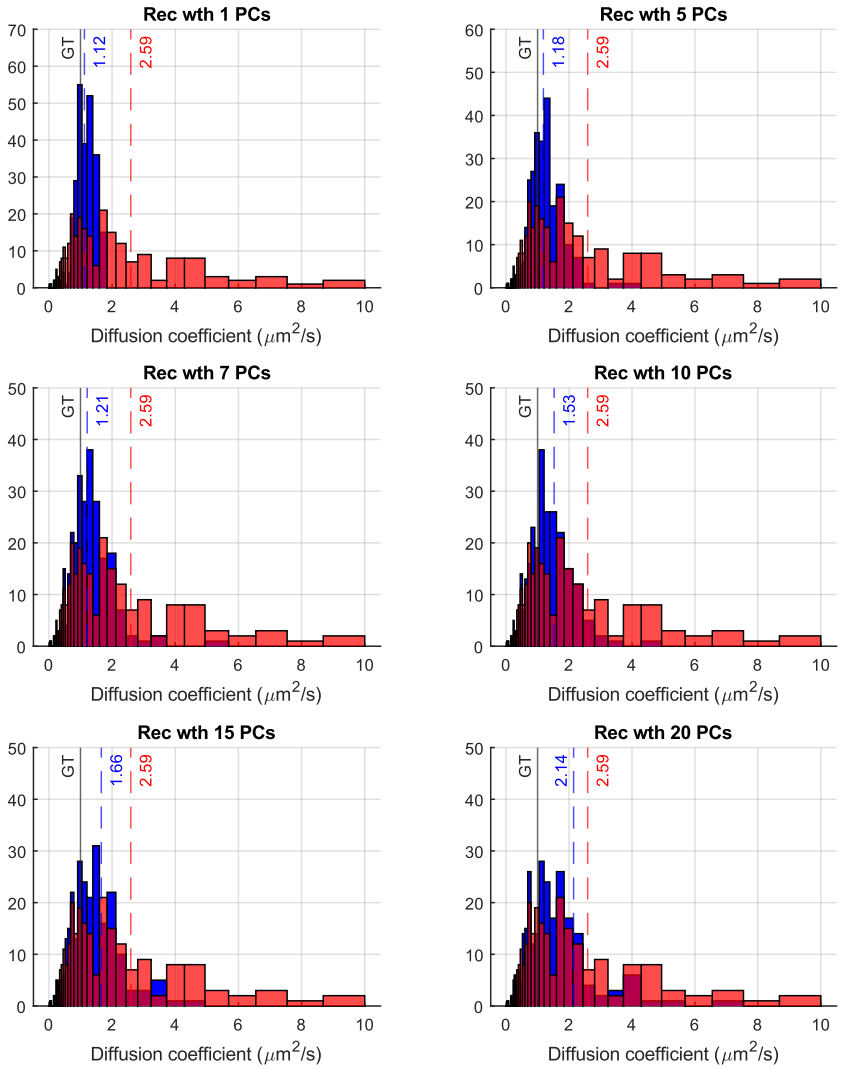

Figure 44 Histogram of the diffusion coefficient obtained with a 1 component model fit on 256 ACF -different points in a line FCS simulated experiment (same in Figure 43)- with different numbers of Principal Components (PCs) used to reconstruct the ACF. Red histograms represent the diffusion coefficient computed on raw data, and the blue on filtered data with different numbers of PCs. The simulated diffusion coefficient is 1 $\mu m^2/s$. As it appears clear, this method gives a strong advantage when dealing with a low S/N curve.

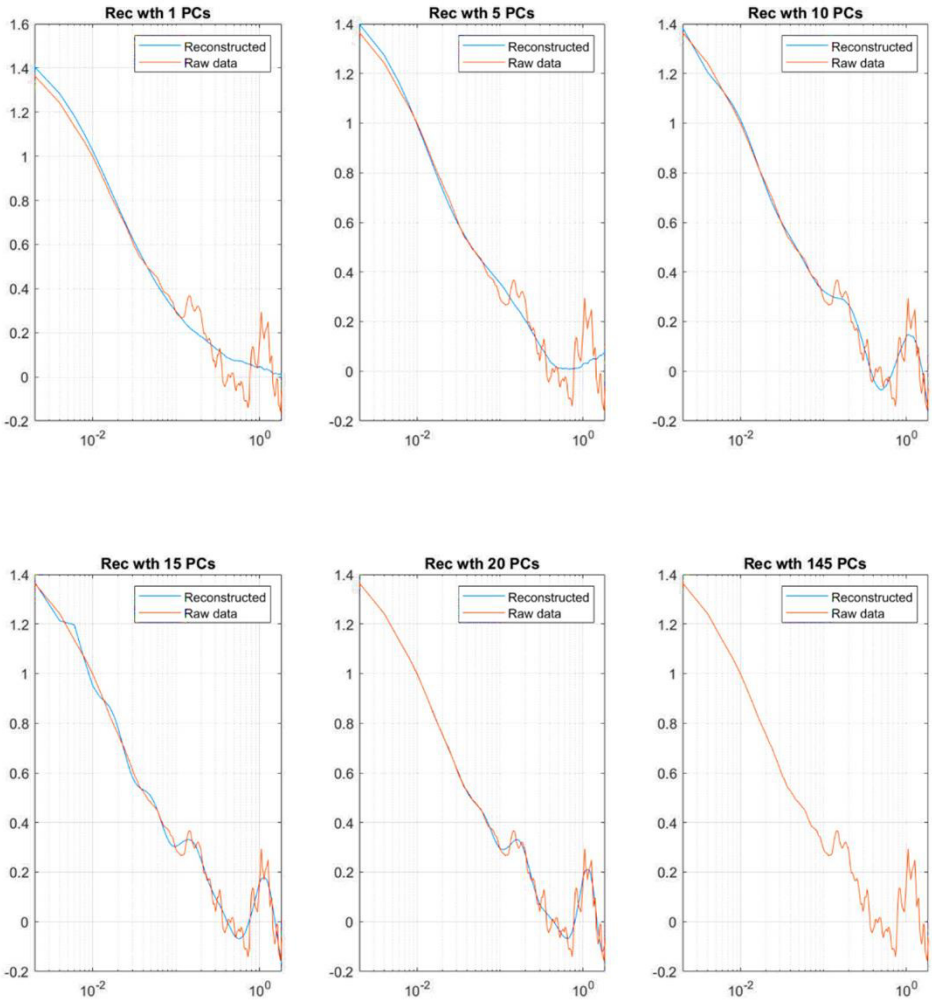

Figure 45. Different number of PCs used to reconstruct the ACF of the noise-free simulation (Chapter 3.3.1). The orange curve represents the raw ACF data of a single pixel. The noise that appears at long lag-time is known as "particle noise" (chapter 3.3.2). We can filter this noise using the information that are present in other pixels using a low number of PCs. A moving standard deviation of the difference between the raw and the filtered can give an estimation of the error $\sigma(\tau)$. This estimation can be useful to use for weighting the non-linear squared fits (and computing the χ^2), or for the MEM approach.

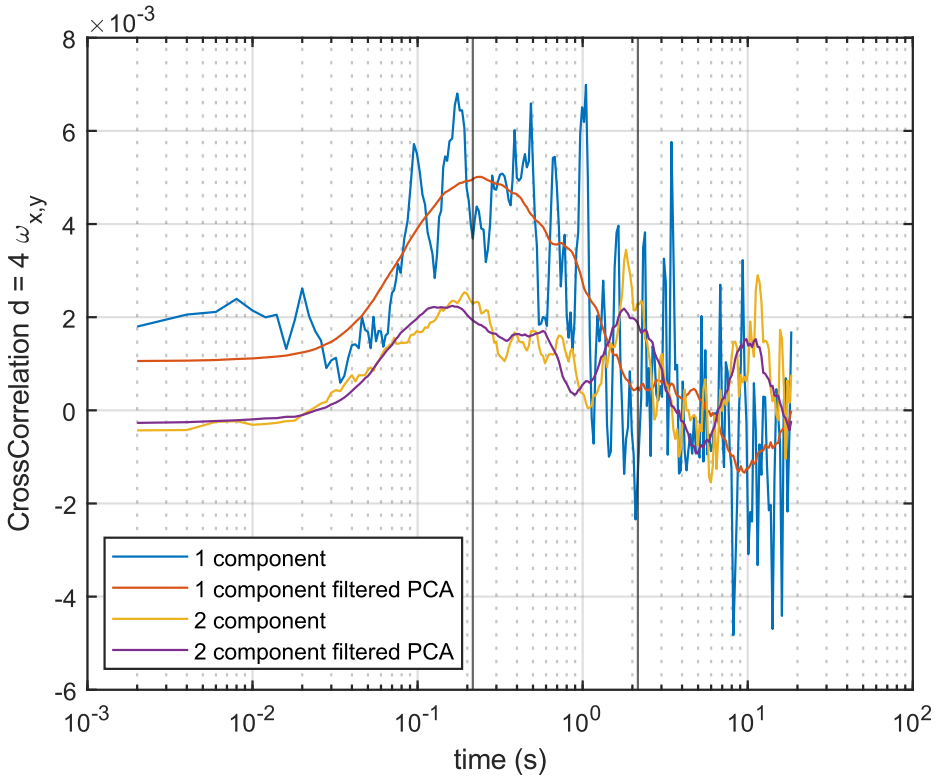

Figure 46 Cross-correlation of the noise-free simulation computed at a distance of 4 $\omega_{x,y}$ in the case of a single or double component, filtered and unfiltered by PCs. The vertical lines represent the time at which the CCFs should have the maximum by simulation. The light blue curve is a single-pixel cross-correlation; the red curve is the same but filtered with 8 PCs. The maximum is perfectly matched by the filtered experimental curve. The yellow and the purple curves represent the CCFs for a two components system, raw and filtered by PCA.

3.6 Code

All this work is written in MATLAB language. The algorithms follow the scheme in Figure 47. For simplicity, we have divided the main code into two program versions that use some shared functions. “BIOSTICS” is optimized for images resolved in time, “BIOLINE” for line-FCS. The code performs a few data-cleaning steps. First, it permits cropping of the dataset in space and time. Then, the data can be detrended using different methods introduced in 2.1.11. This cleaned and detrended dataset can be used to extract some morphological maps based on the intensity fluctuation (also in super-resolution by other plugins like SOFI [122] SRRF [123] SADC [124]) and by N&B method [119]. Besides this, the global tICS measurement can be computed to gain first insight into the diffusional aspects of the measurement. All the autocorrelations are computed by the Wierner-Kirkin theorem. The autocorrelation is fitted with 3 models: 1c 1c+α 2c. At this step the user should select if to perform 1c analysis like stICS iMSD and RICS.

The code proceeds to analyse the ACF at a single-pixel level. The ACFs can be filtered by a 2D Gaussian filter or by the PCA (Chapter 3.5). The code performs all the analyses presented in the thesis: fitting with 1c, 2c (with or without constraints on the faster component), 1c+α, Phasors, MEM, Ring Cross-Correlation. From these analyses, the corresponding parameters are saved as images. These maps could be used to aggregate pixels, using different similarity criteria, following the local-FCS concept.

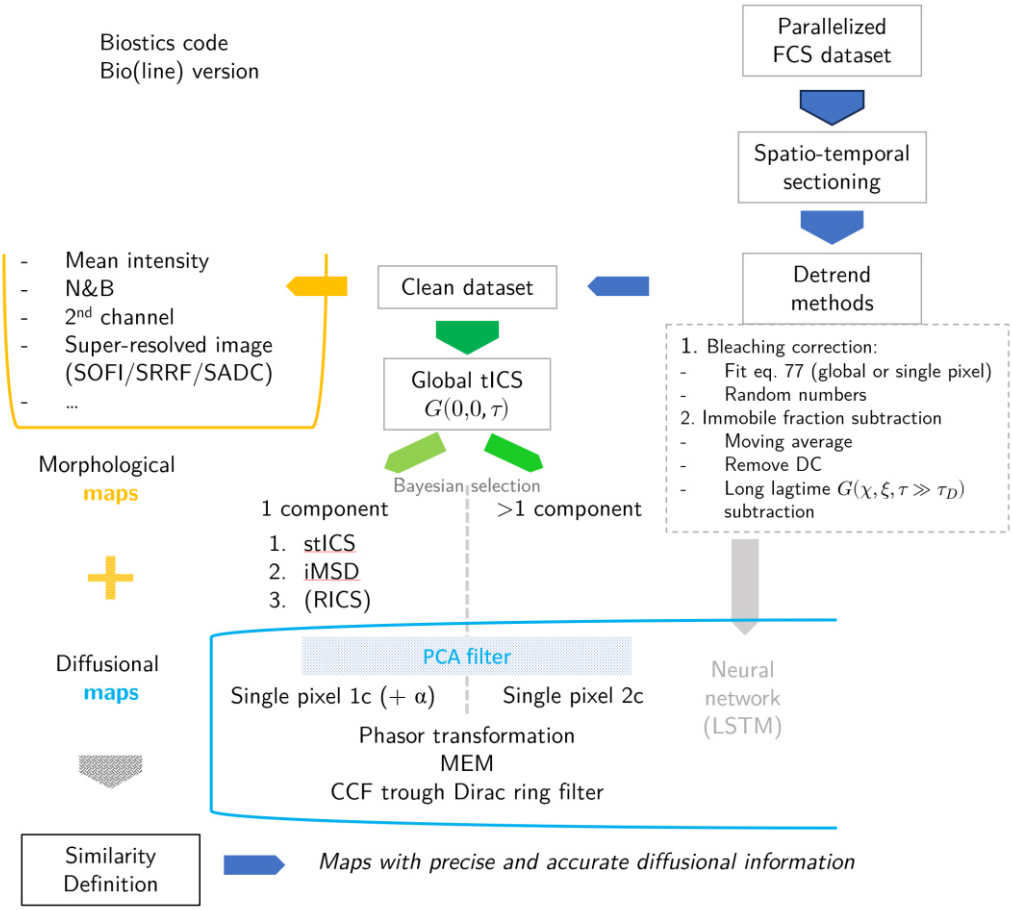

Figure 47 Scheme of the BIOSTICS program (also available optimized for line scan FCS in which is present the pair correlation analysis)

4 Conclusions

In this thesis, we have introduced a novel analysis framework called local-FCS, aimed at overcoming the limitations of conventional image correlation spectroscopy and single-pixel autocorrelation analysis. By refining these methodologies, local-FCS allows us to infer more accurate and precise information from experimental data, which is particularly useful in complex biological systems where spatial heterogeneity plays a crucial role. This approach was demonstrated across various scenarios, including model membrane studies, simulations, and live-cell measurements. In each of these contexts, the technique has shown a clear improvement in identifying and characterizing the diffusional properties of molecules compared to other state-of-the-art methods.

Local-FCS relies on the definition of *similarity* between different spatial positions (identified as pixels). Instead of analysing each pixel individually, it groups pixels based on shared features. Such a grouping allows us to average their ACFs, improving the signal-to-noise ratio of the grouped curve. This leads to a more precise diffusive parameter estimation than the single-pixel approach. Since it averages only similar single-pixel ACFs, it ensures higher accuracy than Image Correlation methods that bound proximal pixels.

The definition of *similarity* can vary depending on the biological context. In lipid bilayer studies, the fluorescence intensity was used to group pixels from different membrane phases. In the protein ACE2 dynamics study, the ratiometric map between fast and slow diffusive components was used as the similarity metric. To discard rare events like bright and slow objects passing through the focal volume, we used a similarity definition based on the shape of the ACFs. In this context, we can define local-FCS as a general platform in which image correlation spectroscopy is only a particular case where *proximity* defines *similarity*.

Throughout this thesis, simulations played a central role in validating the local-FCS method (chapter 3.3.1). We created synthetic datasets to model different diffusion behaviours, and these simulations confirmed that the proposed method consistently provided more reliable and accurate diffusion coefficients than traditional methods. We used simulations to evaluate the method's performance under critical signal-to-noise ratio conditions. As discussed in Chapter 3.3.3, local-FCS approach demonstrated robustness and proved significantly more precise results than single-pixel analysis methods. Local-FCS was integrated with different analytical methods, such as classical fitting approaches (using theoretical models discussed in Chapter 2.1), the phasor method (3.2), and the Maximum Entropy Method (3.3.2). These

tools were employed to gain descriptive information that could be used as *similarity* metrics in different ways.

In particular, in our studies on model membranes (chapter 3.1.1), we demonstrated the versatility of local-FCS in determining diffusion rates across different membrane phases. By analysing DPPE ATTO 647N labelling, we observed the separation between liquid and more ordered phases and through line-scan FCS, we successfully quantified the differences in viscosity between these regions.

In another case study, by analysing the similarity among the ACFs' shapes, we obtained a precise measurement of the diffusion of PD-L1, unmixing the diffusion from the dynamics of slower bright vesicles (chapter 3.2.2). For ACE2 analysis, we used local-FCS to isolate and quantify the fast-moving components of the membrane protein, filtering out the contribution from bright, slow-moving structures. Achieving such a level of precision and accuracy has been challenging with previous global methods like tICS, stICS or iMSD, where the *a priori* spatial averaging process can hide local dynamics.

In Chapter 3.4 we introduced an effective method to compute the cross-correlation between a pixel and its surroundings at a defined radial distance. This approach enabled us to generate cross-correlation maps alongside those derived from autocorrelation, providing additional data for model selection at each pixel (by counting the number of peaks in the cross-correlation). Moreover, these maps could facilitate the development of new *similarity* metrics allowing us to identify areas with confined diffusion, the presence of multiple populations exist, and other spatial dynamics.

The concept of *similarity* could also be used to filter the data, as explained in Chapter 3.5, using principal component analysis. This filter produces ACFs and CCFs with better S/N, enabling a more precise single-pixel diffusion description. We believe these filter procedures, presented for the first time in this thesis, will become a standard in this field.

All of this work is coded in MATLAB except for the Bayesian SESAME algorithm and the LSTM method, which are presented briefly in Chapter 3.6. This code will soon be integrated into a new, more complete, user-friendly platform.

One future direction is to expand the use of all the maps created by the cited algorithms and modalities to accurately segment concurrent dynamics.

This multimodal dynamic approach can be implemented in various ways. As a first example, Figure 29 presents a prototype: each MEM-spectrum, composed of 200 points, is reduced to 10 dimensions using PCA. A clustering algorithm

aggregates nearby points (pixels in the real space) into 6 classes by computing the distance in this ten-dimension space. This approach becomes more complex when the information derives from different biophysical quantities (e.g., diffusion coefficients, concentration, brightness, positions, amplitude of cross-correlation at different spaces/times etc.). This challenge can be addressed by data whitening to avoid overweighting certain descriptors. The analysis of high-dimensional map spaces could reveal insights that other contrast methods may not highlight. A simple example is the elliptical pattern in the simulation dataset, which is almost invisible in mean intensity and autocorrelation but becomes evident in the radial cross-correlation (Figure 42).

All these methods can be further improved by taking advantage of the additional data provided by the Image Scanning Microscope (ISM). This microscope records a micro-image at each scanned position instead of a single intensity value. Such a configuration offers multiple advantages; for instance, it allows for the adjustment of the PSF waist post-acquisition, making the Spot Variation approach easy to implement and straightforward. This approach has been used successfully at a single position, as reported in Chapter 2.1.3, but has yet to be applied in imaging FCS. We believe that this approach could enhance local-RICS, which currently suffers from an oversimplified analysis. By comparing the estimated diffusion coefficient with the waist of the reconstructed PSF, we can gain insights into diffusion behaviours, information otherwise lost with standard confocal setup.

Additionally, we are currently developing new imaging schemes (in excitation and detection) to expand possibilities for local-FCS methods in this ISM context.

Another future purpose is to generalize our new Bayesian method, introduced in Chapter 2.1.12, to anomalous diffusion and to apply it for fitting grouped ACFs. This will enable automatic model selection on a more solid theoretical base instead of using the F-test.

The new approaches based on neural networks (NN) offer clear advantages over traditional deterministic methods. We anticipate that much effort will be directed toward this area in the coming years. Our seminal work using Long Short Term Memory in FCS is still ongoing, but it shows promise for obtaining diffusion information directly from fluctuations. To assess the robustness of these new algorithms, especially in high-complexity simulations, local-FCS could help users to have greater control over the neural network results. In particular, NNs could identify *similar* pixels from fluctuation (or derived maps), and then fit the data deterministically.

Local-FCS described in this thesis can be applied in a wide range of microscope setups. It aids in recognising artefacts and assessing precise and accurate diffusional

descriptions of samples. Furthermore, it offers a broad set of maps that can be used to correlate other biophysical quantities.

In conclusion, this work provides a tool to explore life's dynamic processes, enhancing and facilitating the description and understanding of the complex entanglement between space and time, chaotic diffusion and teleonomic function.

5 Acknowledgements

In this work, we built a tool to capture the subtle transition between chance and necessity, between thermal agitation and function.

On a macroscopic level, things are even more complicated, and the system—already complex at the nanoscale—interlaces across time and space scales, making free will seem like the only possible description for our choices.

This "obscure" paragraph to highlight that if I started and finished a PhD, it's due to a completely unexpected and chaotic sequence of events made accessible by the immense dedication of those closest to me.

Most of you know I was a mediocre university student. More than once, I thought about quitting to pursue more powerful artistic inclinations. On my own, I would have stalled. Without Carlo, Ronny, Francesca, and Alessio, I wouldn't have managed to complete my undergraduate degree. My first thanks go to you. A special thanks for Carlo that helped me in the English translation of Lucretius.

Things improved in Pisa, and among those who always supported me, I want to thank my roommate Franco, whose kindness and goodness made everyday life beautiful during those years.

There, I was fortunate to attend the biophysics lectures by Prof. Ranieri Bizzarri and become passionate about the stubborn struggle of living objects against the infamous energy minimum. Those inspiring classes led me to request my thesis in that field, and I still remember clearly when Dr. Barbara Storti first explained the concepts of tICS, stICS, and iMSD to me. A huge thanks to them, and especially to Ranieri. Without him, I wouldn't have made it to my third attempt to pursue a PhD within a few years. I want to acknowledge that he was the first person who, despite my grades, believed in me and gave me the opportunity to learn, grow, and be guided like only true mentors do.

I also thank them for the contributions of ideas, samples, support, and friendship they've given me over the years, without which this work wouldn't exist.

Here in Genova, under the guidance of Prof. Alberto Diaspro and Prof. Paolo Bianchini, I've had the opportunity to be part of a wonderful lab, made primarily by the people working there. I especially want to thank my supervisors for the freedom they granted me, the support for my ideas, the opportunity for dialogue, for the unique experiences, and for allowing me to attend the schools in Varenna and Erice and conferences in the United States and Portugal. I also thank them for the scientific -and not- discussions we've had over the years. I would like to thank Prof.

Enrico Gratton as well for the scientific exchanges we had both in Varenna and in San Diego during the BPS meeting.

In Genova, I met new and fantastic friends: Matteo, Fabio, with whom I shared almost everything during these years, Sabrina, Lisa, Francesca, Andrea, Eleonora, Sanket, Chantal, Isotta, Giacomo, Francesco, Alessandro, Eli, Alberta, Luca. Thanks to you, these years were filled with bright moments.

In particular, I want to dedicate an extra line to Matteo and Lisa for helping me with the various projects you see discussed here and for helping me with thesis corrections.

I also want to thank Michele, Marco, and Manuela for all their support over the years.

The PhD gave me the opportunity to go abroad and allowed me to explore a new world: Quebéc, and particularly Montréal. For this, I would like to thank Prof. Paul Wiseman and his fantastic group: Rodrigo, Cameron, Teo, Ahmad, and Andrew. I want to thank you all for the time we spent together, for our professional and non-professional exchanges. I truly left a piece of my heart on the other side of the ocean.

It's true that many things happen by chance, but opportunity is also the result of the work and sacrifices of many people, especially those close to me. I was the first person in my family to have the chance to study at university and graduate. When I still talk to my grandmother and hear about the heroic, harsh, exhausting, yet to her so ordinary labour of the humble life in the Apennine countryside, I feel privileged in a world where so many still live in even harsher conditions. When, in just two generations, we went from gathering every single leaf in the woods to feed the livestock during winter to generating entangled photons in a room on the ninth floor of a skyscraper, we can only thank the effort of our loved ones, the trees our grandfathers planted, the care of our grandmothers. The immense energy spent, the time devoted, and everything my mom and my dad have done and still do for me. A big thanks also to Rosanna and Gian for welcoming me into their family.

My deepest gratitude and thoughts go to Federica, who always supports me, who has always encouraged me, and who makes my life wonderful. In my characteristic widespread and overwhelming confusion, you are my polar star.

Ringraziamenti

In questo lavoro abbiamo costruito uno strumento per cogliere il sottile passaggio tra caso e necessità, tra agitazione termica e funzione.

A livello macroscopico le cose sono ancora più complicate e il sistema, già complesso alla nanoscala, si intreccia su scale di tempo e spazio che davvero il libero arbitrio sembra l'unica descrizione possibile per le nostre scelte.

Questo "oscuro" passaggio è per sottolineare che se io ho iniziato e finito un dottorato di ricerca lo devo ad una sequenza di eventi completamente imprevisti, caotici resi accessibili da moltissimo impegno delle persone a me più care.

La maggior parte di voi sa che sono stato un mediocre studente universitario. Più di una volta ho pensato di smettere per seguire suggestioni artistiche più potenti. Da solo mi sarei arenato. Senza Carlo Ronny Francesca e Alessio non sarei riuscito a terminare la triennale. Il primo ringraziamento va a voi. Un ulteriore ringraziamento a Carlo che mi ha aiutato nella traduzione di Lucrezio nel capitolo dell'FCS.

A Pisa le cose sono andate meglio, e tra le persone che mi hanno sempre sostenuto voglio ringraziare il mio compagno di stanza Franco, che con la sua gentilezza e la sua bontà ha reso bello il vivere quotidiano di quegli anni.

Qui ho avuto la fortuna di frequentare le lezioni di biofisica del prof Ranieri Bizzarri e di appassionarmi alla lotta testarda degli oggetti viventi contro il famigerato minimo di potenziale. Quelle lezioni appassionanti mi hanno portato a chiedere la tesi in quell'ambito e mi ricordo ancora bene quando la dottoressa Barbara Storti mi spiegava per la prima volta i concetti di tICS stICS iMSD. Un grande ringraziamento va a loro e specialmente a Ranieri. Senza di lui non sarei arrivato al terzo tentativo di provare ad accedere ad un dottorato nell'arco di un paio d'anni. Voglio riconoscergli il fatto che è stata la prima persona che, nonostante i miei voti, ha creduto in me e mi ha dato l'opportunità di imparare, crescere, e guidare come sanno fare i maestri.
Li ringrazio anche per il contributo di idee, di campioni e di supporto e di amicizia che mi hanno dato in questi anni e senza cui questo lavoro non esisterebbe.

Qui a Genova sotto la guida del Prof. Alberto Diaspro e del Prof. Paolo Bianchini ho avuto la possibilità di entrare in uno splendido laboratorio, fatto soprattutto delle persone che ci lavorano. Voglio ringraziare soprattutto i miei supervisori per la libertà che mi hanno concesso, il sostegno alle idee, la possibilità di un confronto, per le esperienze uniche e per la possibilità di accedere alle scuole di Varenna e Erice ai Congressi negli Stati Uniti e in Portogallo. Voglio inoltre ringraziarli per le

discussioni scientifiche, e non, avute in questi anni. Voglio ringraziare anche il Prof. Enrico Gratton per i confronti scientifici avuti sia a Varenna che a San Diego durante il BPS meeting.

A Genova ho conosciuto nuovi e fantastici amici, Matteo Fabio con cui abbiamo condiviso quasi tutto in questi anni, Sabrina Lisa Francesca Andrea Eleonora Sanket Chantal Isotta Giacomo Francesco Alessandro Eli Alberta Luca. Grazie a voi questi anni sono stati ricchi di momenti luminosi.

In particolare voglio ancora spendere una riga per Matteo e Lisa per avermi aiutato nei vari progetti che vedete trattati qui. E per avermi aiutato nella correzione della tesi.

Voglio ringraziare Michele Marco Manuela per tutto il supporto in questi anni.

Il dottorato mi ha dato la possibilità di andare all'estero e mi ha permesso di esplorare un mondo nuovo, il Quebéc e in particolare Montréal. Per questo devo ringraziare Prof. Paul Wiseman e tutto il suo fantastico gruppo: Rodrigo Cameron Teo Ahmad Andrew. Voglio ringraziarvi tutti per il tempo passato assieme. Per i reciproci scambi professionali e non. Ho davvero lasciato un po' di cuore al di là dell'oceano.

È vero che molte cose accadono per caso, ma l'opportunità è anche frutto del lavoro e sacrificio di tante persone. Soprattutto quelle a me vicine. Sono stato la prima persona della mia famiglia ad aver avuto l'opportunità di studiare all'università e di laurearmi. Quando ancora parlo con mia nonna e sento il lavoro eroico, devastante, usurante eppure per lei così ordinario della povera vita contadina appenninica non posso che sentirmi un privilegiato in un mondo in cui ancora moltissime persone vivono in una condizione ancora peggiore. Quando in due generazioni siamo passati dal raccogliere tutte le singole foglie nel bosco per poter darle da mangiare al bestiame d'inverno a generare fotoni intrecciati in una stanza al nono piano di un grattacielo, non possiamo che ringraziare la fatica dei nostri cari, gli alberi che hanno piantato i nostri nonni, le cure delle nostre nonne. L'immensa energia spesa, il tempo dedicato, e tutto quello che mia mamma e mio papà hanno fatto e fanno per me. Un grande ringraziamento anche a Rosanna e Gian per avermi accolto nella loro famiglia.

Il più grande ringraziamento e pensiero va a Federica, che mi supporta sempre, che mi ha sempre incoraggiato e che rende la mia vita splendida. Nella mia caratteristica confusione diffusa e imperante, sei la mia polare.

6 Bibliography

[1] R. P. Hardie and R. K. Gaye, "PHYSICS," in *Complete Works of Aristotle, Volume 1*, Princeton University Press, 1985, pp. 315–446. doi: 10.1515/9781400835843-010.

[2] Angelo Pagano and Emanuele V. Pagano, "Democrito: Una rivisitazione del modello meccanico Democritus: The mechanical model revisited," *QUADERNI DI STORIA DELLA FISICA*, vol. 26, 2022, doi: 10.1393/qsf/i2022-10086-1.

[3] R. Phillips and S. R. Quake, "The Biological Frontier of Physics," *Phys Today*, vol. 59, no. 5, pp. 38–43, May 2006, doi: 10.1063/1.2216960.

[4] C. Di Rienzo, E. Gratton, F. Beltram, and F. Cardarelli, "Fast spatiotemporal correlation spectroscopy to determine protein lateral diffusion laws in live cell membranes," *Proceedings of the National Academy of Sciences*, vol. 110, no. 30, pp. 12307–12312, Jul. 2013, doi: 10.1073/pnas.1222097110.

[5] C. Manzo and M. F. Garcia-Parajo, "A review of progress in single particle tracking: From methods to biophysical insights," *Reports on Progress in Physics*, vol. 78, no. 12, Oct. 2015, doi: 10.1088/0034-4885/78/12/124601.

[6] R. Brown, "Mikroskopische Beobachtungen über die im Pollen der Pflanzen enthaltenen Partikeln, und über das allgemeine Vorkommen activer Molecüle in organischen und unorganischen Körpern," *Ann Phys*, vol. 90, no. 10, pp. 294–313, Jan. 1828, doi: 10.1002/andp.18280901016.

[7] A. Einstein, "On the movement of small particles suspended in stationary liquids required by the molecular-kinetic theory of heat ," *Ann Phys*, vol. 322, no. 8, pp. 549–560, Jan. 1905.

[8] M. Weiss, "Crowding, Diffusion, and Biochemical Reactions," *Int Rev Cell Mol Biol*, vol. 307, pp. 383–417, Jan. 2014, doi: 10.1016/B978-0-12-800046-5.00011-4.

[9] M. Von Smoluchowski, "Zur kinetischen theorie der brownschen molekularbewegung und der suspensionen," *Ann Phys*, vol. 326 no. 14, pp. 756–780, 1906.

[10] H. Klein and D. Woermann, "Displacements of Brownian particles in terms of Marian von Smoluchowski's heuristic model," *J Chem Educ*, vol. 82, no. 11, pp. 1642–1644, 2005, doi: 10.1021/ED082P1642.

[11] K. PEARSON, "The Problem of the Random Walk," *Nature*, vol. 72, no. 1865, pp. 294–294, Jul. 1905, doi: 10.1038/072294b0.

[12] J.-P. Bouchaud and A. Georges, "Anomalous diffusion in disordered media: Statistical mechanisms, models and physical applications," *Phys Rep*, vol. 195, no. 4–5, pp. 127–293, Nov. 1990, doi: 10.1016/0370-1573(90)90099-N.

[13] J. Klafter, A. Blumen, and M. F. Shlesinger, "Stochastic pathway to anomalous diffusion," *Phys Rev A (Coll Park)*, vol. 35, no. 7, pp. 3081–3085, Apr. 1987, doi: 10.1103/PhysRevA.35.3081.

[14] H. Geerts *et al.*, "Nanovid tracking: a new automatic method for the study of mobility in living cells based on colloidal gold and video microscopy," *Biophys J*, vol. 52, no. 5, pp. 775–782, Nov. 1987, doi: 10.1016/S0006-3495(87)83271-X.

[15] M. J. Saxton and K. Jacobson, "SINGLE-PARTICLE TRACKING:Applications to Membrane Dynamics," *Annu Rev Biophys Biomol Struct*, vol. 26, no. 1, pp. 373–399, Jun. 1997, doi: 10.1146/annurev.biophys.26.1.373.

[16] J. Gelles, B. J. Schnapp, and M. P. Sheetz, "Tracking kinesin-driven movements with nanometre-scale precision," *Nature*, vol. 331, no. 6155, pp. 450–453, Feb. 1988, doi: 10.1038/331450a0.

[17] Y. Eilers, H. Ta, K. C. Gwosch, F. Balzarotti, and S. W. Hell, "MINFLUX monitors rapid molecular jumps with superior spatiotemporal resolution," *Proceedings of the National Academy of Sciences*, vol. 115, no. 24, pp. 6117–6122, Jun. 2018, doi: 10.1073/pnas.1801672115.

[18] F. Balzarotti *et al.*, "Nanometer resolution imaging and tracking of fluorescent molecules with minimal photon fluxes," *Science (1979)*, vol. 355, no. 6325, pp. 606–612, Feb. 2017, doi: 10.1126/science.aak9913.

[19] D. G. Priest, A. Solano, J. Lou, and E. Hinde, "Fluorescence fluctuation spectroscopy: an invaluable microscopy tool for uncovering the biophysical rules for navigating the nuclear landscape," *Biochem Soc Trans*, vol. 47, no. 4, pp. 1117–1129, Aug. 2019, doi: 10.1042/BST20180604.

[20] D. Axelrod, D. E. Koppel, J. Schlessinger, E. Elson, and W. W. Webb, "Mobility measurement by analysis of fluorescence photobleaching recovery kinetics," *Biophys J*, vol. 16, no. 9, pp. 1055–1069, Sep. 1976, doi: 10.1016/S0006-3495(76)85755-4.

[21] N. Lorén *et al.*, "Fluorescence recovery after photobleaching in material and life sciences: putting theory into practice," *Q Rev Biophys*, vol. 48, no. 3, pp. 323–387, Aug. 2015, doi: 10.1017/S0033583515000013.

[22] F. Mueller, D. Mazza, T. J. Stasevich, and J. G. McNally, "FRAP and kinetic modeling in the analysis of nuclear protein dynamics: what do we really know?," *Curr Opin Cell Biol*, vol. 22, no. 3, pp. 403–411, Jun. 2010, doi: 10.1016/j.ceb.2010.03.002.

[23] R. Kubo, "The fluctuation-dissipation theorem," *Reports on Progress in Physics*, vol. 29, no. 1, p. 306, Jan. 1966, doi: 10.1088/0034-4885/29/1/306.

[24] E. L. Elson and W. W. Webb, "Concentration correlation spectroscopy: a new biophysical probe based on occupation number fluctuations.," *Annu Rev Biophys Bioeng*, vol. 4, no. Volume 4, 1975, pp. 311–334, Jun. 1975, doi: 10.1146/ANNUREV.BB.04.060175.001523/CITE/REFWORKS.

[25] D. L. Kolin, S. Costantino, and P. W. Wiseman, "Sampling effects, noise, and photobleaching in temporal image correlation spectroscopy," *Biophys J*, vol. 90, no. 2, pp. 628–639, Jan. 2006, doi: 10.1529/biophysj.105.072322.

[26] R. P. Kulkarni, D. D. Wu, M. E. Davis, and S. E. Fraser, "Quantitating intracellular transport of polyplexes by spatio-temporal image correlation spectroscopy," *Proceedings of the National Academy of Sciences*, vol. 102, no. 21, pp. 7523–7528, May 2005, doi: 10.1073/pnas.0501950102.

[27] M. P. Sheetz and D. E. Koppel, "Membrane damage caused by irradiation of fluorescent concanavalin A.," *Proceedings of the National Academy of Sciences*, vol. 76, no. 7, pp. 3314–3317, Jul. 1979, doi: 10.1073/pnas.76.7.3314.

[28] D. E. Wolf, M. Edidin, and P. R. Dragsten, "Effect of bleaching light on measurements of lateral diffusion in cell membranes by the fluorescence photobleaching recovery method.," *Proceedings of the National Academy of Sciences*, vol. 77, no. 4, pp. 2043–2045, Apr. 1980, doi: 10.1073/pnas.77.4.2043.

[29] D. Magde, E. Elson, and W. W. Webb, "Thermodynamic Fluctuations in a Reacting System — Measurement by Fluorescence Correlation Spectroscopy," *Phys Rev Lett*, vol. 29, no. 11, p. 705, Sep. 1972, doi: 10.1103/PhysRevLett.29.705.

[30] B. Berne and R. Pecora, "Dynamic Light Scattering: With Applications to Chemistry, Biology, and Physics," 1976.

[31] M. Ehrenberg and R. Rigler, "Rotational brownian motion and fluorescence intensify fluctuations," *Chem Phys*, vol. 4, no. 3, pp. 390–401, Jun. 1974, doi: 10.1016/0301-0104(74)85005-6.

[32] D. E. Koppel, "Statistical accuracy in fluorescence correlation spectroscopy," *Phys Rev A (Coll Park)*, vol. 10, no. 6, pp. 1938–1945, Dec. 1974, doi: 10.1103/PhysRevA.10.1938.

[33] M. Weissman, H. Schindler, and G. Feher, "Determination of molecular weights by fluctuation spectroscopy: application to DNA.," *Proceedings of the National Academy of Sciences*, vol. 73, no. 8, pp. 2776–2780, Aug. 1976, doi: 10.1073/pnas.73.8.2776.

[34] N. O. Petersen, D. C. Johnson, and M. J. Schlesinger, "Scanning fluorescence correlation spectroscopy. II. Application to virus glycoprotein aggregation," *Biophys J*, vol. 49, no. 4, pp. 817–820, Apr. 1986, doi: 10.1016/S0006-3495(86)83710-9.

[35] N. O. Petersen, "Scanning fluorescence correlation spectroscopy. I. Theory and simulation of aggregation measurements," *Biophys J*, vol. 49, no. 4, pp. 809–815, Apr. 1986, doi: 10.1016/S0006-3495(86)83709-2.

[36] N. 0 Petersen, P. L. H6ddelius, P. W. Wiseman, O. Seger, and K.-E. Magnusson, "Quantitation of Membrane Receptor Distributions by Image Correlation Spectroscopy: Concept and Application," 1993. doi: 10.1016/S0006-3495(93)81173-1.

[37] M. Srivastava and N. O. Petersen, "Image cross-correlation spectroscopy: A new experimental biophysical approach to measurement of slow diffusion of fluorescent molecules," 1996.

[38] M. Brinkmeier, K. Dörre, J. Stephan, and M. Eigen, "Two-Beam Cross-Correlation: A Method To Characterize Transport Phenomena in Micrometer-Sized Structures," *Anal Chem*, vol. 71, no. 3, pp. 609–616, Feb. 1999, doi: 10.1021/ac980820i.

[39] B. Hebert, S. Costantino, and P. W. Wiseman, "Spatiotemporal Image Correlation Spectroscopy (STICS) Theory, Verification, and Application to Protein Velocity Mapping in Living CHO Cells," *Biophys J*, vol. 88, no. 5, pp. 3601–3614, May 2005, doi: 10.1529/biophysj.104.054874.

[40] M. A. Digman, C. M. Brown, P. Sengupta, P. W. Wiseman, A. R. Horwitz, and E. Gratton, "Measuring Fast Dynamics in Solutions and Cells with a Laser Scanning Microscope," *Biophys J*, vol. 89, no. 2, pp. 1317–1327, Aug. 2005, doi: 10.1529/BIOPHYSJ.105.062836.

[41] M. A. Digman, P. Sengupta, P. W. Wiseman, C. M. Brown, A. R. Horwitz, and E. Gratton, "Fluctuation correlation spectroscopy with a laser-scanning microscope: Exploiting the hidden time structure," *Biophys J*, vol. 88, no. 5, pp. L33–L36, May 2005, doi: 10.1529/biophysj.105.061788.

[42] L. Scipioni, M. Di Bona, G. Vicidomini, A. Diaspro, and L. Lanzanò, "Local raster image correlation spectroscopy generates high-resolution intracellular diffusion maps," *Commun Biol*, vol. 1, no. 1, p. 10, Feb. 2018, doi: 10.1038/s42003-017-0010-6.

[43] M. A. Digman and E. Gratton, "Imaging Barriers to Diffusion by Pair Correlation Functions," *Biophys J*, vol. 97, no. 2, pp. 665–673, Jul. 2009, doi: 10.1016/j.bpj.2009.04.048.

[44] C. Di Rienzo, V. Piazza, E. Gratton, F. Beltram, and F. Cardarelli, "Probing short-range protein Brownian motion in the cytoplasm of living cells," *Nat Commun*, vol. 5, no. 1, p. 5891, Dec. 2014, doi: 10.1038/ncomms6891.

[45] B. Storti, C. Di Rienzo, F. Cardarelli, R. Bizzarri, and F. Beltram, "Unveiling TRPV1 Spatio-Temporal Organization in Live Cell Membranes," *PLoS One*, vol. 10, no. 3, p. e0116900, Mar. 2015, doi: 10.1371/journal.pone.0116900.

[46] D. L. Kolin and P. W. Wiseman, "Advances in Image Correlation Spectroscopy: Measuring Number Densities, Aggregation States, and Dynamics of Fluorescently labeled Macromolecules in Cells," *Cell Biochem Biophys*, vol. 49, no. 3, pp. 141–164, Oct. 2007, doi: 10.1007/s12013-007-9000-5.

[47] A. D. Polyanin and V. E. Nazaikinskii, *Handbook of Linear Partial Differential Equations for Engineers and Scientists*. Chapman and Hall/CRC, 2015. doi: 10.1201/b19056.

[48] J. Kohler, K. H. Hur, and J. D. Mueller, "Autocorrelation function of finite-length data in fluorescence correlation spectroscopy," *Biophys J*, vol. 122, no. 1, pp. 241–253, Jan. 2023, doi: 10.1016/J.BPJ.2022.10.027.

[49] L. Wawrezinieck, H. Rigneault, D. Marguet, and P.-F. Lenne, "Fluorescence Correlation Spectroscopy Diffusion Laws to Probe the Submicron Cell Membrane Organization," *Biophys J*, vol. 89, no. 6, pp. 4029–4042, Dec. 2005, doi: 10.1529/biophysj.105.067959.

[50] C. Eggeling *et al.*, "Direct observation of the nanoscale dynamics of membrane lipids in a living cell," *Nature*, vol. 457, no. 7233, pp. 1159–1162, Feb. 2009, doi: 10.1038/nature07596.

[51] F. Schneider *et al.*, "Diffusion of lipids and GPI-anchored proteins in actin-free plasma membrane vesicles measured by STED-FCS," *Mol Biol Cell*, vol. 28, no. 11, pp. 1507–1518, Jun. 2017, doi: 10.1091/mbc.e16-07-0536.

[52] L. Lanzano *et al.*, "Application of the SPLIT-FLCS Method to the Detection of Nanoscale Diffusion in 3D in Live Cells," *Biophys J*, vol. 110, no. 3, p. 195a, Feb. 2016, doi: 10.1016/j.bpj.2015.11.1087.

[53] L. Scipioni, L. Lanzanó, A. Diaspro, and E. Gratton, "Comprehensive correlation analysis for super-resolution dynamic fingerprinting of cellular compartments using the Zeiss Airyscan detector," *Nat Commun*, vol. 9, no. 1, p. 5120, Nov. 2018, doi: 10.1038/s41467-018-07513-2.

[54] E. Slenders *et al.*, "Confocal-based fluorescence fluctuation spectroscopy with a SPAD array detector," *Light Sci Appl*, vol. 10, no. 1, p. 31, Feb. 2021, doi: 10.1038/s41377-021-00475-z.

[55] E. Perego *et al.*, "Single-photon microscopy to study biomolecular condensates," *Nat Commun*, vol. 14, no. 1, p. 8224, Dec. 2023, doi: 10.1038/s41467-023-43969-7.

[56] A. Gupta, I. Y. Phang, and T. Wohland, "To Hop or not to Hop: Exceptions in the FCS Diffusion Law," *Biophys J*, vol. 118, no. 10, pp. 2434–2447, May 2020, doi: 10.1016/j.bpj.2020.04.004.

[57] J. Sankaran, N. Bag, R. S. Kraut, and T. Wohland, "Accuracy and precision in camera-based fluorescence correlation spectroscopy measurements," *Anal Chem*, vol. 85, no. 8, pp. 3948–3954, Apr. 2013, doi: 10.1021/AC303485T.

[58] S. Veerapathiran and T. Wohland, "The imaging FCS diffusion law in the presence of multiple diffusive modes," *Methods*, vol. 140–141, pp. 140–150, May 2018, doi: 10.1016/j.ymeth.2017.11.016.

[59] H. Blom *et al.*, "Parallel fluorescence detection of single biomolecules in microarrays by a diffractive-optical-designed 2 × 2 fan-out element," *Appl Opt*, vol. 41, no. 16, p. 3336, Jun. 2002, doi: 10.1364/AO.41.003336.

[60] Q. Ruan, M. A. Cheng, M. Levi, E. Gratton, and W. W. Mantulin, "Spatial-Temporal Studies of Membrane Dynamics: Scanning Fluorescence Correlation Spectroscopy (SFCS)," *Biophys J*, vol. 87, no. 2, pp. 1260–1267, Aug. 2004, doi: 10.1529/biophysj.103.036483.

[61] D. Sisan, R. C. Arevalo, C. Graves, R. G. McAllister, and J. Urbach, "Massively-parallel fluorescence correlation spectroscopy using a spinning disk confocal microscope," *Bulletin of the American Physical Society*, 2006.

[62] D. R. Sisan, R. Arevalo, C. Graves, R. McAllister, and J. S. Urbach, "Spatially Resolved Fluorescence Correlation Spectroscopy Using a Spinning Disk Confocal Microscope," *Biophys J*, vol. 91, no. 11, pp. 4241–4252, Dec. 2006, doi: 10.1529/biophysj.106.084251.

[63] B. Kannan, L. Guo, T. Sudhaharan, S. Ahmed, I. Maruyama, and T. Wohland, "Spatially Resolved Total Internal Reflection Fluorescence Correlation Microscopy Using an Electron Multiplying Charge-Coupled Device Camera," *Anal Chem*, vol. 79, no. 12, pp. 4463–4470, Jun. 2007, doi: 10.1021/ac0624546.

[64] T. Wohland, X. Shi, J. Sankaran, and E. H. K. Stelzer, "Single Plane Illumination Fluorescence Correlation Spectroscopy (SPIM-FCS) probes inhomogeneous three-dimensional environments," *Opt Express*, vol. 18, no. 10, p. 10627, May 2010, doi: 10.1364/OE.18.010627.

[65] J. Ries and P. Schwille, "New concepts for fluorescence correlation spectroscopy on membranes," *Article in Physical Chemistry Chemical Physics*, 2008, doi: 10.1039/b718132a.

[66] M. Di Bona, M. A. Mancini, D. Mazza, G. Vicidomini, A. Diaspro, and L. Lanzanò, "Measuring Mobility in Chromatin by Intensity-Sorted FCS," *Biophys J*, vol. 116, no. 6, pp. 987–999, Mar. 2019, doi: 10.1016/j.bpj.2019.02.003.

[67] T. Wohland, R. Rigler, and H. Vogel, "The Standard Deviation in Fluorescence Correlation Spectroscopy," *Biophys J*, vol. 80, pp. 2987–2999, 2001, doi: 10.1016/S0006-3495(01)76264-9.

[68] T. Wohland, S. Maiti, and R. Macháň, *An Introduction to Fluorescence Correlation Spectroscopy*. IOP Publishing, 2020. doi: 10.1088/978-0-7503-2080-1.

[69] M. Brinkmeier, K. Dörre, J. Stephan, and M. Eigen, "Two-Beam Cross-Correlation: A Method To Characterize Transport Phenomena in Micrometer-Sized Structures," *Anal Chem*, vol. 71, no. 3, pp. 609–616, Feb. 1999, doi: 10.1021/ac980820i.

[70] P. Bianchini, F. Cardarelli, M. Di Luca, A. Diaspro, and R. Bizzarri, "Nanoscale Protein Diffusion by STED-Based Pair Correlation Analysis," *PLoS One*, vol. 9, no. 6, p. e99619, Jun. 2014, doi: 10.1371/journal.pone.0099619.

[71] F. Cardarelli and E. Gratton, "In Vivo Imaging of Single-Molecule Translocation Through Nuclear Pore Complexes by Pair Correlation Functions," *PLoS One*, vol. 5, no. 5, p. e10475, May 2010, doi: 10.1371/journal.pone.0010475.

[72] F. Cardarelli, L. Lanzano, and E. Gratton, "Capturing directed molecular motion in the nuclear pore complex of live cells," *Proc Natl Acad Sci U S A*, vol. 109, no. 25, pp. 9863–9868, Jun. 2012, doi: 10.1073/PNAS.1200486109/SUPPL_FILE/PNAS.1200486109_SI.PDF.

[73] P. W. Wiseman and N. O. Petersen, "Image Correlation Spectroscopy. II. Optimization for Ultrasensitive Detection of Preexisting Platelet-Derived Growth Factor-β Receptor Oligomers on Intact Cells," *Biophys J*, vol. 76, no. 2, pp. 963–977, Feb. 1999, doi: 10.1016/S0006-3495(99)77260-7.

[74] P. W. Wiseman, P. Höddelius, N. O. Petersen, and K.-E. Magnusson, "Aggregation of PDGF-β receptors in human skin fibroblasts: characterization by image correlation spectroscopy (ICS)," *FEBS Lett*, vol. 401, no. 1, pp. 43–48, Jan. 1997, doi: 10.1016/S0014-5793(96)01429-9.

[75] N. O. Petersen, C. Brown, A. Kaminski, J. Rocheleau, M. Srivastava, and P. W. Wiseman, "Analysis of membrane protein cluster densities and sizes in situ by image correlation spectroscopy," *Faraday Discuss*, vol. 111, no. 0, pp. 289–305, Jan. 1999, doi: 10.1039/A806677I.

[76] L. Scipioni, E. Gratton, A. Diaspro, and L. Lanzanò, "Phasor Analysis of Local ICS Detects Heterogeneity in Size and Number of Intracellular Vesicles," *Biophys J*, vol. 111, no. 3, pp. 619–629, Aug. 2016, doi: 10.1016/j.bpj.2016.06.029.

[77] M. Longfils *et al.*, "Raster Image Correlation Spectroscopy Performance Evaluation," *Biophys J*, vol. 117, no. 10, pp. 1900–1914, Nov. 2019, doi: 10.1016/j.bpj.2019.09.045.

[78] E. A. Jares-Erijman and T. M. Jovin, "FRET imaging," *Nat Biotechnol*, vol. 21, no. 11, pp. 1387–1395, Nov. 2003, doi: 10.1038/nbt896.

[79] J. Ries, S. Chiantia, and P. Schwille, "Accurate Determination of Membrane Dynamics with Line-Scan FCS," *Biophys J*, vol. 96, no. 5, pp. 1999–2008, Mar. 2009, doi: 10.1016/j.bpj.2008.12.3888.

[80] M. A. Digman, C. M. Brown, A. R. Horwitz, W. W. Mantulin, and E. Gratton, "Paxillin Dynamics Measured during Adhesion Assembly and Disassembly by Correlation Spectroscopy," *Biophys J*, vol. 94, no. 7, pp. 2819–2831, Apr. 2008, doi: 10.1529/biophysj.107.104984.

[81] L. Cuneo, S. Civita, P. Bianchini, and A. Diaspro, "Scattering networks: A tool to remove the background," pp. 143–145, 2023, doi: 10.3254/ENFI230014.

[82] G. Sun, S. M. Guo, C. Teh, V. Korzh, M. Bathe, and T. Wohland, "Bayesian model selection applied to the analysis of fluorescence correlation spectroscopy data of fluorescent proteins in vitro and in vivo," *Anal Chem*, vol. 87, no. 8, pp. 4326–4333, Apr. 2015, doi: 10.1021/ACS.ANALCHEM.5B00022/SUPPL_FILE/AC5B00022_SI_001.PDF.

[83] S.-M. Guo, J. He, N. Monnier, G. Sun, T. Wohland, and M. Bathe, "Bayesian Approach to the Analysis of Fluorescence Correlation Spectroscopy Data II: Application to Simulated and In Vitro Data," *Anal Chem*, vol. 84, no. 9, pp. 3880–3888, May 2012, doi: 10.1021/ac2034375.

[84] S. Sommariva and A. Sorrentino, "Sequential Monte Carlo samplers for semilinear inverse problems and application to magnetoencephalography," *Inverse Probl*, vol. 30, no. 11, p. 114020, Nov. 2014, doi: 10.1088/0266-5611/30/11/114020.

[85] L. Cuneo, "Analysis of advanced optical microscopy data through Artificial Intelligent algorithms," *PhD Thesis*, 2024.

[86] J. Skilling and R. K. Bryan, "Maximum entropy image reconstruction: general algorithm," *Mon Not R Astron Soc*, vol. 211, no. 1, pp. 111–124, Nov. 1984, doi: 10.1093/mnras/211.1.111.

[87] P. J. Steinbach *et al.*, "Ligand binding to heme proteins: connection between dynamics and function," *Biochemistry*, vol. 30, no. 16, pp. 3988–4001, Apr. 1991, doi: 10.1021/bi00230a026.

[88] P. J. Steinbach, R. Ionescu, and C. R. Matthews, "Analysis of Kinetics Using a Hybrid Maximum-Entropy/Nonlinear-Least-Squares Method: Application to Protein Folding," *Biophys J*, vol. 82, no. 4, pp. 2244–2255, Apr. 2002, doi: 10.1016/S0006-3495(02)75570-7.

[89] R. Narayan and R. Nityananda, "Maximum Entropy Image Restoration in Astronomy," *Annu Rev Astron Astrophys*, vol. 24, no. 1, pp. 127–170, Sep. 1986, doi: 10.1146/annurev.aa.24.090186.001015.

[90] R. A. Migueles-Ramírez, A. Cambi, A. Hayer, P. W. Wiseman, and K. van den Dries, "Quantifying superimposed protein flow dynamics in live cells using spatial filtering and spatiotemporal image correlation spectroscopy," *J Microsc*, Jul. 2024, doi: 10.1111/jmi.13342.

[91] Z. Gong, K. van den Dries, R. A. Migueles-Ramírez, P. W. Wiseman, A. Cambi, and V. B. Shenoy, "Chemo-mechanical diffusion waves explain collective dynamics of immune cell podosomes," *Nat Commun*, vol. 14, no. 1, p. 2902, May 2023, doi: 10.1038/s41467-023-38598-z.

[92] S. Civita, R. Bizzarri, P. Bianchini, and A. Diaspro, "Image correlation spectroscopy approaches to probe diffusion in cell," *Biophys J*, vol. 122, no. 3, p. 274a, Feb. 2023, doi: 10.1016/j.bpj.2022.11.1563.

[93] L. Malacrida, E. Rao, and E. Gratton, "Comparison between iMSD and 2D-pCF analysis for molecular motion studies on in vivo cells: The case of the epidermal growth factor receptor," *Methods*, vol. 140–141, pp. 74–84, May 2018, doi: 10.1016/j.ymeth.2018.01.010.

[94] L. Lanzanò *et al.*, "Measurement of nanoscale three-dimensional diffusion in the interior of living cells by STED-FCS," *Nat Commun*, vol. 8, no. 1, p. 65, Jul. 2017, doi: 10.1038/s41467-017-00117-2.

[95] M. A. Digman, V. R. Caiolfa, M. Zamai, and E. Gratton, "The Phasor Approach to Fluorescence Lifetime Imaging Analysis," *Biophys J*, vol. 94, no. 2, pp. L14–L16, Jan. 2008, doi: 10.1529/biophysj.107.120154.

[96] S. Ranjit, L. Lanzano, and E. Gratton, "Mapping Diffusion in a Living Cell via the Phasor Approach," *Biophys J*, vol. 107, no. 12, pp. 2775–2785, Dec. 2014, doi: 10.1016/j.bpj.2014.08.041.

[97] M. Ruglioni *et al.*, "Nanoscale engagement and clusterization of Programmed death ligand 1 (PD-L1) in the membrane lipid rafts of Non-Small Cell Lung Cancer cells," 2022. doi: 10.1101/2022.08.09.503318.

[98] W. H. Tang *et al.*, "Deep learning reduces data requirements and allows real-time measurements in Imaging Fluorescence Correlation Spectroscopy," 2023, doi: 10.1101/2023.08.07.552352.

[99] E. T. Castellana and P. S. Cremer, "Solid supported lipid bilayers: From biophysical studies to sensor design," *Surf Sci Rep*, vol. 61, no. 10, pp. 429–444, Nov. 2006, doi: 10.1016/j.surfrep.2006.06.001.

[100] P. Delcanale, S. Abbruzzetti, and C. Viappiani, "Photodynamic treatment of pathogens," *La Rivista del Nuovo Cimento*, vol. 45, no. 6, pp. 407–459, Jun. 2022, doi: 10.1007/s40766-022-00031-4.

[101] M. Mariangeli *et al.*, "Photosensitizers against pathogens: Model membranes characterization with hypericin," *Biophys J*, vol. 122, no. 3, p. 547a, Feb. 2023, doi: 10.1016/j.bpj.2022.11.2895.

[102] M. Mariangeli *et al.*, "Quantitative analysis of hypericin interaction with SARS-CoV 2 and with a model membrane," *Biophys J*, vol. 121, no. 3, p. 141a, Feb. 2022, doi: 10.1016/j.bpj.2021.11.2029.

[103] P. Delcanale *et al.*, "The Interaction of Hypericin with SARS-CoV-2 Reveals a Multimodal Antiviral Activity," *ACS Appl Mater Interfaces*, vol. 14, no. 12, pp. 14025–14032, Mar. 2022, doi: 10.1021/acsami.1c22439.

[104] M. Mariangeli *et al.*, "Insights on the Mechanical Properties of SARS-CoV-2 Particles and the Effects of the Photosensitizer Hypericin," *Int J Mol Sci*, vol. 25, no. 16, p. 8724, Aug. 2024, doi: 10.3390/ijms25168724.

[105] Matteo Mariangeli, "A correlative and multimodal microscopy approach to study the interaction of photosensitizers with biological samples," 2024.

[106] S. Chiantia , J. Ries , N. Kahya, and P. Schwille, "Combined AFM and Two-Focus SFCS Study of Raft-Exhibiting Model Membranes," *ChemPhysChem*, vol. 7, no. 11, pp. 2409–2418, Nov. 2006, doi: 10.1002/cphc.200600464.

[107] L. Lanzanò, I. Coto Hernández, M. Castello, E. Gratton, A. Diaspro, and G. Vicidomini, "Encoding and decoding spatio-temporal information for super-resolution microscopy," *Nat Commun*, vol. 6, no. 1, p. 6701, Apr. 2015, doi: 10.1038/ncomms7701.

[108] M. J. Rust, M. Bates, and X. Zhuang, "Sub-diffraction-limit imaging by stochastic optical reconstruction microscopy (STORM)," *Nat Methods*, vol. 3, no. 10, pp. 793–796, Oct. 2006, doi: 10.1038/nmeth929.

[109] H. Deschout *et al.*, "Precisely and accurately localizing single emitters in fluorescence microscopy," *Nat Methods*, vol. 11, no. 3, pp. 253–266, Mar. 2014, doi: 10.1038/nmeth.2843.

[110] C. J. R. Sheppard *et al.*, "Pixel reassignment in image scanning microscopy: a re-evaluation," *Journal of the Optical Society of America A*, vol. 37, no. 1, p. 154, Jan. 2020, doi: 10.1364/JOSAA.37.000154.

[111] G. Vicidomini, P. Bianchini, and A. Diaspro, "STED super-resolved microscopy," *Nat Methods*, vol. 15, no. 3, pp. 173–182, Mar. 2018, doi: 10.1038/nmeth.4593.

[112] J. Sankaran and T. Wohland, "Current capabilities and future perspectives of FCS: super-resolution microscopy, machine learning, and in vivo applications," *Commun Biol*, vol. 6, no. 1, Dec. 2023, doi: 10.1038/S42003-023-05069-6.

[113] R. B. Dalal, M. A. Digman, A. F. Horwitz, V. Vetri, and E. Gratton, "Determination of particle number and brightness using a laser scanning confocal microscope operating in the analog mode," *Microsc Res Tech*, vol. 71, no. 1, pp. 69–81, 2008, doi: 10.1002/JEMT.20526.

[114] H. Qian and E. L. Elson, "Distribution of molecular aggregation by analysis of fluctuation moments.," *Proceedings of the National Academy of Sciences*, vol. 87, no. 14, pp. 5479–5483, Jul. 1990, doi: 10.1073/pnas.87.14.5479.

[115] Y. Chen, J. D. Müller, Q. Ruan, and E. Gratton, "Molecular Brightness Characterization of EGFP In Vivo by Fluorescence Fluctuation Spectroscopy," *Biophys J*, vol. 82, no. 1, pp. 133–144, Jan. 2002, doi: 10.1016/S0006-3495(02)75380-0.

[116] R. A. Kerr *et al.*, "Fast Monte Carlo Simulation Methods for Biological Reaction-Diffusion Systems in Solution and on Surfaces," *SIAM Journal on Scientific Computing*, vol. 30, no. 6, pp. 3126–3149, Jan. 2008, doi: 10.1137/070692017.

[117] J. R. Unruh and E. Gratton, "Analysis of Molecular Concentration and Brightness from Fluorescence Fluctuation Data with an Electron Multiplied CCD Camera," *Biophys J*, vol. 95, no. 11, pp. 5385–5398, Dec. 2008, doi: 10.1529/biophysj.108.130310.

[118] P. D. J. Moens, E. Gratton, and I. L. Salvemini, "Fluorescence correlation spectroscopy, raster image correlation spectroscopy, and number and brightness on a commercial confocal laser scanning microscope with analog detectors (Nikon C1)," *Microsc Res Tech*, vol. 74, no. 4, pp. 377–388, Apr. 2011, doi: 10.1002/jemt.20919.

[119] M. A. Digman, R. Dalal, A. F. Horwitz, and E. Gratton, "Mapping the Number of Molecules and Brightness in the Laser Scanning Microscope," *Biophys J*, vol. 94, no. 6, pp. 2320–2332, Mar. 2008, doi: 10.1529/BIOPHYSJ.107.114645.

[120] S. Saffarian and E. L. Elson, "Statistical Analysis of Fluorescence Correlation Spectroscopy: The Standard Deviation and Bias," *Biophys J*, vol. 84, no. 3, pp. 2030–2042, Mar. 2003, doi: 10.1016/S0006-3495(03)75011-5.

[121] L. Malacrida, P. N. Hedde, S. Ranjit, F. Cardarelli, and E. Gratton, "Visualization of barriers and obstacles to molecular diffusion in live cells by spatial pair-

cross-correlation in two dimensions," *Biomed Opt Express*, vol. 9, no. 1, p. 303, Jan. 2018, doi: 10.1364/BOE.9.000303.

[122] T. Dertinger, R. Colyer, G. Iyer, S. Weiss, and J. Enderlein, "Fast, background-free, 3D super-resolution optical fluctuation imaging (SOFI)," *Proceedings of the National Academy of Sciences*, vol. 106, no. 52, pp. 22287–22292, Dec. 2009, doi: 10.1073/pnas.0907866106.

[123] N. Gustafsson, S. Culley, G. Ashdown, D. M. Owen, P. M. Pereira, and R. Henriques, "Fast live-cell conventional fluorophore nanoscopy with ImageJ through super-resolution radial fluctuations," *Nat Commun*, vol. 7, no. 1, p. 12471, Aug. 2016, doi: 10.1038/ncomms12471.

[124] W. Zhao *et al.*, "Enhanced detection of fluorescence fluctuations for high-throughput super-resolution imaging," *Nat Photonics*, vol. 17, no. 9, pp. 806–813, Sep. 2023, doi: 10.1038/s41566-023-01234-9.